Copyright

by

Michael Andrew Carey

2014

The Thesis Committee for Michael Andrew Carey
Certifies that this is the approved version of the following thesis:

Water Hammer Fracture Diagnostics

APPROVED BY
SUPERVISING COMMITTEE:

Supervisor:

Mukul M. Sharma

Mark W. McClure

Water Hammer Fracture Diagnostics

by

Michael Andrew Carey, BSPE BSGEH

Thesis

Presented to the Faculty of the Graduate School of

The University of Texas at Austin

in Partial Fulfillment

of the Requirements

for the Degree of

Master of Science in Engineering

The University of Texas at Austin

December, 2014

Dedication

To my family, girlfriend, and friends that have always supported me.

Acknowledgements

First and foremost I would like to acknowledge my supervisor, Dr. Mukul M. Sharma, for all that he has done for me during my time in graduate school at The University of Texas. I also want to thank the second member of my committee, Dr. Mark McClure, for all his assistance, and the reading and evaluation of my work.

I would like to acknowledge Anadarko Petroleum Corporation for providing me with much needed data. I would also like to thank Jin Lee for all the assistance she has given me while making sure everything in the research group runs smoothly. Finally, I want to thank all my family and friends who have encouraged and supported me.

Abstract

Water Hammer Fracture Diagnostics

Michael Andrew Carey, MSE

The University of Texas at Austin, 2014

Supervisor: Mukul M. Sharma

A sudden change in flow in a confined system results in the formation of a series of pressure pulses known as a water hammer. Pump shutdown at the conclusion of a hydraulic fracture treatment frequently generates a water hammer, which sends a pressure pulse down the wellbore that interacts with the created fracture before returning towards the surface. This study confirms that created hydraulic fractures alter the period, amplitude, and duration of the water hammer signal. Water hammer pressure signals were simulated with a previously presented numerical model that combined the continuity and momentum equations of the wellbore with a created hydraulic fracture represented by a *RCI* series circuit. Field data from several multi-stage stimulation treatments were history matched with the numerical model by iteratively altering *R*, *C*, and *I* until an appropriate match was obtained. Equivalent fracture dimensions were calculated from *R*, *C*, and *I*, and were in agreement with acquired micro-seismic SRV. Finally, the obtained *R*, *C*, and *I* values were compared to SRV and production log data. Capacitance was directly correlated with SRV, while resistance was inversely correlated with SRV, and no correlations with production data were observed.

Table of Contents

List of Tables x

List of Figures xi

Chapter 1: Introduction 1

1.1 Literature Review 3

1.1.1 Water Hammer Modeling 3

1.1.2 Friction Calculations 5

1.1.3 Fracture Impedance 6

1.1.4 Water Hammer Period 7

Chapter 2: Water Hammer Characteristics Study 9

2.1 Water hammer study introduction 9

2.2 Water Hammer : Some Characteristic Properties 9

2.2.1 Period 10

2.2.2 Amplitude 10

2.2.3 Decay Rate 10

2.3 Production log and srv data 11

2.3.1 Production Log Data 11

2.3.2 SRV Data 11

2.4 Study results and discussion 11

2.4.1 Period 12

2.4.2 Amplitude 15

2.4.3 Decay Rate 18

2.5 Period discrepancy and error 21

2.5.1 Field Data Under Sampling 22

2.5.2 Fractures Alter Period 24

2.6 conclusions from characteristics study 26

Chapter 3: Model Formulation 27

3.1 Water hammer modeling equations 27

3.1.1 Equation of Motion 27
3.1.2 Continuity Equation 28
3.1.3 Water Hammer Wave Speed 29
3.2 Using the method of characteristics 30
3.2.1 Finite Difference Equations 34
3.3 Boundary conditions 37
3.3.1 Pipe System Nomenclature 37
3.3.2 Upstream Surface Valve 38
3.3.3 Pipe Section Series Connection 39
3.3.4 Downstream Fracture Boundary Condition 41
3.4 Equations for fracture parameter estimation 45
3.4.1 Assumptions for Fracture Dimension Calculations 45
3.4.2 Calculating R, C, and I from Fracture Dimensions 47
3.4.3 Length and Width Estimation from Known Fracture Height 49
3.4.4 Equivalent Fracture Dimensions 51
3.5 Model Validation 54
3.5.1 Mondal (2010) Field Data 54
3.5.2 How *RCI* Variations Affect Pressure Profile 55
3.5.2.1 Variations in Resistance 55
3.5.2.2 Variations of Capacitance 55
3.5.2.3 Variations of Inertance 56
3.5.2.4 RCI Iteration Method 58
3.5.3 Ferrick et al. (1982) Field Data 58
3.6 Model Formulation Summary 61

Chapter 4: Results and Discussion 62
4.1 History Matching Field Data 62
4.2 *RCI* Relationships with Production and SRV 63
4.3 Simulated Bottom-hole Pressures 67
4.4 Fracture Treatment Diagnostic Tool 68
4.5 Fracture Complexity Index Correlations 70

4.6 Wavelength Identification with Fourier Transforms 73

Chapter 5: Conclusion.....76

Appendices.....78

Appendix A: Elliptical Integral Equations.....79

Appendix B: Oscillation Profiles for Varying *R*, *C*, and *I*.....80

Appendix C: Field Data and Numerical Model History Matches.....83

Appendix D: Tables of *RCI* values and Fracture Dimensions.....97

References.....99

List of Tables

Table 3.1: Summary of hydraulic fracture boundary condition terms and electrical circuit equivalents 43

Table 3.2: Fracture dimensions comparison between Mondal (2010) values and current numerical model 55

Table 4.1: Summary of *RCI* values and fracture dimensions for the multiple shutdown events from Wells A and C. 69

Table D.1: Well A *RCI* and fracture dimension values obtained from history matching.....97

Table D.2: Well B *RCI* and fracture dimension values obtained from history matching.....98

Table D.3: Well C *RCI* and fracture dimension values obtained from history matching.....98

List of Figures

Figure 1.1: UT-Pipeflow schematic of water hammer pressure oscillations in a horizontal well 2

Figure 2.1: Water hammer characteristic properties. 9

Figure 2.2: An example pressure signal showing several water hammer decay rates. 10

Figure 2.4: Water hammer period versus SRV 13

Figure 2.5: Measured depth versus water hammer period 13

Figure 2.6: Water hammer period normalized by depth versus gas production 14

Figure 2.7: Water hammer period normalized by depth versus SRV 14

Figure 2.8: Initial water hammer amplitude versus gas production 15

Figure 2.9: Average water hammer amplitude versus gas production 16

Figure 2.10: Initial water hammer amplitude versus gas production 16

Figure 2.11: Average water hammer amplitude versus SRV 17

Figure 2.12: Average water hammer amplitude normalized by injection rate prior to shutdown plotted versus SRV 17

Figure 2.13: Decay rate exponent *B* versus gas production 18

Figure 2.14: Decay rate exponent *B* versus SRV 19

Figure 2.15: Water hammer duration versus SRV 20

Figure 2.16: Water hammer pressure oscillations after 207, 2385, 3338, and 47,700 Liters were pumped during a hydraulic fracture treatment (From Holzhausen et al., 1985) 21

Figure 2.17: Field data water hammer period compared to water hammer period calculated from Eq. (1.2) 22

Figure 2.18: How under sampling may alter the observed water hammer period (From Wang et al., 2008) 22
Figure 2.17: Water hammer data generated at $1/10^{th}$ second intervals and sampled at 1 second intervals to investigate under sampling effects 23
Figure 2.18: Free oscillations observed in a 1589 m deep well a) prior to and b) after fracturing. The period shifts from $2L/a$ in the unfractured case to $4L/a$ in the fracture case. (From Ferrick et al., 1982) 25
Figure 2.19: Histogram of percent difference between field water hammer period and Holzhausen's predicted $4L/a$ 25
Figure 2.20: Fluid distributions after a gel hydraulic fracture treatment 26
Figure 3.1: C^+ and C^- characteristic lines in the x-t plane (From Mondal, 2010) 33
Figure 3.2: Grid of characteristic lines in the x-t plane. (From Mondal, 2010) ..34
Figure 3.3: Pipe system consisting of two pipes connected in series. (Mondal, 2010) 38
Figure 3.4: Rate versus time and τ versus time at shutdown of a completed hydraulic fracture treatment 39
Figure 3.5: C^+ and C^- characteristic equations for a pipe series connection between pipe section i and $i+1$ 40
Figure 3.6: Schematics for (a) horizontal wellbore with fracture and (b) the electrical circuit representation 44
Figure 3.7: Graphical representation of determining P_f from fitting the surface pressure data with an exponential function (From Mondal, 2010)...47
Figure 3.8: Map view schematic of a stimulation stage in a horizontal well with three perforation clusters and three created hydraulic fractures. 53

Figure 3.9: Map view of Fig. 3.8 modeled as a *RCI* circuit with the three fracture capacitances connected in parallel. 53

Figure 3.10: History match of Mondal (2010) field data with numerical model data where R = 52.9 bpd/psi, C = 4.33×10^{-2} bbl/psi, and I = 2.45×10^{-10} psi/bbl/d^2. 54

Figure 3.11: Summary of the effect of resistance on the initial water hammer amplitude.....56

Figure 3.12: Summary of the effect of capacitance on the water hammer period.57

Figure 3.13: Summary of the effect of capacitance on the pressure sustained during a water hammer event. 57

Figure 3.14: Summary of the effect of inertance on the water hammer period.....58

Figure 3.15: History match of Ferrick et al. (1982) post-frac data with numerical model.....59

Figure 3.16: Diagram of Ferrick et al. (1982) well with large difference in tubing and casing inner diameters (not to scale).....60

Figure 3.17: Capacitance versus normalized frequency from Ferrick et al. (1982) data for (a) *RCI* numerical model and (b) Holzhausen et al. (1985) *RC* impedance model. 61

Figure 4.1: History match of field data with simulation results for shutdown event 1 in stage 1 of Well A 62

Figure 4.2: Capacitance obtained from our model's interpretation of water hammer data plotted versus stimulated reservoir volume (SRV). 64

Figure 4.3: Resistance obtained from our model's interpretation of water hammer data plotted versus stimulated reservoir volume (SRV). 64

Figure 4.4: Inertance obtained from our model's interpretation of water hammer data plotted versus stimulated reservoir volume (SRV). 65
Figure 4.5: Capacitance obtained from our model's interpretation of water hammer data plotted versus gas production obtained from production logs. .65
Figure 4.6: Inertance obtained from our model's interpretation of water hammer data plotted versus gas production obtained from production logs. .66
Figure 4.7: Resistance obtained from our model's interpretation of water hammer data plotted versus gas production obtained from production logs. .66
Figure 4.8: Stimulated reservoir volume (SRV) plotted versus gas production obtained from production logs. 67
Figure 4.9: Simulated bottomhole pressure for shutdown event 1 of stage 1, well A.....68
Figure 4.10: Surface pressure profile that depicts the two shutdown events of Well A, stage 1. (Note: large fluctuations due to bad transducer or cable)....69
Figure 4.11: Surface pressure profile that depicts the two shutdown events of Well C, stage 10 69
Figure 4.12: Visual description of how micro-seismic width and length were obtained from SRV data. 70
Figure 4.13: Resistance versus fracture complexity index (FCI). 71
Figure 4.14: Capacitance versus fracture complexity index (FCI).....72
Figure 4.15: Inertance versus fracture complexity index (FCI). 72
Figure 4.16: Ratio of calculated width to length versus fracture complexity index (FCI).....73

Figure 4.17: Micro-seismic events showing communication with an adjacent zone during stimulation treatment either due to poor cement job or leaky packer for stage 3 of well B. 74

Figure 4.18: Fast Fourier Transform of Well B, Stage 3 which identifies the dominant period as 10.6 seconds, but fails to identify the period of the nearby zone due to low resolution of pressure data. 75

Figure B.1: Oscillation profiles for resistances of (a) $2.67x10^{-6}$ psi/bpd, (b) $8.44x10^{-3}$ psi/bpd, (c) $1.89x10^{-2}$ psi/bpd, and (d) $3.36x10^{-2}$ psi/bpd at a fixed C and I of $1.37x10^{-3}$ ^{3} bbl/psi, and $2.45x10^{-10}$ psi/bbl/d^2 respectively. 80

Figure B.2: Oscillation profiles for capacitances of (a) $4.34x10^{-6}$ bbl/psi, (b) $1.37x10^{-4}$ bbl/psi, (c) $1.37x10^{-3}$ bbl/psi, and (d) 1.37 bbl/psi at a fixed *R* and *I* of $1.89x10^{-2}$ psi/bpd and $2.45x10^{-10}$ psi/bbl/d^2 respectively. ...81

Figure B.3: Oscillation profiles for inertances of (a) $3.09x10^{-10}$ psi/bbl/d^2, (b) $3.09x10^{-7}$ psi/bbl/d^2, (c) $9.77x10^{-7}$ psi/bbl/d^2, and (d) $9.77x10^{-6}$ psi/bbl/d^2 at a fixed *R* and *C* of $1.89x10^{-2}$ psi/bpd $1.37x10^{-3}$ bbl/psi respectively. 82

Figure C.1: History match of well A, stage 1, shutdown 2 field data with numerical model results 83

Figure C.2: History match of well A, stage 3 field data with numerical model results 83

Figure C.3: History match of well A, stage 4 field data with numerical model results 83

Figure C.4: History match of well A, stage 5 field data with numerical model results 84

Figure C.5: History match of well A, stage 6 field data with numerical model results 84
Figure C.6: History match of well A, stage 7 field data with numerical model results 84
Figure C.7: History match of well A, stage 8 field data with numerical model results 85
Figure C.8: History match of well A, stage 9 field data with numerical model results 85
Figure C.9: History match of well A, stage 10 field data with numerical model results 85
Figure C.10: History match of well A, stage 11 field data with numerical model results 86
Figure C.11: History match of well A, stage 12 field data with numerical model results 86
Figure C.12: History match of well A, stage 13 field data with numerical model results 86
Figure C.13: History match of well A, stage 14 field data with numerical model results 87
Figure C.14: History match of well A, stage 15 field data with numerical model results 87
Figure C.15: History match of well A, stage 16 field data with numerical model results 87
Figure C.16: History match of well A, stage 17field data with numerical model results 88

Figure C.17: History match of well B, stage 1 field data with numerical model results 88
Figure C.18: History match of well B, stage 3 field data with numerical model results 88
Figure C.19: History match of well B, stage 4 field data with numerical model results 89
Figure C.20: History match of well B, stage 8 field data with numerical model results 89
Figure C.21: History match of well B, stage 9 field data with numerical model results 89
Figure C.22: History match of well B, stage 10 field data with numerical model results 90
Figure C.23: History match of well B, stage 11 field data with numerical model results 90
Figure C.24: History match of well B, stage 15 field data with numerical model results 90
Figure C.25: History match of well B, stage 17 field data with numerical model results 91
Figure C.26: History match of well C, stage 1 field data with numerical model results 91
Figure C.27: History match of well C, stage 2 field data with numerical model results 91
Figure C.28: History match of well C, stage 3 field data with numerical model results 92

Figure C.29: History match of well C, stage 4 field data with numerical model results 92
Figure C.30: History match of well C, stage 5 field data with numerical model results 92
Figure C.31: History match of well C, stage 6 field data with numerical model results. 93
Figure C.32: History match of well C, stage 7 field data with numerical model results. 93
Figure C.33: History match of well C, stage 9 field data with numerical model results. 93
Figure C.34: History match of well C, stage 10 shutdown 1 field data with numerical model results. 94
Figure C.35: History match of well C, stage 10 shutdown 2 field data with numerical model results. 94
Figure C.36: History match of well C, stage 12 field data with numerical model results. 94
Figure C.37: History match of well C, stage 13 field data with numerical model results. 95
Figure C.38: History match of well C, stage 14 field data with numerical model results. 95
Figure C.39: History match of well C, stage 15 field data with numerical model results. 95
Figure C.40: History match of well C, stage 16 field data with numerical model results. 96

Chapter 1: Introduction

A sudden change in flow in a confined system results in the formation of a series of pressure pulses known as a water hammer. This name comes from the hammering sound that sometimes occurs during the event. Water hammer events arise in several areas of the petroleum industry, such as sudden valve closures of injection wells, surface facilities, or pipelines, but one of the most common and important occurrences of the water hammer takes place at the shutdown of a completed hydraulic fracture treatment. The pressure fluctuations during these events can be on the order of thousands of psi. Joukowsky (1900) carried out some of the earliest water hammer experiments. The Joukowsky equation states that a pressure increase of a water hammer is given by,

$$\Delta P = \frac{a \cdot V_0}{g} \tag{1.1}$$

where P is the pressure rise, a is the wavespeed, V is the steady-state velocity before shut-down, and g the acceleration due to gravity (Joukowsky, 1900). The time period for the pressure increase to travel to the bottom of a well and back to the surface is given by,

$$T_R = \frac{2L}{a} \tag{1.2}$$

where T_R is the reflection time, L is the length of the well, and a is the wavespeed. The figure below depicts a typical water hammer pressure response compared to the physical processes in the well-bore.

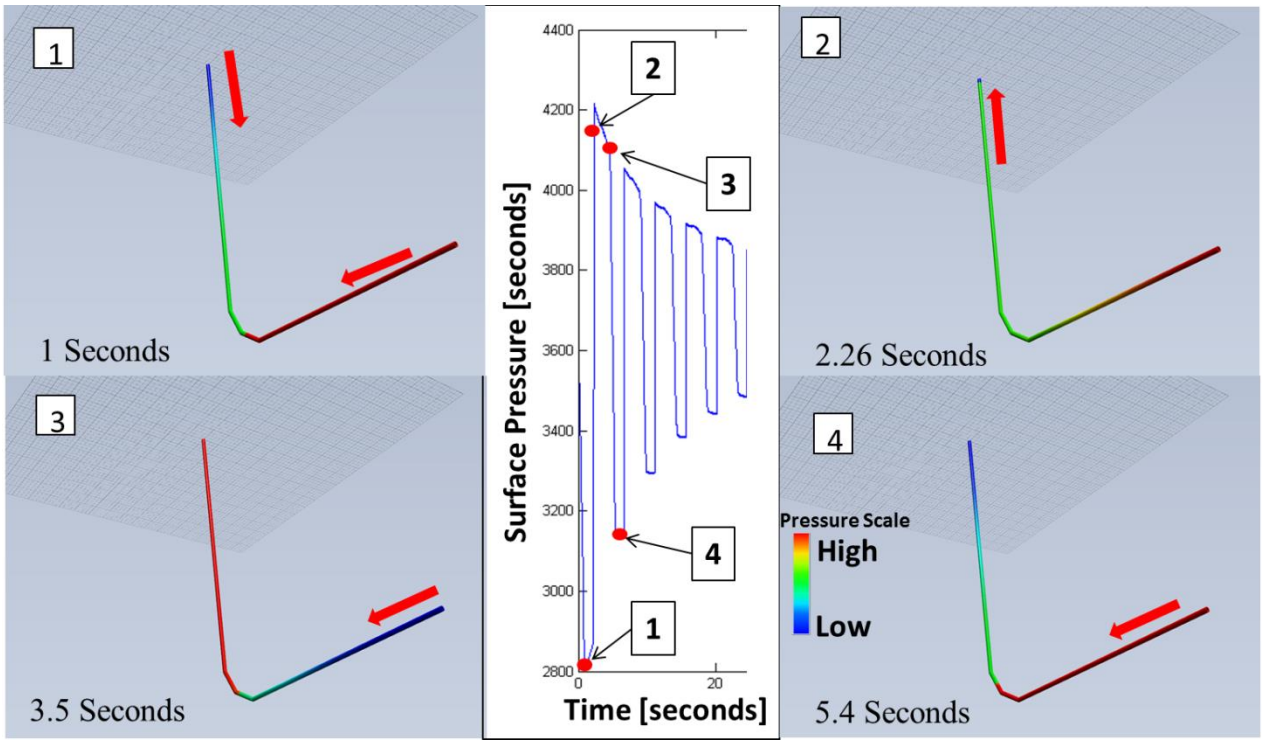

Figure 1.1: UT-Pipeflow schematic of water hammer pressure oscillations in a horizontal well

A typical water hammer pressure response compared to the physical processes in the well-bore is shown above in Fig. 1.1. The system consists of a horizontal well with constant diameter, and a fluid at an injection rate of 20 bbl/min prior to shut down. The following describes the different frames in Fig. 1.1 above:

1. At t = 1 second after shut down, the pressure at the surface is falling as the depressurized layers travel down the wellbore. The pressure near the end of the wellbore remains relatively unchanged due to the momentum of the fluid, and is thus higher than that at the surface. The higher pressure begins to move up the wellbore towards the surface.

2. At t = 2.26 seconds, the higher downhole pressure has reached the surface and the pressure oscillation is near its peak amplitude.
3. At t = 3.5 seconds, the high pressure at the surface begins to decline as the wave is reflected back downhole. The botomhole pressure is now lower than the surface pressure.
4. At t = 5.4 seconds, the low pressure pulse reaches the well-head at t=2L/a, which is known at the reflection time Tr. The low pressure pulse is then reflected back down the well-bore and the process repeats and the magnitude of the high pressure pulse attenuates due to friction.

While a majority of the water hammer research has been conducted to prevent wellbore or formation damage (Santarelli et al., 2000; Vaziri et al., 2007; Wang et al., 2008), this paper presents a way to utilize the water hammer as a means to measure hydraulic fracture parameters. The objective of this study is to prove hydraulic fractures affect the water hammer pressure pulse travel time (wavelength) and attenuation, quantify the affect, and use this relationship to estimate fracture geometry and compliance from readily available field pressure data for each fracturing stage.

1.1 LITERATURE REVIEW

1.1.1 Water Hammer Modeling

Joukowsky (1900) described water hammer phenomena with differential equations of motion, and presented water hammer equations using finite differences to solve the equations. Allievi (1902, 1913) developed the earliest analytical and graphical solutions for the basic unsteady flow equations after neglecting the friction terms. Bergeron (1935, 1936) developed a graphical solution that accounted for friction, but was limited to a single pipeline. Streeter and Wylie (1967) proposed the explicit method of

characteristics (MOC) as a method to solve water hammer equations. Bribiesca (1981) utilized matrix calculations to solve finite difference water hammer equations, and claimed it more suitable than the MOC for systems with water column separation. Shimada and Okushima (1984) solved the water hammer equations with a series solution and Newton-Raphson method. Chaudhry and Hussaini (1985) used MacCormack, Lamda, and Gabutti Finite Difference (FD) schemes to numerically solve the water hammer equations, and found second-order schemes resulted in better solutions than first-order MOC. Izquierdo and Iglesias (2002, 2004) developed a computer model to simulate transients in simple and complex pipeline systems using the method of characteristics. Silva-Araya and Chaudhury (1997) used the method of characteristics to solve the hyperbolic portion of the equations in one-dimensional form and finite differences to solve the parabolic portion in quasi-two-dimensional form. Han et al. (2002) developed a model that coupled an analytical solution of the water hammer equations with a geotechnical model to quantify the effect of well shut-downs to rock stress distributions. Ghidaoui et al. (2002) proposed a two-layer and five-layer eddy viscosity model for water hammer to estimate the accuracy of the flow asymmetry assumption by introducing a dimensionless parameter that was the ratio of the time scale of radial diffusion of shear to the time scale of wave propagation. Zhao and Ghidaoui (2003) solved a quasi-two-dimensional turbulent flow water hammer model. Zhao and Ghidaoui (2004) also formulated first and second-order Godunov-type explicit finite volume (FV) schemes for water hammer problems, and compared the results to MOC solutions for three test cases that neglected friction. They found the first-order finite volume Godunoc-type scheme produced identical results with MOC, and the second-order finite volume Godunov-type scheme required less memory and execution time than the first-order scheme. Wood (2005) developed and promoted the Wave Characteristics Method (WCM) as a

computationally less intensive alternate to the MOC that yielded virtually identical results. The WCM was based on the action of pressure waves, which represented the rapid pressure and associated flow changes that travel at sonic velocity through pipes. Greyvenstein (2006) developed an implicit finite difference method with a time step weighing factor that took into account the convective acceleration term of the momentum equation. Afshar and Rohani (2008) proposed an implicit MOC simulation method that dealt with complex boundary conditions. Mondal (2010) developed a semi-analytical model solved with the MOC that coupled the wellbore with the formation with wellbore impedance.

The previous work reviewed above shows that various methods exist to solve the water hammer equations, such as explicit and implicit Method of Characteristics, explicit and implicit finite difference, finite volume and finite element methods. Each method has advantages and disadvantages, however, the explicit MOC is the most popular method of solution because it is simple to code, accurate, and efficient (Mondal 2010). Thus, this current research utilizes the MOC approach.

1.1.2 Friction Calculations

Calculated friction losses are needed to accurately determine the attenuation of the water hammer signal. The simple, general method for calculating friction losses in transient flows uses equations developed for steady-state conditions, such as the Darcy-Weisbach formula for friction where the calculations for mean flow velocity assume that the shear stress at the wall is the same for both steady-state and unsteady flow conditions (Mondal 2010). The assumption of steady viscous losses may be satisfactory for slow transients where the wall shear stress has a quasi-static behavior, but previous investigations of the behavior of steady friction models for rapid transients showed large

discrepancies in attenuation, shape, and timing of pressure traces when computational results were compared with measurements (Bergant et al. 2008). To account for these large discrepancies, MOC solutions incorporated unsteady friction models. Zielke (1968) proposed a convolution based frequency dependent calculation method of unsteady friction for laminar flows that was very computationally intensive, however, Trikha (1975) improved the computational speed of Zielke's model by incorporating approximate expressions for Zielke's weighting functions. Vardy and Brown (2004) built on the previous work of Trikha, and created computationally faster solutions valid for both laminar and turbulent flow. Vardy and Hwang (1991) developed a five-region turbulence model in which each region had a different expression to compute the eddy viscosity distribution. Silva-Araya (1993) included an energy dissipation term for laminar and turbulent unsteady friction computations. Brunone et al. (1991) developed a model where the total friction was the sum of a quasi-steady friction term and an unsteady friction term that depended on the instantaneous local and convective acceleration. Bergant et al. (2001) incorporated both the unsteady friction models by Zielke (1968) and Brunone et al. (1991) into the MOC and compared the results against experimental values, and found the Brunone model to be computationally efficient. Saikia and Sarma (2006) developed a numerical model with the MOC that included unsteady friction calculated at each time step with the Barr's (1980) explicit friction factor correlation.

1.1.3 Fracture Impedance

While very little work has been done analyzing water hammer signals from hydraulic fracture treatments for fracture diagnostics, quite a bit of work has been done with fracture impedance. Khalevin (1960), Walker (1962), and Morris et al. (1964) confirmed that acoustic waves can detect wellbore fractures. Mathieu (1984) postulated

that the presence of a fracture changed the wellbore acoustic impedance, and derived analytically that Stoneley waves could be used to detect hydraulic fractures. Furthermore, Mathieu coined the term "fracture impedance", and derived the reflection and transmission coefficients for waves in a fractured wellbore. Holzhausen et al. (1985) proposed the method of Hydraulic Impedance Testing (HIT), which consisted of sending a single artificially induced pressure pulse downhole from the surface and analyzing the reflected pressure oscillations. The HIT method used an equivalent circuit model to estimate fracture impedance from the reflected pressure pulse, in which the pulse amplitude was used to compute fracture conductivity and height, and fracture length was determined from the difference in arrival times from the pressure pulse. Paige et al. (1992) confirmed the validity of Holzhausen's HIT model experimentally, and several field tests were conducted (Paige et al., 1993; Holzhausen and Egan, 1986). Ashour (1994) utilized Holzhausen's HIT method for vertical and horizontal fractures and found that a more accurate estimation of fracture parameters was achieved if the input pressure pulse could produce a resonant motion of the fluid in the fracture.

1.1.4 Water Hammer Period

As shown previously in Equation 1.2, the pressure pulse travel time, which is the period between water hammer pressure oscillation peaks, can be calculated in a pipe given the length and wavespeed. Holzhausen et al. (1985) analyzed pressure data gathered by Ferrick et al. (1982) for a fractured and unfractured well, and confirmed that hydraulic fractures alter the water hammer period by inducing a constant pressure boundary at the bottom of the well which effectively doubles the water hammer period from $2L/a$ to $4L/a$. Paige et al. (1992) conducted HIT laboratory experiments and did not observe a doubling of the water hammer period. Furthermore, Paige claimed that with

high-frequency pressure transducers (100 samples/second) the separate reflections from the fracture mouth and tip were detectable, and fracture length could be determined from the time lapse between pulses. Patzek et al. (1999) also proposed that the water hammer pressure pulse travel time was consistent with Equation 1.2 through both HIT experiments and simulations, and concluded that hydraulic fractures do not affect the water hammer period.

Both the work by Paige et al. (1992) and Patzek et al. (1999) suggest water hammer oscillations occur at a period of $T = 2L/a$ during a HIT, however the data analyzed by Holzhausen et al. (1985) is contradictory. The disagreement may arise due to the methods by which the water hammer pulses were generated. HIT's induce a pressure pulse by quickly dropping or increasing the pump rate for a very short time period before returning to the original pump rate, while a quick shut-down, which was the source for the Ferrick et al. (1982) water hammer data, produces a water hammer pulse by suddenly dropping the rate from some value to zero. This thesis will attempt to clarify this phenomenon through simulations.

Chapter 2: Water Hammer Characteristics Study

2.1 Water Hammer Study Introduction

Post shut-in water hammer pressure signals from hydraulically fractured wells were analyzed. The period, amplitude, and decay rate of the pressure signal were the three characteristic properties chosen for analysis. The three characteristic properties were compared to production log and micro-seismic SRV data to identify any correlations.

2.2 Water Hammer : Some Characteristic Properties

A graphical representation of the period, amplitude, and decay rate are shown below in Fig. 2.1.

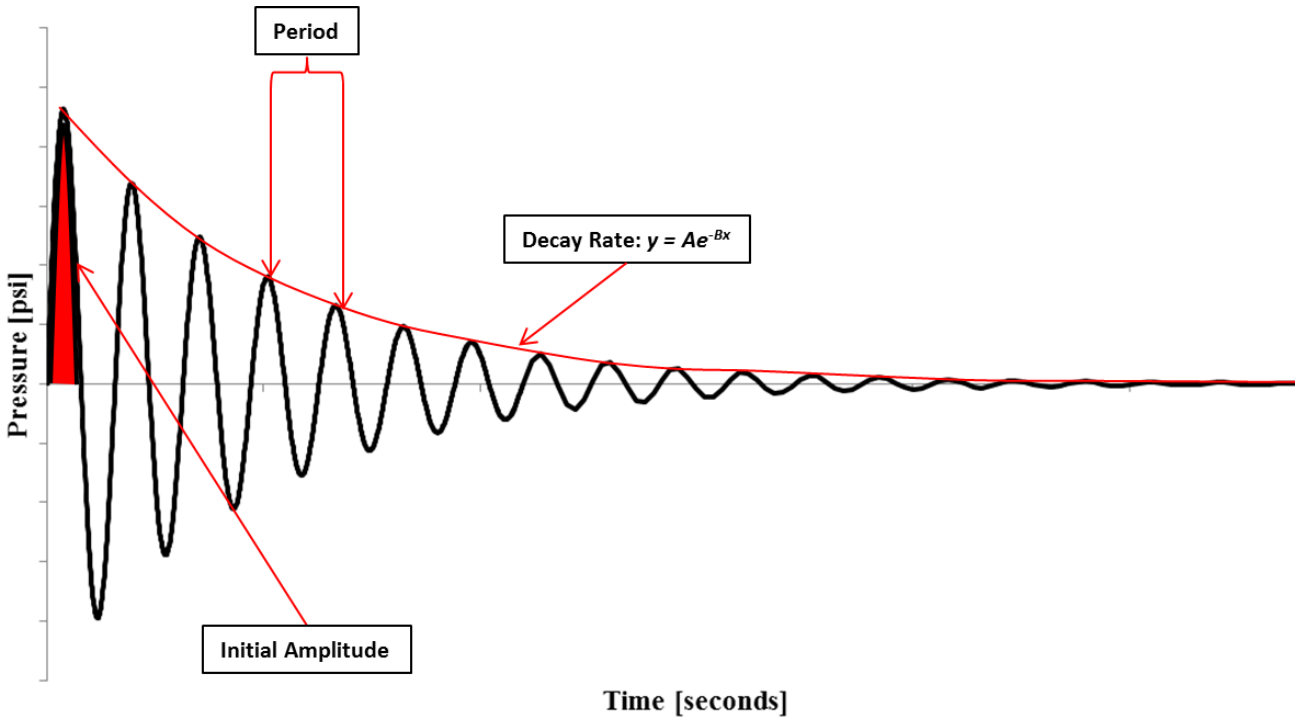

Figure 2.1: Water hammer characteristic properties.

2.2.1 Period

The period, or inverse of frequency, was determined by the distance between peaks or troughs of the water hammer pressure signal, and had the units of seconds.

2.2.2 Amplitude

The amplitude of the water hammer signal was half the difference between a pressure oscillation peak and consecutive trough. Amplitude was included in this study as both the initial amplitude, which was the magnitude of the first water hammer pressure oscillation, and the average amplitude, which was taken over the entire pressure oscillation sequence.

2.2.3 Decay Rate

The water hammer decay rate was determined by fitting the decaying pressure signal to an exponential function $y = Ae^{-Bx}$ and extracting the exponent B. A larger B exponent indicated a larger decay rate, shown below in Fig. 2.2.

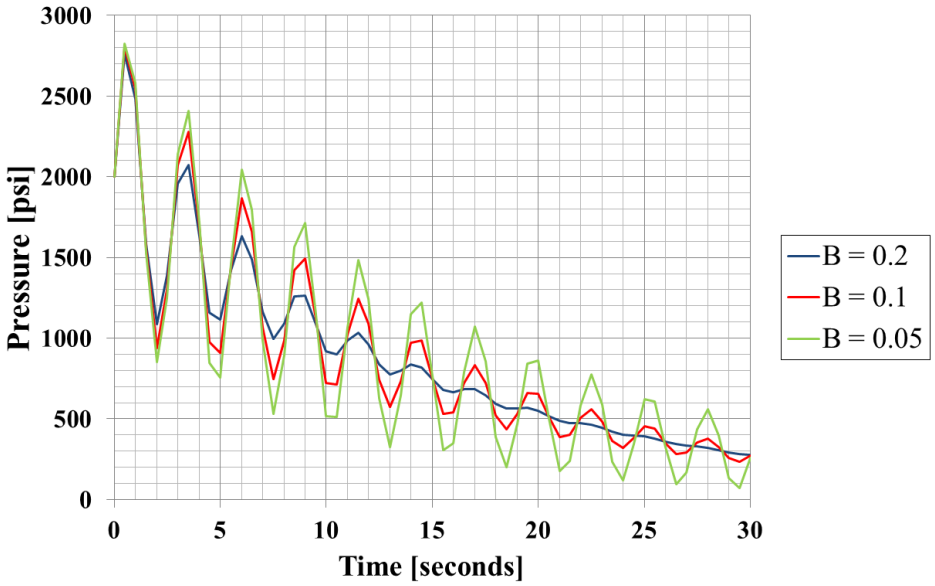

Figure 2.2: An example pressure signal showing several water hammer decay rates.

2.3 PRODUCTION LOG AND SRV DATA

Production log and SRV data was used as s successful fracture indicator, with high production or a large SRV indicating a more successful fracture treatment and low production or a smaller SRV indicating a less successful fracture treatment.

2.3.1 Production Log Data

Production data was obtained from a combination of spinner and FSI logs for 16 wells for a total of 187 stages, of which 136 stages were slickwater treatments and 51 stages were cross-linked gel treatments. Since the production data consisted predominantly of natural gas wells with a small number of oil and water producing wells, the gas production in Mscfd was the primary production indicator, and ranged from 0 Mscfd to 400 Mscfd with an average of 94 Mscfd.

2.3.2 SRV Data

SRV data was obtained from micro-seismic information analyzed with PETREL for only 3 wells for a total of 50 stages, and indicated the volume of rock affected by the hydraulic fracture treatment. All 50 stages were slickwater treatments. The SRV volume was estimated by defining the SRV as the region in which measureable microseisms were recorded. We recognize that this is an imperfect definition of SRR since not all the shear failure events contribute to production and not all the events are measurable. However, this definition is used as a matter of necessity and provides a consistent approximation estimate of the stimulated volume. The volume of the SRVs ranged from 1.5×10^6 to 3.89×10^8 ft^3 with an average of 8.17×10^7 ft^3.

2.4 STUDY RESULTS AND DISCUSSION

Water hammer period, amplitude, and decay rate were compared to gas production and SRV data to find any correlations that would enable the water hammer

pressure signal to indicate effective fracture treatments. Slickwater treatments are noted by blue data points on the plots while cross-link gel treatments are distinguished by red data points.

2.4.1 Period

Water hammer period compared to gas production and SRV values are shown below in Fig. 2.3 and Fig. 2.4 respectively. There were no strong correlations between the water hammer period and production or SRV data. Water hammer period, however, correlated strongly with plug measured depth, shown below if Fig. 2.5. This correlation exists because the water hammer period is directly related to the length of the pipe, discussed earlier with Equation 1.2. To eliminate this correlation, the water hammer period was normalized by measured depth and compared to gas production and SRV data, shown below in Fig. 2.6 and Fig 2.6 respectively, however there were no strong correlations.

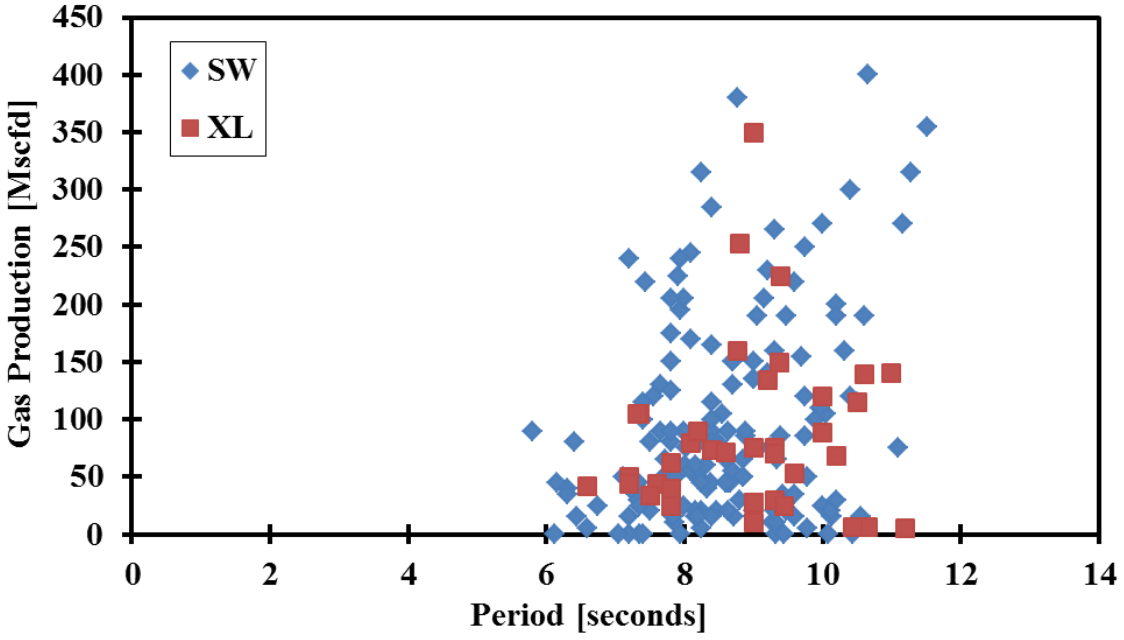

Figure 2.3: Water hammer period versus gas production

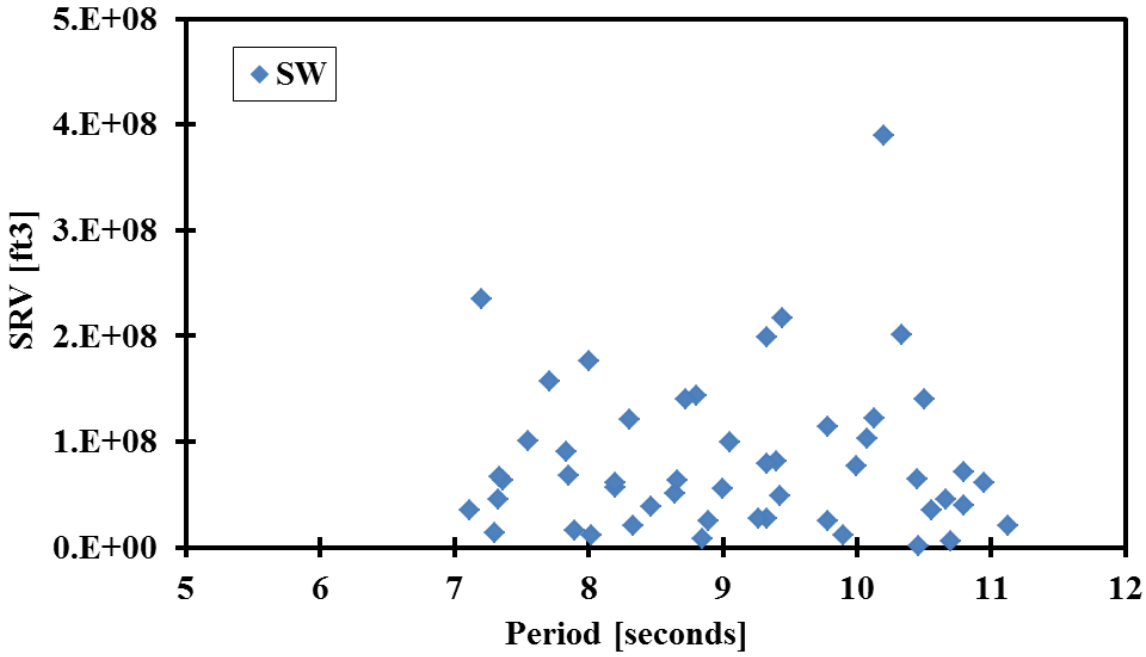

Figure 2.4: Water hammer period versus SRV

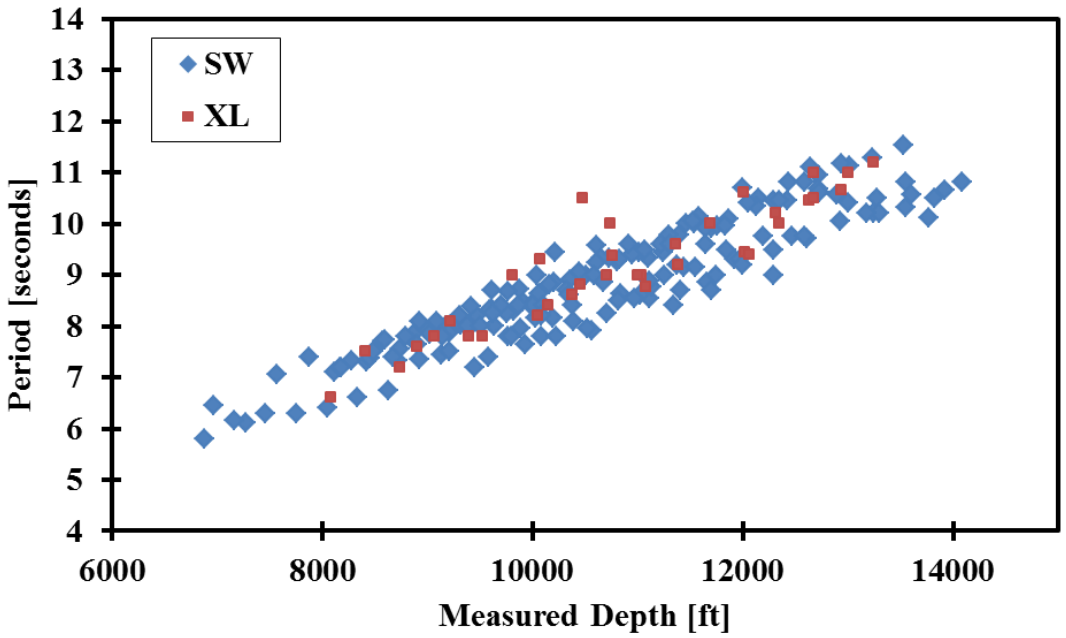

Figure 2.5: Measured depth versus water hammer period

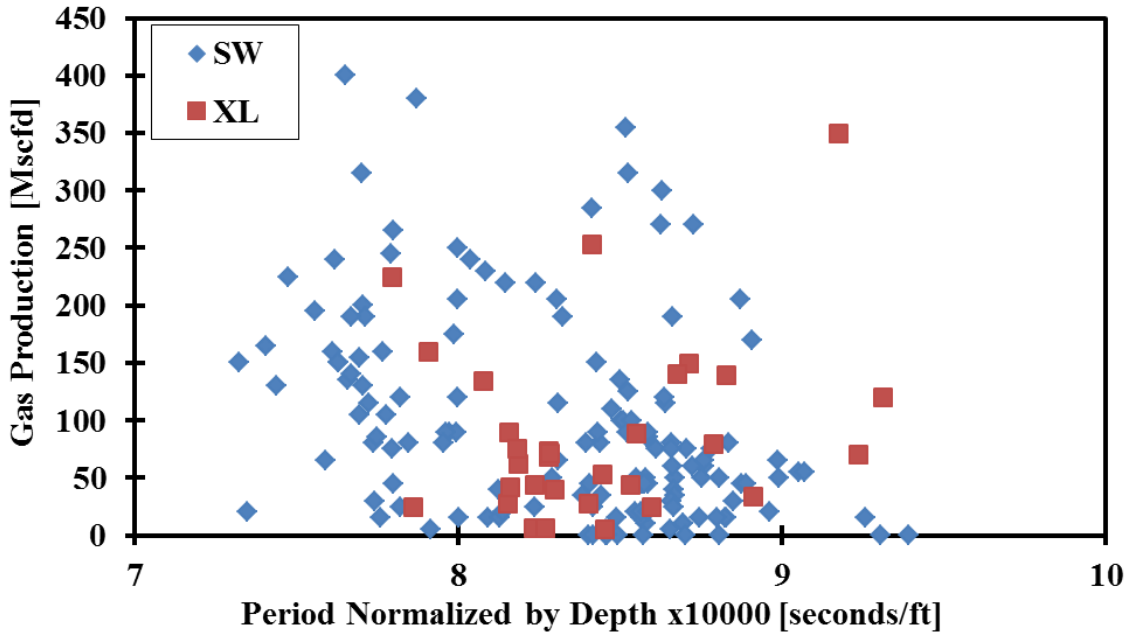

Figure 2.6: Water hammer period normalized by depth versus gas production

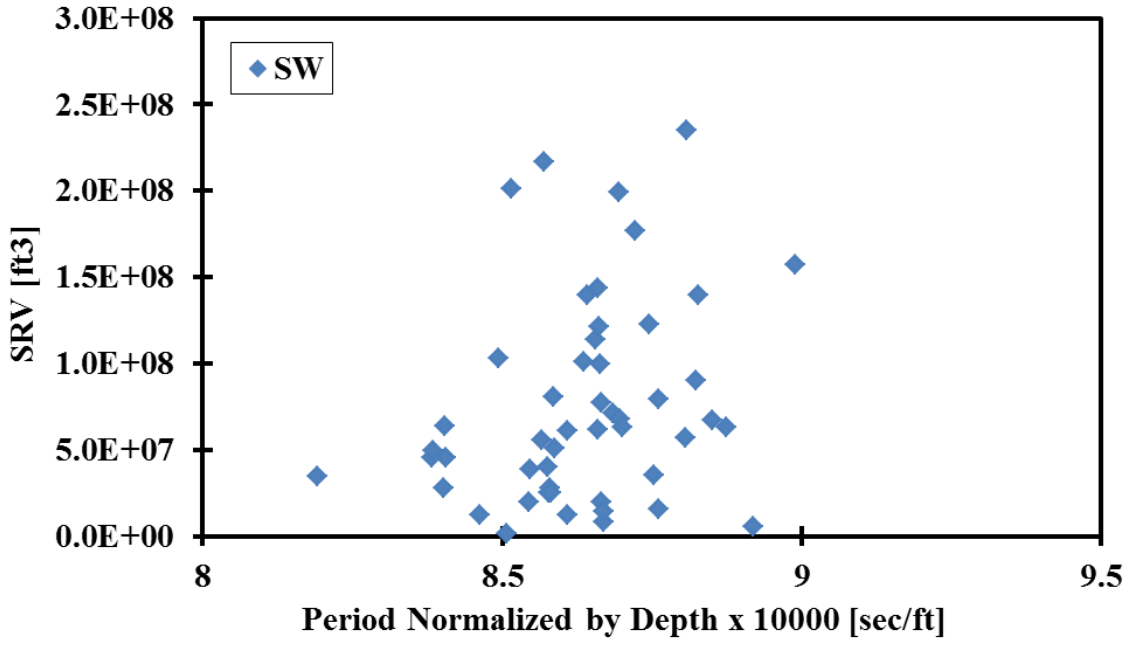

Figure 2.7: Water hammer period normalized by depth versus SRV

2.4.2 Amplitude

Initial and average amplitude of the water hammer pressure signal compared to production data are shown below in Fig. 2.8 and Fig. 2.9 respectively. There was no correlation between the initial amplitude and production data shown in Fig. 2.8. This is due to the initial amplitude being dominated by the magnitude of the injection rate prior to shutdown, with a higher injection rate yielding higher initial amplitude. There was no strong correlation between the production data and average amplitude, which is shown below in Fig. 2.9. Initial and average amplitude compared to SRV are shown below in Fig. 2.10 and Fig. 2.11 respectively, and no correlations between either variable exists. Average amplitude normalized by injection rate versus SRV is shown below in Fig. 2.12, and shows no correlation.

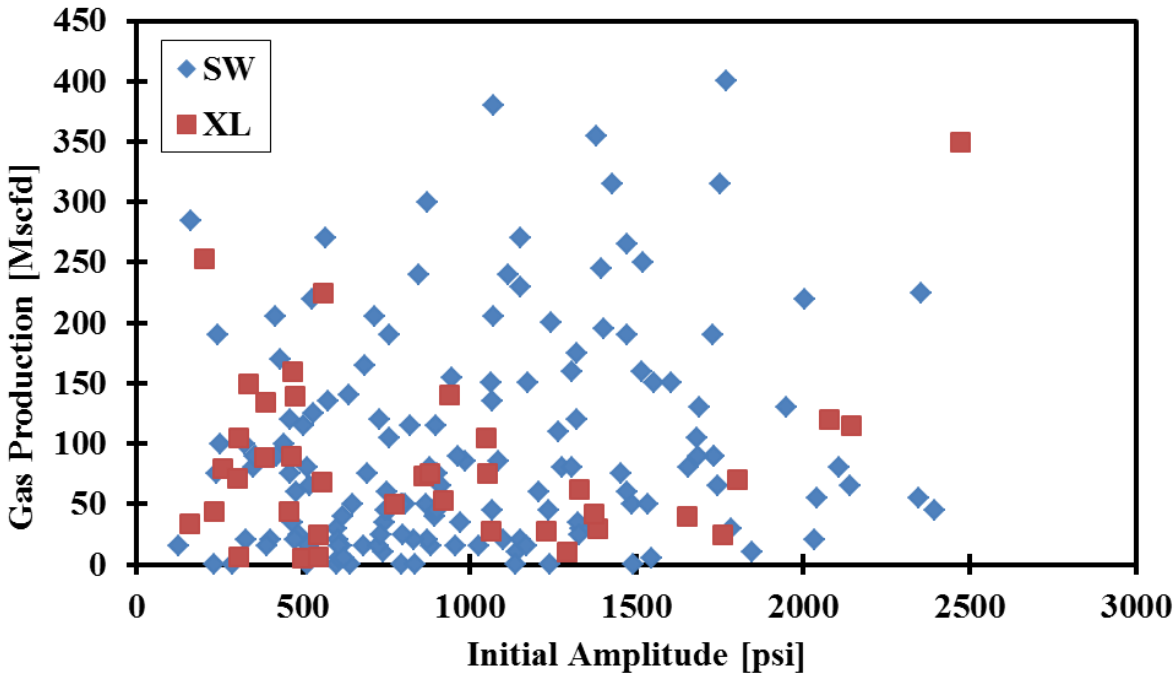

Figure 2.8: Initial water hammer amplitude versus gas production

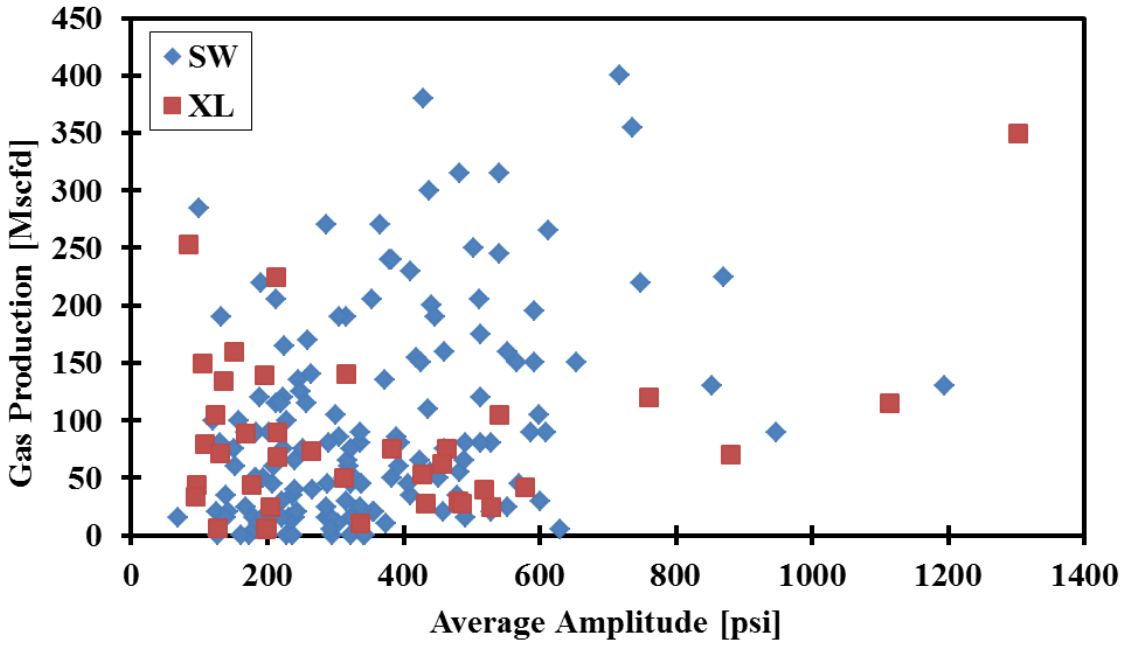

Figure 2.9: Average water hammer amplitude versus gas production

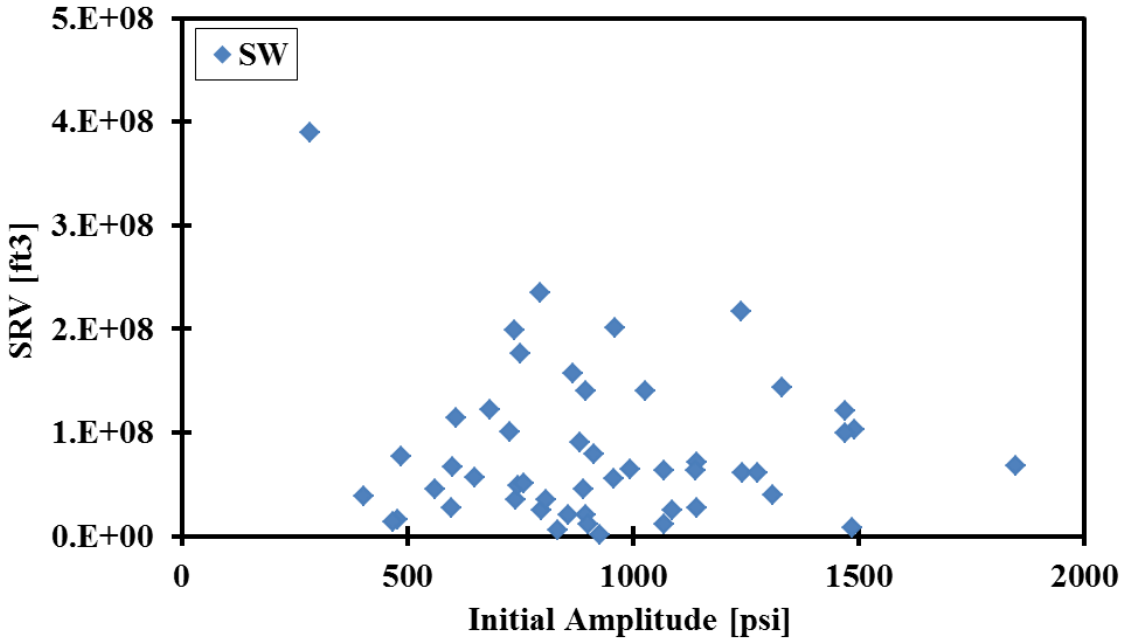

Figure 2.10: Initial water hammer amplitude versus gas production

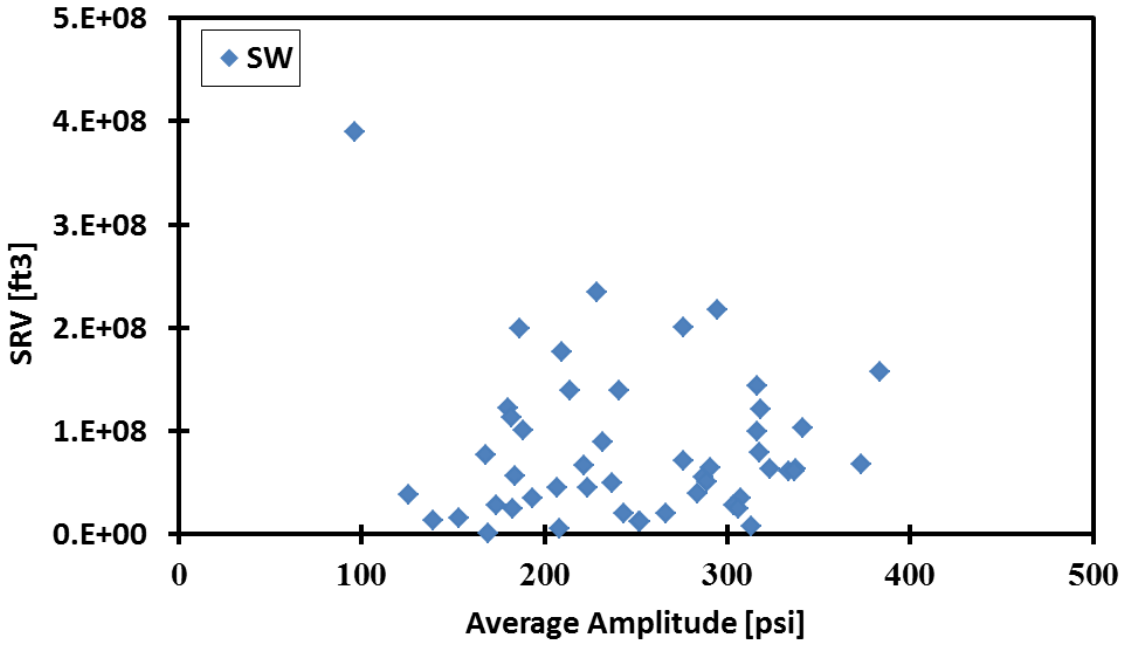

Figure 2.11: Average water hammer amplitude versus SRV

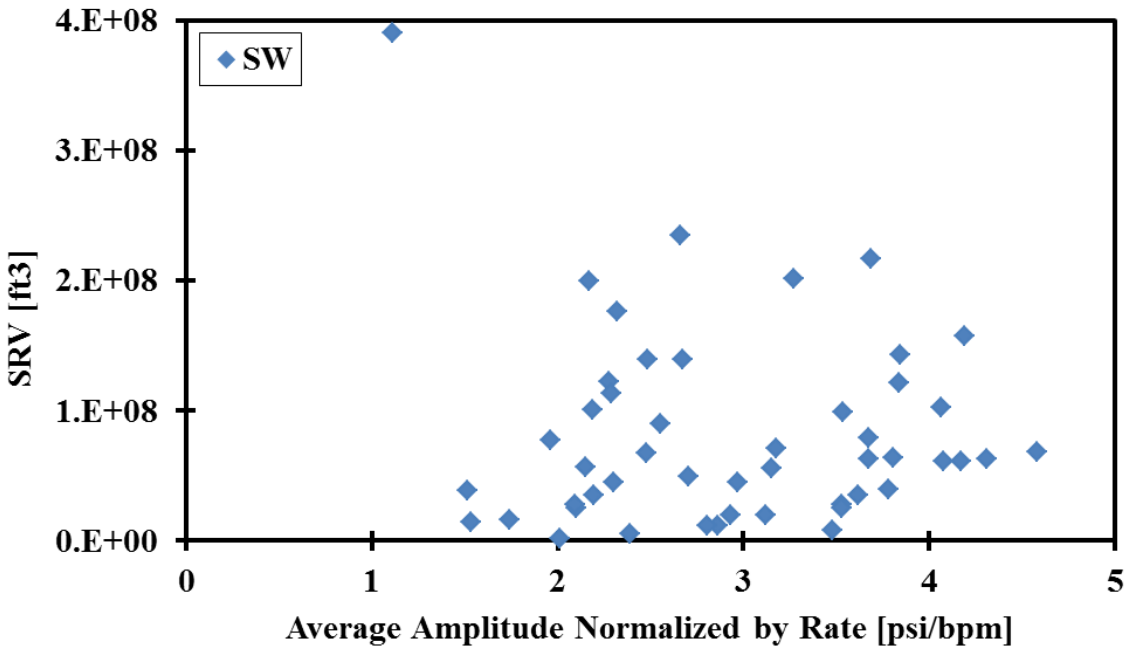

Figure 2.12: Average water hammer amplitude normalized by injection rate prior to shutdown plotted versus SRV

2.4.3 Decay Rate

The decay rate exponent compared to production data is shown below in Fig. 2.13. While there was no strong correlation between decay rate and gas production, the cross-link treatments on average have a larger decay, shown by a majority of the cross-link treatments in the right-hand portion of Fig. 2.13. This is due to the higher fracture widths created with gel treatments and the high viscosity gel within the fractures dampening out the pressure waves.

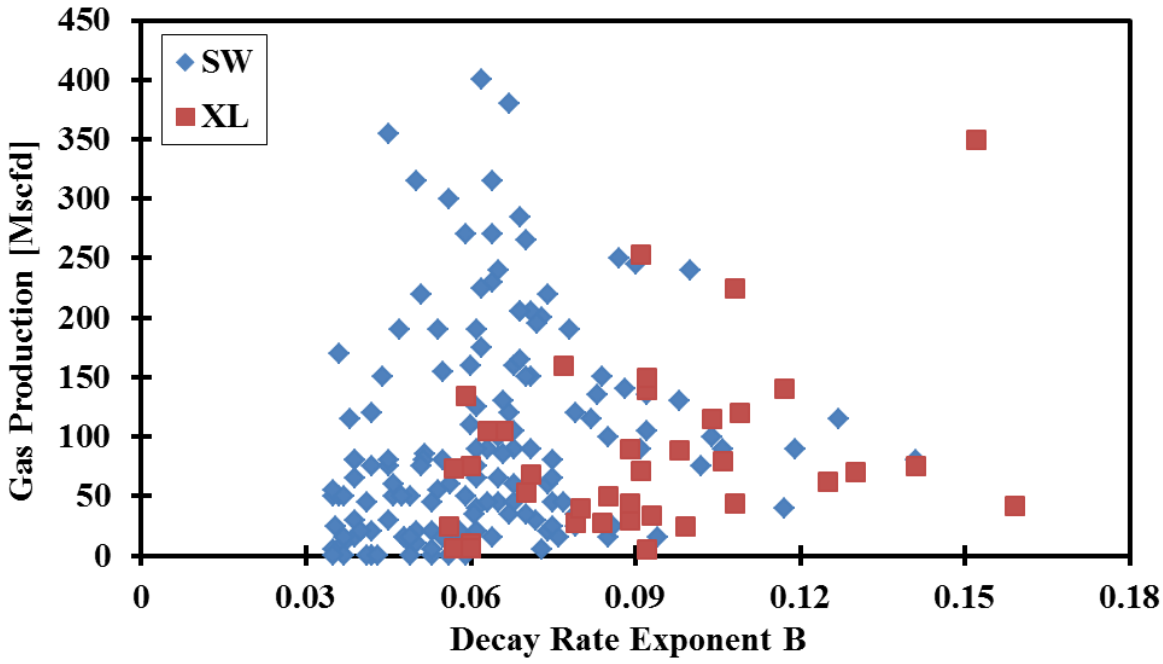

Figure 2.13: Decay rate exponent *B* versus gas production

SRV data compared to decay exponent B are shown below in Fig. 2.14. All 50 stages with SRV data were slickwater treatments. There is a slight negative trend in the SRV versus decay rate data, which suggests water hammer signals that have a slower decay rate, denoted by a smaller decay exponent *B*, correlate to treatment zones with

larger fractures or stimulated volume. This relationship becomes more apparent when SRV data is plotted versus water hammer duration, which is the amount of time the water hammer signal oscillates before attenuating, shown below in Fig 2.15. Larger durations correlate to larger stimulated volumes.

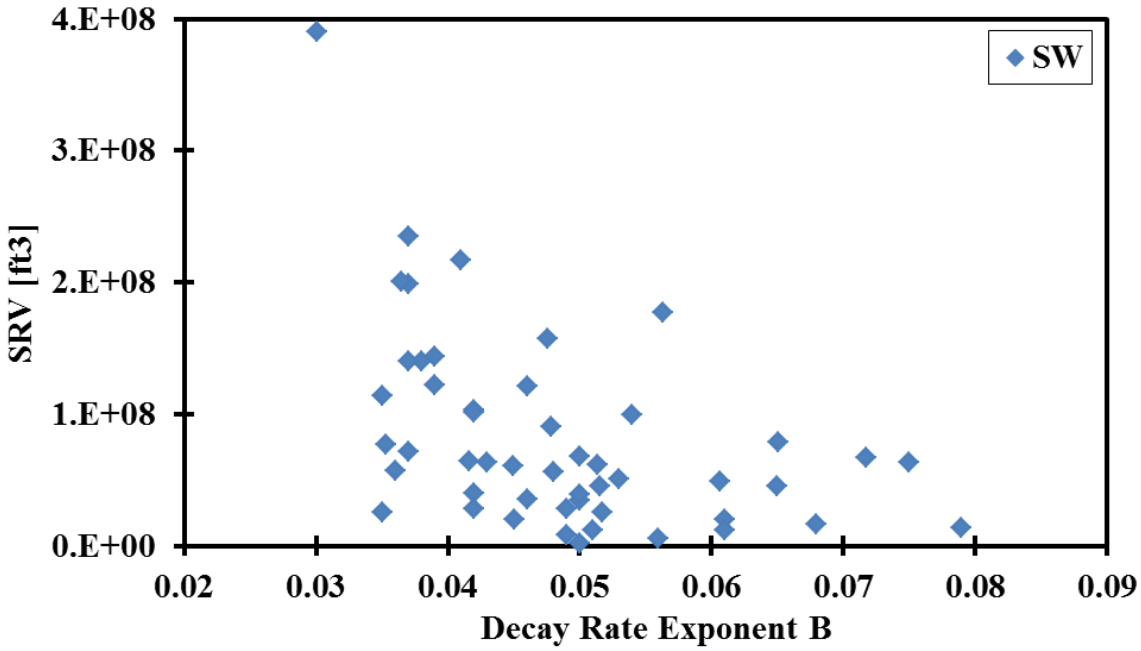

Figure 2.14: Decay rate exponent *B* versus SRV

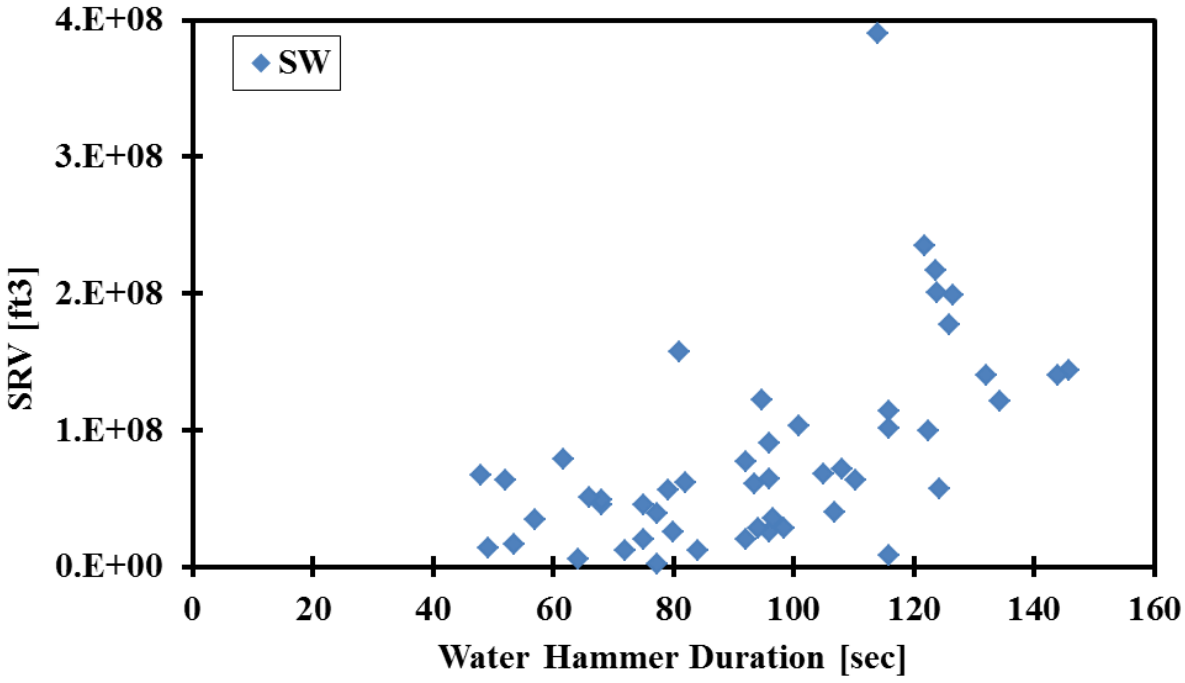

Figure 2.15: Water hammer duration versus SRV

Holzhausen et al. (1985) observed a similar phenomenon when performing a hydraulic fracture treatment. Several shut-downs were executed at various times during the treatment and the water hammer pressure oscillations were compared, shown below in Fig. 2.16. As the injected volume increased, the duration of the water hammer oscillations increased. Holzhausen et al. (1985) concluded that changing fracture dimensions affects the amplitude and duration of the water hammer pressure oscillations.

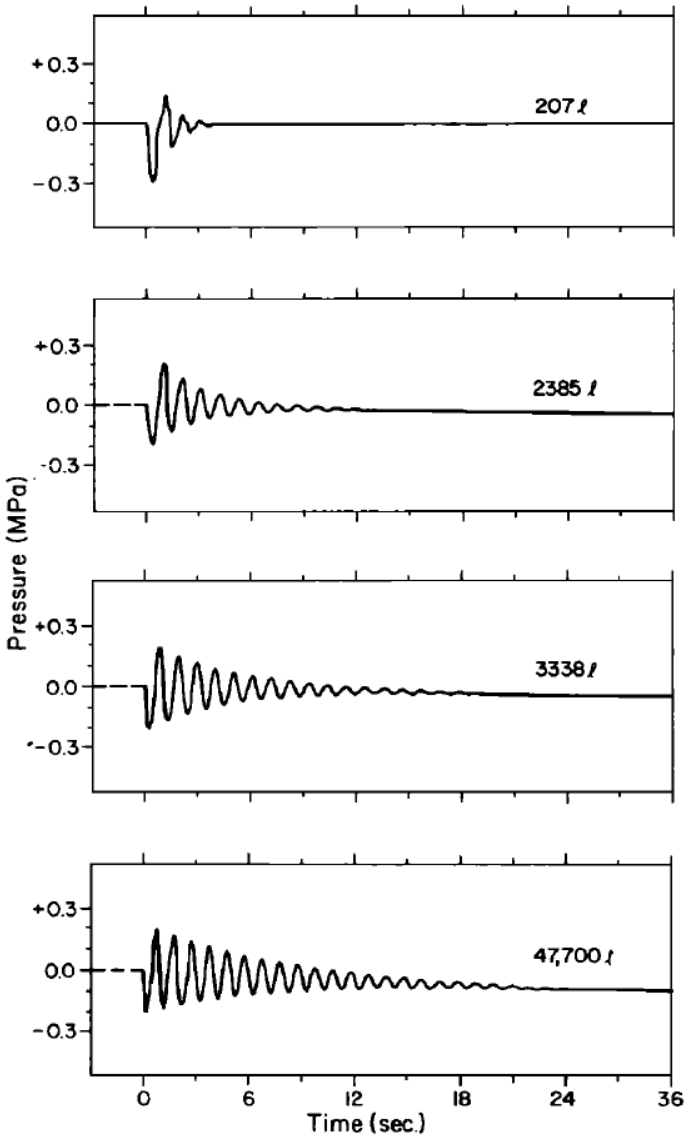

Figure 2.16: Water hammer pressure oscillations after 207, 2385, 3338, and 47,700 Liters were pumped during a hydraulic fracture treatment (From Holzhausen et al., 1985)

2.5 PERIOD DISCREPANCY AND ERROR

There was a notable difference between the water hammer period of the fractured well field data and the period calculated from Eq. (1.2), shown in Fig. 2.17 below.

Field Data Period:	Period Calculation:
Measured Depth = 10805 [ft] Period = 9.27 [sec]	$\text{Period} = \frac{2 \cdot Depth}{Wavespeed}$ Depth = 10805 [ft] Wavespeed = 4621 [ft/sec] Period = 4.68 [sec]

Figure 2.17: Field data water hammer period compared to water hammer period calculated from Eq. (1.2)

There are two possibilities for this occurrence: 1) The frequency of the pressure measurements is not fine enough to capture the true period of the water hammer, or 2) the created fractures from the stimulation significantly alter the water hammer period.

2.5.1 Field Data Under Sampling

Typical hydraulic fracturing operations measure surface pressure data every 1 to 5 seconds, which may not be of high enough resolution to capture the true water hammer period, shown below in Fig. 2.18.

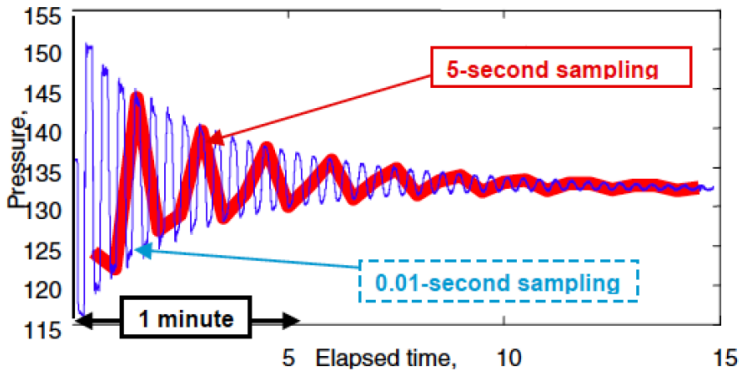

Figure 2.18: How under sampling may alter the observed water hammer period (From Wang et al., 2008)

While the 5 second sampling in Fig. 2.18 drastically alters the observed water hammer, this study's data was acquired at 1 second intervals. To test the validity of the this data's observed water hammer period, synthetic data with a 4 second period was generated at 1/10th second intervals and compared to the same data sampled at 1 second intervals, shown below in Fig. 2.17. The 1 second data reasonably captured the water hammer period in Fig. 2.17. Thus, the water hammer oscillation periods determined from this study's field data were assumed to be within reason. While the true period is observable at the 1 second sampling, all fine-scale events such as reflections from the fracture mouth or tip will not be visible, and it is suggested high resolution data be used for any further studies.

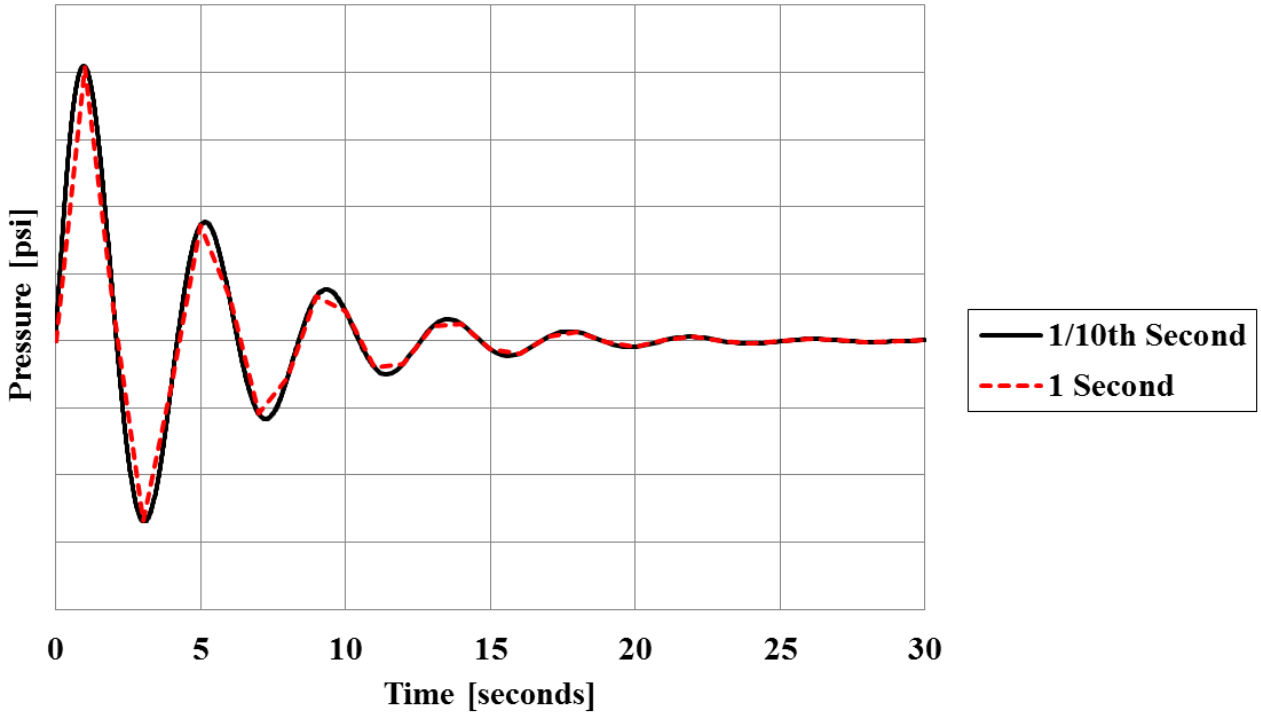

Figure 2.17: Water hammer data generated at 1/10th second intervals and sampled at 1 second intervals to investigate under sampling effects

2.5.2 Fractures Alter Period

If the observed field data water hammer periods are accurate and significantly different from the expected calculated values, the created hydraulic fractures may alter the water hammer pressure signal. Holzhausen et al. (1985) proposed hydraulic fractures affect the water hammer period by imposing a constant pressure boundary condition at the bottom of the well, which doubles the water hammer period from $2L/a$ to $4L/a$. Data gathered by Ferrick et al. (1982) and analyzed by Holzhausen et al. (1985) is shown below in Fig. 2.18, and supports Holzhausen's hypothesis. The doubling of the period occurs since when the low-pressure wave reaches the bottom of the well at time L/a, fluid is drawn into the well in order to maintain the condition of constant pressure, which is to be expected from a hydraulic fracture with large capacitance or storage.

Two trends in this study's data support Holzhausen's hypothesis. First, 68% of the stages have a water hammer period within 10% of the predicted $4L/a$, shown below in a cumulative histogram in Fig. 2.19. Lastly, there is a noticeable difference in the average decay rate of cross-link and slickwater fracture fluid treatments. During the fracture treatment, the cross-link gel is swept out of the wellbore to the perforations, and water occupies the wellbore while gel and proppant fill the created fracture, as shown in Fig. 2.20 below.

The noticeable difference in decay rates between slickwater and cross-link gel treatments when the only difference is the fluid within the fracture means the created hydraulic fractures are 1) in communication with the wellbore, and 2) have an effect on the water hammer pressure signal.

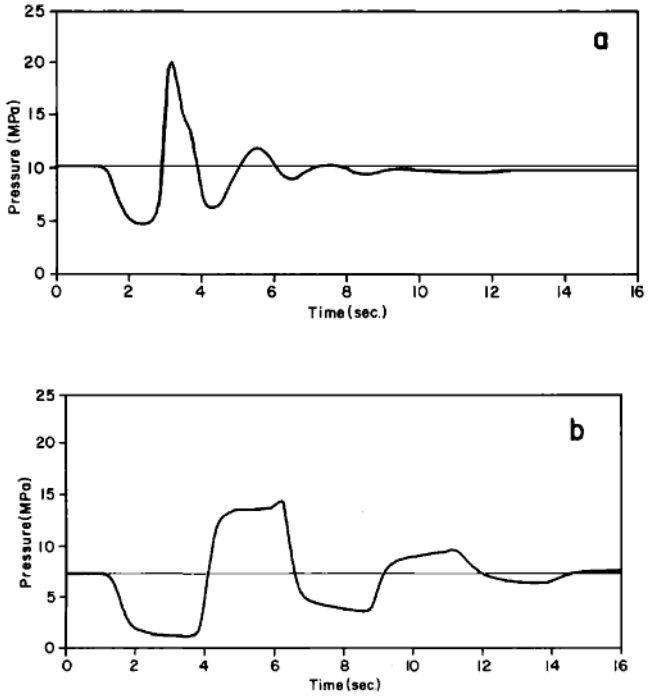

Figure 2.18: Free oscillations observed in a 1589 m deep well a) prior to and b) after fracturing. The period shifts from 2*L*/*a* in the unfractured case to 4*L*/*a* in the fracture case. (From Ferrick et al., 1982)

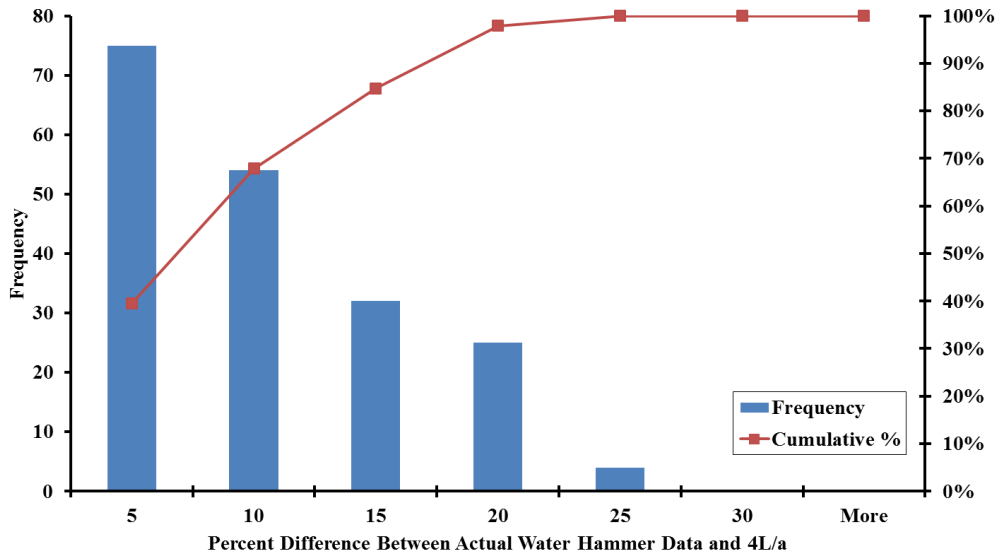

Figure 2.19: Histogram of percent difference between field water hammer period and Holzhausen's predicted 4*L*/*a*

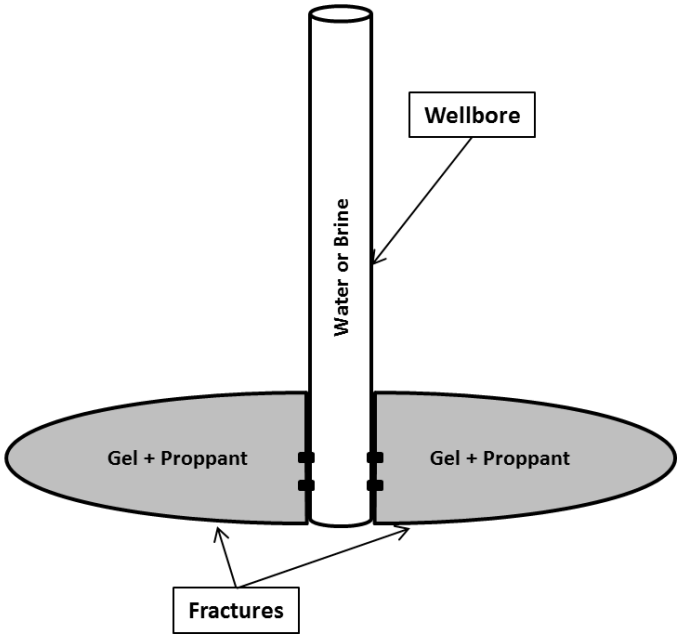

Figure 2.20: Fluid distributions after a gel hydraulic fracture treatment

2.6 CONCLUSIONS FROM CHARACTERISTICS STUDY

Several water hammer characteristic properties were analyzed and compared to production and SRV data. The production log data was found to be a poor indicator of fracture effectiveness due to the strong dependence on geology. Of the water hammer characteristic properties, the water hammer decay rate showed the only correlation with SRV data, and exhibited an inverse relationship. A discrepancy close to a factor of 2 between the observed water hammer period and the calculated theoretical period of $2L/a$ was observed and suggests hydraulic fractures alter the water hammer period. Holzhuasen et al. (1985) reported similar findings, and proposed that large fractures alter the water hammer period from $2L/a$ to $4L/a$ by acting as a constant pressure boundary due to the large capacitance. Thus, it may be possible to determine hydraulic fracture dimensions based on a particular well's water hammer period between $2L/a$ and $4L/a$.

Chapter 3: Model Formulation

3.1 WATER HAMMER MODELING EQUATIONS

Transient flow behavior in a closed conduit is governed by the one-dimensional equations of motion and continuity (Bird et al., 2007). The general forms of the equations of motion and continuity were derived using Reynolds transport theorem (Chaudhury, 1987). Wylie and Streeter (1993) have also documented a thorough derivation in the literature. Below is an explanation of the derivation and the assumptions used by Chaudhury (1987) and Wylie and Streeter (1993) to derive the governing equations for water hammer analysis.

3.1.1 Equation of Motion

The general form of the equation of motion is obtained from a momentum balance over a volume element within a pipe, is Chaudhury (1987),

$$\frac{\partial V}{\partial t} + V\frac{\partial V}{\partial x} + \frac{1}{\rho}\frac{\partial p}{\partial x} + g\sin\theta + \frac{fV|V|}{2D} = 0 \tag{3.1}$$

where, V = mean flow velocity, t = time, x = distance along pipe axis, ρ = density of fluid within pipe, p = pressure intensity, g = gravitational acceleration, θ = angle of inclination of the pipe, f = Darcy-Weisbach friction factor, and D = pipe diameter.

The convective transport term in Eq. (3.1), $V\,\partial V/\partial x$, is neglected for low Mach-number unsteady flows, reducing the equation to

$$\frac{\partial V}{\partial t} + \frac{1}{\rho}\frac{\partial p}{\partial x} + g\sin\theta + \frac{fV|V|}{2D} = 0 \tag{3.2}$$

3.1.2 Continuity Equation

The general form of the continuity equation is obtained from a mass balance over a fixed pipe control volume, Chaudhury (1987),

$$\frac{1}{\rho}\frac{d\rho}{dt}+\frac{1}{A}\frac{dA}{dt}+\frac{\partial V}{\partial x}=0 \tag{3.3}$$

where, A = pipe cross-sectional area. The first term in Eq. (3.3) describes the fluid compressibility, the second term represents the pipe wall deformation rate, and the last term describes the accumulation rate.

With the assumption of an elastic pipe filled with a slightly compressible fluid Eq. (3.3) simplifies to

$$\frac{\partial p}{\partial t}+V\frac{\partial p}{\partial x}+\rho a^2\frac{\partial V}{\partial x}=0 \tag{3.4}$$

where, a = wave speed of the water hammer waves. The convective transport term in Eq. (3.1), $V\,\partial V/\partial x$, is neglected for low Mach-number unsteady flows, reducing the continuity equation to

$$\frac{\partial p}{\partial t}+\rho a^2\frac{\partial V}{\partial x}=0 \tag{3.5}$$

Pipe flows are often analyzed by describing pressure, p, and velocity, V, in terms of piezometric head, H, and discharge, Q, respectively, shown below in Eq. (3.6) and Eq. (3.7).

$$H=\frac{p}{\rho g}+z \tag{3.6}$$

$$Q=VA \tag{3.7}$$

where p = pressure, ρ = density, g = acceleration due to gravity, z = pipe elevation above a specified datum, A = pipe cross-sectional area, and V = mean flow velocity.

In terms of H and Q, Eqs. (3.2) and (3.4) become,

$$\frac{\partial Q}{\partial t} + gA\frac{\partial H}{\partial x} + \frac{fQ|Q|}{2DA} = 0 \tag{3.8}$$

$$\frac{\partial H}{\partial t} + \frac{a^2}{gA}\frac{\partial Q}{\partial x} = 0 \tag{3.9}$$

3.1.3 Water Hammer Wave Speed

The water hammer wave speed within a wellbore was presented by Halliwell (1963) as,

$$a = \sqrt{\frac{K/\rho}{1+(K/E)\psi}} \tag{3.10}$$

where K = bulk modulus, ρ = density, E = Pipe Young's modulus of elasticity, and Ψ = non-dimensional variable that depends on the pipe elastic properties.

The non-dimensional parameter Ψ is defined for various scenarios (rigid pipe, thick-walled elastic pipes, thin-walled elastic pipes, tunnels through solid rock, etc.) in the literature (Chaudury, 1987; Wylie and Streeter, 1993). For this analysis, the parameter Ψ was determined in the wellbore from the expression for a thin-walled elastic pipe anchored against longitudinal movement, given as,

$$\psi = \frac{D}{e}\left(1-v^2\right) \tag{3.11}$$

where D = pipe diameter, e = wall thickness, v = pipe Poisson's ratio.

Holzhausen et al. (1985) determined that fractures have a considerably slower wavespeed than the wellbore due to fracture compliance, and derived the following expression for fracture wavespeed using the results of Sneddon (1946)

$$a = \sqrt{\frac{\pi b G}{2\rho h(1-\nu)}} \tag{3.12}$$

where b = is fracture half-width, G = rock bulk shear modulus, ρ is fluid density, h is fracture half-height at the wellbore, and ν is rock Poisson's ratio.

3.2 USING THE METHOD OF CHARACTERISTICS

The derived water hammer equations (Eq. (3.8) to (3.9)) are quasi-linear, hyperbolic, partial differential equations without a closed-form solution (Wylie and Streeter, 1993). These equations, however, can be numerically integrated through a variety of techniques, such as explicit and implicit finite-difference approaches, finite-element methods, and the method of characteristics (Ghidaoui et al. 2005). The method of characteristics is the most popular method for its simplicity and superior performance because it can solve complex pipe networks, has an established stability criterion, is easy to program, and has accurate solutions (Wylie and Streeter, 1993; Afshar et al., 2008). The main disadvantage of the MOC is the requirement to adhere to the time step-distance interval relationship for stability (Mondal, 2010).

The momentum and continuity partial differential equations are transformed into four ordinary differential equations by the MOC. Wylie and Streeter (1993) begin the MOC transformation by rewriting the momentum and continuity equations, Eqs. (3.8) and (3.9) respectively, in terms of L_1 and L_2

$$L_1 = \frac{\partial Q}{\partial t} + gA\frac{\partial H}{\partial x} + \frac{fQ|Q|}{2DA} = 0 \tag{3.13}$$

$$L_2 = \frac{\partial H}{\partial t} + \frac{a^2}{gA}\frac{\partial Q}{\partial x} = 0 \tag{3.14}$$

A linear combination of Eqs. (3.13) and (3.14) using an unknown multiplier λ produces,

$$L = L_1 + \lambda L_2 = \left(\frac{\partial Q}{\partial t} + \lambda a^2 \frac{\partial Q}{\partial x}\right) + \lambda gA\left(\frac{\partial H}{\partial x} + \frac{1}{\lambda}\frac{\partial H}{\partial t}\right) + \frac{fQ|Q|}{2DA} = 0 \tag{3.15}$$

Wylie and Streeter (1993) note that using any two distinct values of λ Eq. (3.15) will again produce two equations equivalent to Eqs. (3.13) and (3.14). If both discharge Q and piezometric head H are functions of distance x and time t, then the total derivative can be written as,

$$\frac{dH}{dt} = \frac{\partial H}{\partial t} + \frac{\partial H}{\partial x}\frac{dx}{dt} \tag{3.16}$$

$$\frac{dQ}{dt} = \frac{\partial Q}{\partial t} + \frac{\partial Q}{\partial x}\frac{dx}{dt} \tag{3.17}$$

By re-examination of Eqs. (3.15), (3.16), and (3.17), it can be seen that if λ is defined as,

$$\frac{dx}{dt} = \frac{1}{\lambda} = \lambda a^2 \tag{3.18}$$

Solving for λ in Eq. (3.18) yields,

$$\lambda = \pm\frac{1}{a} \tag{3.19}$$

By substituting these values of λ into Eq. (3.18), the specific manner in which x and t are related is given as,

$$\frac{dx}{dt} = \pm a \tag{3.20}$$

The substitution of these values of λ into Eq. (3.15) leads to two pairs of equations which Wylie and Streeter (1993) grouped and identified as C^+ and C^- equations.

$$C^+ \begin{cases} \dfrac{dQ}{dt} + \dfrac{gA}{a}\dfrac{dH}{dt} + \dfrac{f}{2DA}Q|Q| = 0 \\ \dfrac{dx}{dt} = +a \end{cases} \tag{3.21}$$

$$C^- \begin{cases} \dfrac{dQ}{dt} - \dfrac{gA}{a}\dfrac{dH}{dt} + \dfrac{f}{2DA}Q|Q| = 0 \\ \dfrac{dx}{dt} = -a \end{cases} \tag{3.22}$$

Thus the two values of λ have been used to convert the original two partial differential equations (Eqs. (3.8) and (3.9)) to two total differential equations (Eqs. (3.21) and (3.22)). The total differential equations (Eqs. (3.21) and (3.22)), however, are not valid everywhere in the x-t plane like Eqs. (3.8) and (3.9) are, and instead are only valid along straight lines with slope +1/a and -1/a in the x-t plane assuming a is constant. A single system of C^+ and C^- equations, called *characteristic lines*, are graphically shown below in Fig. 3.1.

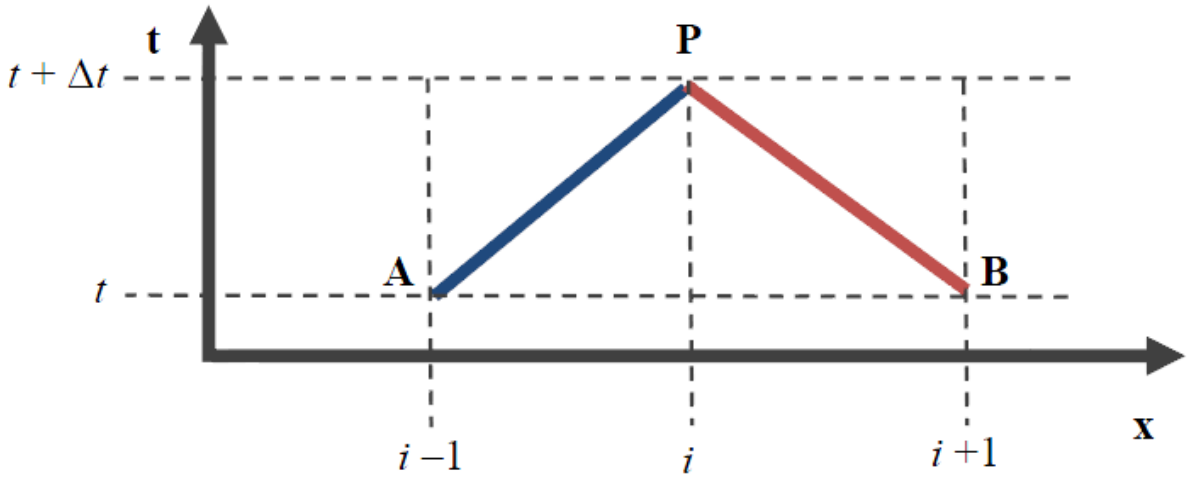

Figure 3.1: C^+ and C^- characteristic lines in the *x-t* plane (From Mondal, 2010)

Thus, with the C^+ and C^- equations and the known values at time t, the two unknowns, head H and discharge Q at time $t + \Delta t$ can be calculated at the intersection of point P in Fig. 3.1 above by integrating the differential equations in finite difference form and solving both equations. These *characteristic lines* extend along the entire *x-t* plane in the system, shown below in Fig. 3.2, and the unknowns can be calculated at all the intersection points.

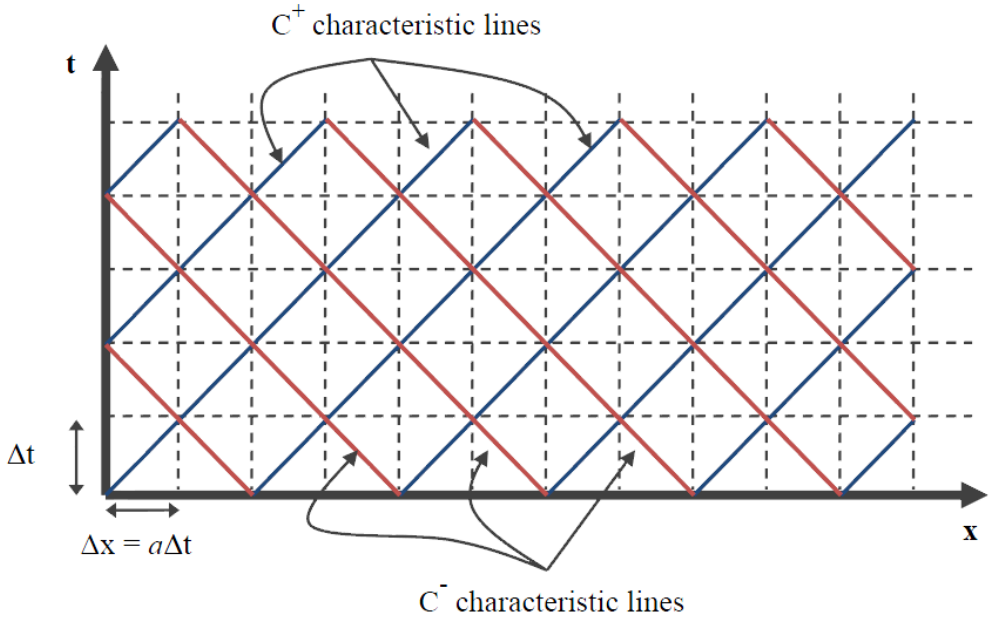

Figure 3.2: Grid of characteristic lines in the *x-t* plane. (From Mondal, 2010)

3.2.1 Finite Difference Equations

Wylie and Streeter (1993) developed a series of finite difference equations to numerically solve the water hammer equations. The wellbore system was divided into *n* equal reaches or subsections, each Δx in length, shown above in Fig. 3.2, and fixed the time-step size as $\Delta t = \Delta x/a$. Since the hydraulic head H and the flow rate Q are known at point A in Fig. 3.1, Eq. (3.21) can be integrated along AP and expressed in terms of the unknown H and Q at point P, shown below in Eq. (3.23). Likewise, since the values of H and Q are known at point B, Eq. (3.22) can be integrated along PB to form a second equation in terms of the same unknown H and Q at point P, shown in Eq. (3.24) below.

$$\int_{H_A}^{H_P} dH + \frac{a}{gA}\int_{Q_A}^{Q_P} dQ + \frac{f}{2gDA^2}\int_{X_A}^{X_P} Q|Q|\,dx = 0 \tag{3.23}$$

$$\int_{H_P}^{H_B} dH + \frac{a}{gA}\int_{Q_P}^{Q_B} dQ + \frac{f}{2gDA^2}\int_{X_P}^{X_B} Q|Q|\,dx = 0 \tag{3.24}$$

The last term in both Eq. (3.23) and (3.24) are unknown a priori, and were replaced with the second-order approximation in Eq. (3.25) and (3.26) respectively.

$$\int_{X_A}^{X_P} Q|Q|\,dx = Q_P\,|Q_A|\left(x_P - x_A\right) \tag{3.25}$$

$$\int_{X_P}^{X_B} Q|Q|\,dx = Q_P\,|Q_B|\left(x_B - x_P\right) \tag{3.26}$$

The integration of Eq. (3.23) and (3.24) with the included second order approximation yield the finite difference equations of Eq. (3.27) and (3.28) for C+ and C- respectively,

$$C^+ : H_P = H_A - B\left(Q_P - Q_A\right) - RQ_P\,|Q_A| \tag{3.27}$$

$$C^- : H_P = H_B + B\left(Q_P - Q_B\right) + RQ_P\,|Q_B| \tag{3.28}$$

where B is pipe characteristic impedance, given by:

$$B = \frac{a}{gA} \tag{3.29}$$

And R is the pipe resistance coefficient, given by:

$$R = \frac{f\,\Delta x}{2gDA^2} \tag{3.30}$$

The friction factor f is calculated with the Chen equation (Chen, 1979) shown below in Eq. (3.31)

$$\frac{1}{\sqrt{f}} = -2\log\left[\frac{1}{3.7065}\left(\frac{e}{D}\right) - \frac{5.0452}{\mathrm{Re}}\left(\log\left[\frac{1}{2.8257}\left(\frac{e}{D}\right)^{1.1098} + \frac{5.8506}{\mathrm{Re}^{0.8981}}\right]\right)\right] \tag{3.31}$$

where D = pipe diameter, e = pipe roughness, and Re = Reynolds number.

The model begins the calculations at time-step $t = 0$, where H and Q are known in each section of the pipe from the initial steady state conditions. The H and Q at any intersection point i at $t = \Delta t$ are calculated from the known values at points i-1 and i+1 from the previous time step, as shown above in Fig. 3.1. Thus, the finite difference equations Eq. (3.23) and (3.24) can be written in terms of time, shown below,

$$C^{+}: H_i^{t+\Delta t} = C_P - B_P Q_i^{t+\Delta t} \tag{3.32}$$

$$C^{-}: H_i^{t+\Delta t} = C_M + B_M Q_i^{t+\Delta t} \tag{3.33}$$

where the subscript i refers to any intersection point, and C_p, B_p, C_m, and B_m are calculated constants from the equations below.

$$C_P = H_{i-1}^{t} + BQ_{i-1}^{t} \tag{3.34}$$

$$B_P = B + R\left|Q_{i-1}^{t}\right| \tag{3.35}$$

$$C_M = H_{i+1}^{t} - BQ_{i+1}^{t} \tag{3.36}$$

$$B_M = B + R\left|Q_{i+1}^{t}\right| \tag{3.37}$$

Finally, solving Eq. (3.32) and (3.33) simultaneously yields,

$$H_i^{t+\Delta t} = \frac{C_P B_M + C_M B_P}{B_P + B_M} \tag{3.38}$$

$$Q_i^{t+\Delta t} = \frac{C_P - C_M}{B_P + B_M} \tag{3.39}$$

The above Eq. (3.38) and (3.39) are only valid within a homogenous pipe section when both a C^+ and C^- equation are present. At the surface and downhole endpoints, or at pipe junctions, only one of the C^+ or C^- equations are present, and boundary conditions are required for the solution.

3.3 BOUNDARY CONDITIONS

As shown in Fig. 3.2 above, the upstream and downstream endpoints have only one characteristic equation present, thus boundary conditions are necessary for solutions at these endpoints. Wylie and Streeter (1993) have defined many boundary conditions in the literature. This analysis only incorporates three boundary conditions which are 1) upstream surface valves, 2) series connections for pipe sections of varying properties (thickness, diameter, Young's Modulus, etc.), and 3) reservoir or hydraulic fracture connection downstream.

3.3.1 Pipe System Nomenclature

The subscript and superscript pipe system nomenclature for wellbores with more than one homologous pipe section must be conveyed before proceeding to boundary conditions. It is common for wellbores to be constructed of pipe sections of varying diameter or thickness, which are taken into account in this model with discrete pipe sections connected in series, with the simplest complex case of two pipe sections shown below in Fig. 3.3.

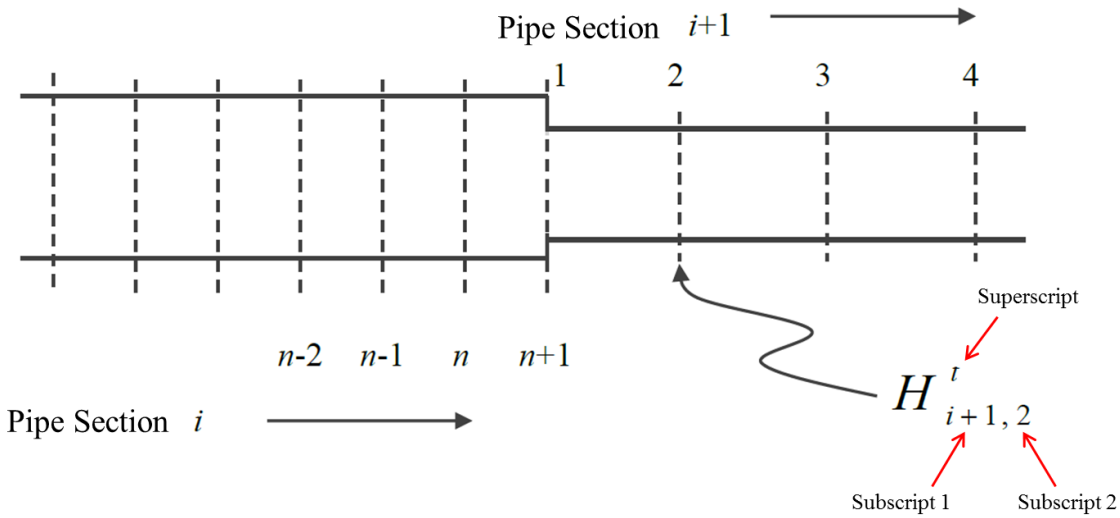

Figure 3.3: Pipe system consisting of two pipes connected in series. (Mondal, 2010)

The notation for such a system includes two subscripts and a superscript. The first subscript refers to the pipe *section* number, while the second subscript refers to the pipe reach or *subsection* number. Finally, the superscript refers to a particular time step.

3.3.2 Upstream Surface Valve

Upon completion of a hydraulic fracture treatment, pumps are often shut down in a stair step pattern to increase the shutdown time to avoid wellbore and or formation damage (Choi and Huang, 2011). This change in flow rate versus time is incorporated into this water hammer solution by mimicking the rate decrease as a valve closure, in which the fractional area of an open valve decreases with time, as shown below in Fig. 3.4.

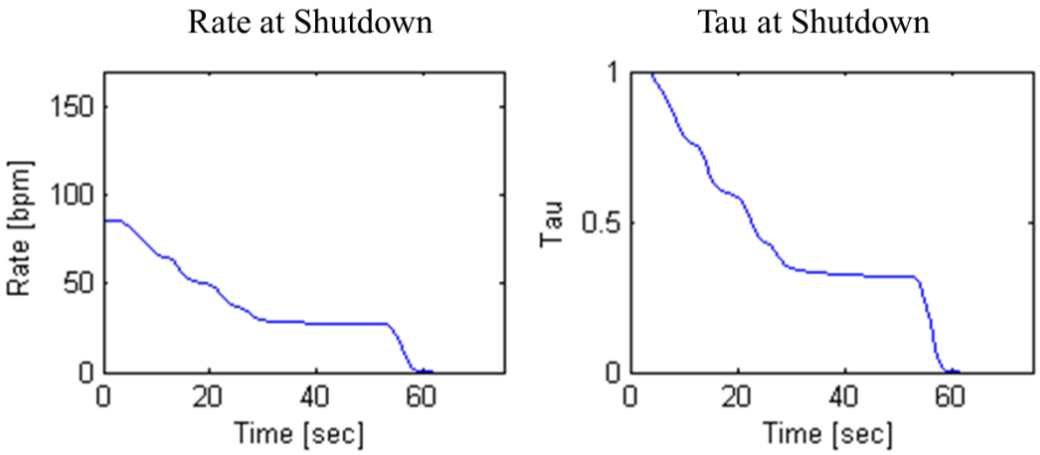

Figure 3.4: Rate versus time and τ versus time at shutdown of a completed hydraulic fracture treatment

This is expressed mathematically by multiplying the steady-state surface discharge Q_o by a specified τ between 0 (for valve completely closed) to 1 (valve completely open), shown below in Eq. (3.40),

$$Q_{1,1}^{t} = Q_o \tau(t) \tag{3.40}$$

where τ varies as a function of time. The C^- characteristic equation from Eq. (3.33) is then used in conjunction with the boundary condition from Eq. (3.40) to solve for H at the upstream endpoint for each time-step.

3.3.3 Pipe Section Series Connection

As previously mentioned in reference to Fig. 3.3, complex wellbores comprised of varying sections of pipe are connected in series, and a boundary condition must be introduced to solve the characteristic equations for H and Q at the exit of pipe section i and the entrance of pipe section i +1, shown below in Fig. 3.5.

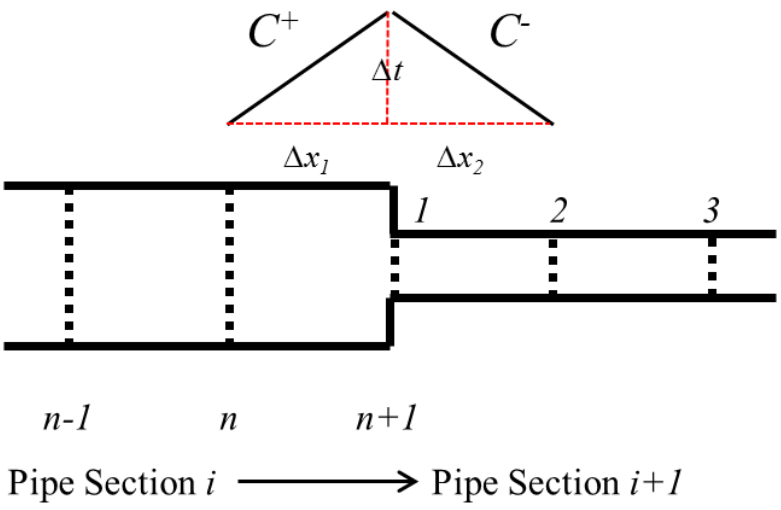

Figure 3.5: C^+ and C^- characteristic equations for a pipe series connection between pipe section i and $i+1$

The boundary condition is derived from the continuity equation, shown below in Eq. (3.41), and the assumption that the head losses at the pipe junction are neglected, shown below in Eq. (3.42).

$$Q_{i,n+1} = Q_{i+1,1} \tag{3.41}$$

$$H_{i,n+1} = H_{i+1,1} \tag{3.42}$$

The C^+ and C^- characteristic equations of Eq. (3.32) to (3.37) are rewritten in terms of pipe section i and i+1 respectively from Fig. 3.5, shown below,

$$H_{i,n+1}^{t+\Delta t} = C_{P,i} - B_{P,i} Q_{i,n+1}^{t+\Delta t} \tag{3.43}$$

$$C_{P,i} = H_{i,n}^{t} + B_i Q_{i,n}^{t} \tag{3.44}$$

$$B_{P,i} = B_i + R_i \left| Q_{i,n}^{t} \right| \tag{3.45}$$

$$H_{i+1,1}^{t+\Delta t} = C_{M,i+1} + B_{M,i+1} Q_{i+1,1}^{t+\Delta t} \tag{3.46}$$

$$C_{M,i+1} = H^t_{i+1,2} - B_{i+1} Q^t_{i+1,2} \tag{3.47}$$

$$B_{M,i+1} = B_{i+1} + R_{i+1} \left| Q^t_{i+1,2} \right| \tag{3.48}$$

Finally, solving Eq. (3.43) and (3.46) simultaneously for discharge Q yields:

$$Q^{t+\Delta t}_{i,n+1} = Q^{t+\Delta t}_{i+1,1} = \frac{C_{P,i} - C_{M,i+1}}{B_{P,i} + B_{M,i+1}} \tag{3.49}$$

Once the discharge Q is calculated from Eq. (3.49), the other unknowns are calculated directly from the respective equations above.

3.3.4 Downstream Fracture Boundary Condition

The downhole fracture boundary condition defined by Mondal (2010) was used for this analysis, which consists of a lumped resistance R, capacitance C and inertance I equivalent to an electrical circuit. The general form of the downhole boundary condition is shown below in Eq. (3.50), in which the change in hydraulic potential (ΔH) for a certain discharge (Q) is a function of R, C, and I.

$$\frac{\Delta H}{Q} = f\left(R, C, I\right) \tag{3.50}$$

Mondal (2010) claims such a boundary condition is advantageous for three reasons: 1) it accounts for the resistance to flow, fracture compliance, and the compressibility and inertial effects of the fracturing fluid, 2) the boundary condition is dynamic, and 3) easily coupled with the wellbore water hammer equations. Thus, for any fracture numerically defined by R, C, and I the pressure and discharge transients can be calculated at any point in the well between the surface and the fracture mouth.

Each of the R, C, and I terms is defined with respect to the discharge Q or the hydraulic potential P, with the latter shown below in Eq. (3.51),

$$P = \rho g H = \rho g z + p + \frac{1}{2}\rho v^2 \tag{3.51}$$

where ρ = density, g = acceleration due to gravity, H = total hydraulic head, z = elevation above reference datum, and v = fluid velocity. The resistance R is defined as the proportionality constant between the discharge Q into or out of the fracture and the potential difference required to sustain that discharge, shown in Eq. (3.52) (Schönfeld, 1951).

$$\Delta P = RQ \tag{3.52}$$

Holzhausen et al. (1985) defined capacitance C as the ratio of fracture volume change per change in hydraulic potential, shown below in Eq. (3.53). Fracture capacitance is equivalent to fracture compliance.

$$C = \frac{\Delta V}{\Delta P} \tag{3.53}$$

Capacitance can also be written in terms of discharge Q, shown below in Eq. (3.54).

$$Q = C\frac{dP}{dt} \tag{3.54}$$

The inertance I is related to the fluid mass in the system, and is proportional to the potential difference required to accelerate or decelerate the discharge Q in the absence of

friction, shown below in Eq. (3.55) (Schönfeld, 1951). Inertance I is equivalent to the inductance in electrical circuits (Feynman et al., 1964).

$$\Delta P = I \frac{dQ}{dt} \tag{3.55}$$

A summary of R, C, and I with the equivalent fracture model terms is shown below in Table 3.1.

Symbol	**Electric**	**Hydraulic Fracture Model**
R	Resistance	Resistance (near wellbore friction)
C	Capacitance	Capacitance (fracture compliance)
I	Inductance	Inertance
P	Potential Difference	Potential Difference (pressure)
Q	Current	Discharge/Flow rate

Table 3.1: Summary of hydraulic fracture boundary condition terms and electrical circuit equivalents

The R, C, and I are combined in series, analogous to an electrical circuit to satisfy the downhole boundary condition. Mondal (2010) showed a series combination was sufficient to describe a hydraulic fracture because the fluid and volume of the fracture dominate the pressure/flow behavior due to minimal leakoff and a linear flow regime in the fracture for the water hammer duration. Figure 3.6 below depicts a hydraulic fracture connected to a horizontal wellbore along with the electrical circuit representation.

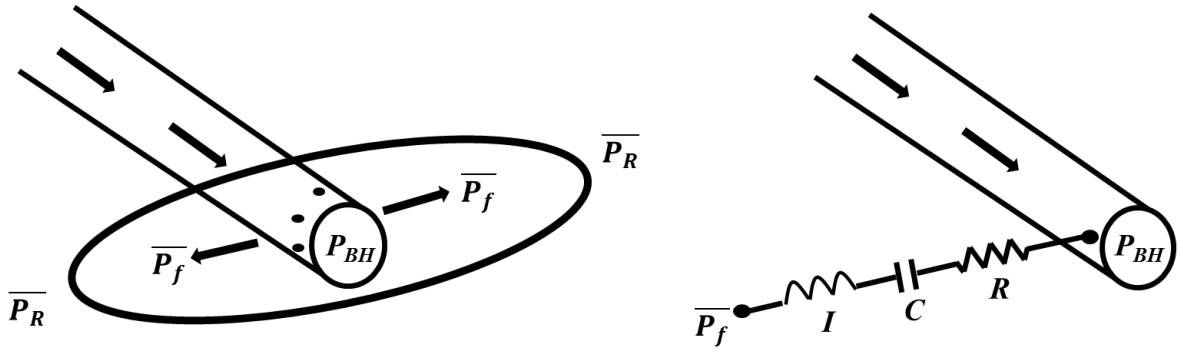

(a) Horizontal Wellbore with Fracture (b) Electrical Circuit Representation

Figure 3.6: Schematics for (a) horizontal wellbore with fracture and (b) the electrical circuit representation

In the series electrical circuit representation, current will flow into the circuit until the capacitor becomes fully charged, at which point current can only flow into the circuit if the potential difference is increased or the impedance is decreased. Thus, current can flow into the circuit at a constant potential difference only when the capacitance is increased. This is analogous to a hydraulic fracture, as fluid flows into the fracture until the maximum compliance is reached, and additional fluid can only flow into the fracture if the net pressure is increased. The potential difference at the downhole boundary condition, defined as the difference between bottomhole pressure (P_{BH}) and average near wellbore pressure (P_f), is thus the sum of the individual R, C, and I potential differences, shown below in Eq. (3.56).

$$\rho g \Delta H = RQ + \frac{1}{C}\int Q dt + I\frac{dQ}{dt} \tag{3.56}$$

R, C, and I can then be altered iteratively to match the pressure response from field data.

3.4 EQUATIONS FOR FRACTURE PARAMETER ESTIMATION

The goal of this work was not only to classify a given hydraulic fracture by an *R*, *C*, and *I*, but to also determine certain parameters such as fracture half-length, height, and width. Relationships between *R*, *C*, and *I* and fracture properties were derived from the work of Shylapobersky et al. (1988). The following is a description of the assumptions and calculations for determining fracture parameters from *R*, *C*, and *I*.

3.4.1 Assumptions for Fracture Dimension Calculations

The following assumptions were made to simplify the fracture dimension calculations:

i. Only a single planar fracture of constant height and ellipsoidal cross-section is created.
ii. Fracture length is constant for the duration of water hammer, and fracture compliance is only due to a change in width.
iii. Negligible fracture leakoff occurs for the duration of the water hammer.
iv. Flow resistance is dominated by near wellbore friction and negligible along the length of the fracture.
v. Average near wellbore pressure (P_f) is estimated from surface pressure data.

These assumptions are consistent with most hydraulic fracture treatments attempted in unconventional reservoirs, as low reservoir permeability results in small leakoff values, and there is minimal height and length growth after pump shutdown. Furthermore, since the fracture remains open for the duration of the water hammer event, the resistance along the fracture length is minimal, and the near wellbore friction is the only contributor to the resistance *R*. Fracture connectivity with the wellbore can therefore be quantified by the magnitude of the *R* term, shown below in Eq. (3.57), with large

resistance values signifying increased tortuosity and high near wellbore frictional pressure drop *(*ΔP_{nwf}).

$$R = \frac{\Delta P_{nwf}}{Q_0} \tag{3.57}$$

where Q_0 = injection rate prior to pump shutdown.

As previously mentioned, the hydraulic potential difference, ΔH, in Eq. (3.50) and (3.56) is defined as the difference between the bottomhole pressure and the average near wellbore pressure, as shown in Eq. (3.58) below.

$$\rho g \Delta H = P_{BH} - \overline{P}_f \tag{3.58}$$

The industry standard is to use the instantaneous shut in pressure (P_{ISIP}) as the average near wellbore pressure, however, this selection assumes the near wellbore frictional pressure drop (P_{BH}-P_{ISIP}) equals zero at pump shut down, which is not the case when a water hammer occurs. The P_{ISIP} is thus not an accurate representation of the average near wellbore pressure due to the presence of frictional pressure. P_f is thus determined by the method mentioned by Mondal (2010), which encompasses fitting the surface pressure data at shut down with the exponential function in Eq. (3.59).

$$\overline{P}_f = P_{f0} e^{-kt} \tag{3.59}$$

where P_{f0} is the average near wellbore pressure prior to shut down, and k is the exponential decay constant, shown graphically in Fig. 3.7 below. P_{f0} will always be between PISIP and the end of water hammer pressure (P_{EoWH}), but P_{EoWH} is a good estimate for P_{f0} at low pressure decay rates.

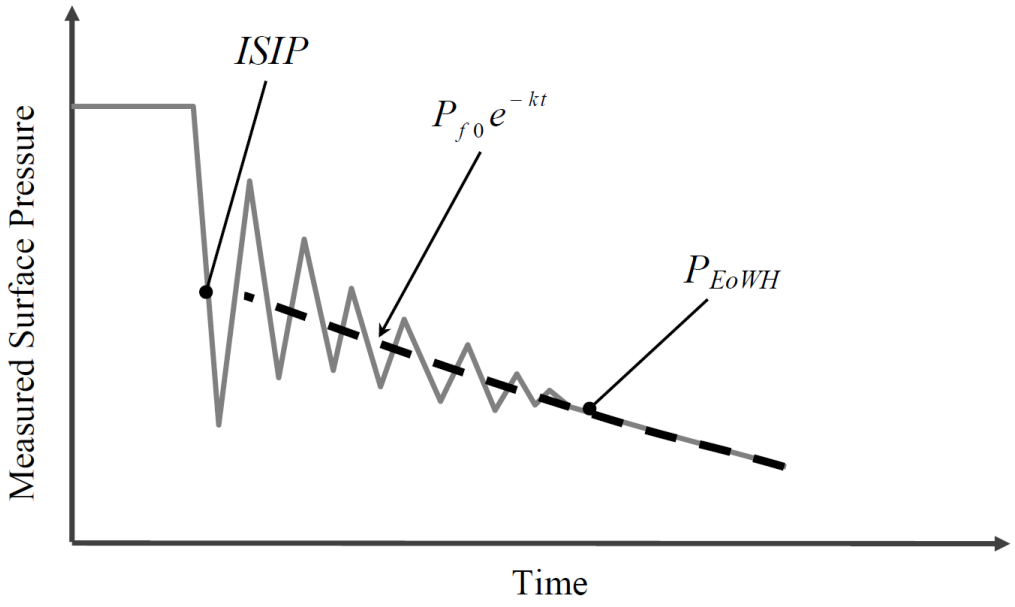

Figure 3.7: Graphical representation of determining P_f from fitting the surface pressure data with an exponential function (From Mondal, 2010).

3.4.2 Calculating *R*, *C*, and *I* from Fracture Dimensions

The fracture length, width, height, and net pressure can be calculated once the appropriate *R*, *C*, and *I* values have been determined. The average net pressure ($\overline{\Delta P}_o$) is simply the difference between the average pressure inside the fracture (P_{BH}-P_{nwf}) and the minimum horizontal in-situ stress (S_{Hmin}), in which P_{nwf} is calculated from *R* and Q_0 in Eq. (3.57) above.

$$\overline{\Delta P}_o = \left(P_{BH} - \Delta P_{nwf}\right) - S_{H\min} \tag{3.60}$$

Fracture length, width, and height are determined from the capacitance and inertance based on the work of Shylapobersky et al. (1988), which classified fractures as short $(2L_f / h_f < 1)$ or long $(2L_f / h_f \geq 1)$. Shylapobersky et al. (1988) related net pressure to fracture dimensions with Eq. (3.61) below,

$$\overline{\Delta P_o} = \frac{4}{\pi^2}\frac{E}{1-\nu^2}E(m)\bar{w}\begin{pmatrix}1/L_f\\2/h_f\end{pmatrix} \tag{3.61}$$

where ν = Poisson's ratio, w = average fracture width, E = Young's modulus, and $E(m)$ = the complete elliptical integral of the second kind, shown in Appendix A, where m is defined in Eq. (3.62) below.

$$m = \begin{pmatrix}1-(2L_f/h_f)^2 \geq 0\\1-(2h_f/L_f)^2 \geq 0\end{pmatrix} \tag{3.62}$$

For Eq. (3.61), (3.62), and the following equations, the upper parameters in the brackets are for short fractures and the lower parameters are for long fractures.

Based on the assumption that the change in fracture volume due to fracture compliance is only due to a change in width, capacitance is rewritten in terms of the fracture dimensions, shown below in Eq. (3.63).

$$C = \frac{\Delta V}{\Delta P} = \frac{\Delta w h_f L_f}{\Delta P} \tag{3.63}$$

The net pressure in Eq. (3.61) can be substituted into the ΔP term of Eq. (3.63), which yields the following equation for capacitance:

$$C = \frac{\pi^2 h_f L_f}{4E'E(m)}\begin{pmatrix}L_f\\h_f/2\end{pmatrix} \tag{3.64}$$

Where E' is the plane strain elastic modulus, defined in Eq. (3.64) below.

$$E' = \frac{E}{1-\nu^2} \tag{3.65}$$

Fracture inertance is determined by relating fracture dimensions to the definition of inertance in Eq. (3.55) above, and is shown below in Eq. (3.66).

$$I = \frac{\rho L_f}{\overline{w} h_f} = \frac{4\rho E' E(m) L_f}{\overline{\Delta P}_o h_f} \begin{pmatrix} 1/L_f \\ 2/h_f \end{pmatrix} \tag{3.66}$$

Fracture half-length for both short and long fractures is obtained by substituting Eq. (3.66) into Eq. (3.64), shown below in Eq. (3.67).

$$L_f = \sqrt{\frac{CI\overline{\Delta P_o}}{\rho}} \tag{3.67}$$

An expression for fracture height is obtained by rearranging Eq. (3.64) as,

$$h_f = \begin{cases} \dfrac{4E' E(m) C}{\pi^2 L_f^2} & short \\ \sqrt{\dfrac{4E' E(m) C}{\pi^2 L_f}} & long \end{cases} \tag{3.68}$$

Both $\overline{w}$ and *E(m)* in Eq. (3.68) are functions of fracture height, thus h_f and $\overline{w}$ must be calculated iteratively such that Eq. (3.68) above and Eq. (3.69) below are satisfied.

$$h_f = \frac{\rho L_f}{\overline{w} I} \tag{3.69}$$

3.4.3 Length and Width Estimation from Known Fracture Height

If the fracture height is assumed to be the perforated interval height, and *R*, *C*, and *I* are known, fracture length and width can be calculated from an expression formulated

by Shylapobersky et al. (1988) that takes width due to viscous dissipation (w_f) and rock toughness effects (w_c) into consideration, shown below in Eq. (3.70):

$$w' = \sqrt{w_c^2 + \sqrt{w_c^4 + w_f^4}} \tag{3.70}$$

where *w'* is average width, not to be confused with $\overline{w}$ in Eq. (3.69), and w_c and w_f are shown below in Eqs. (3.71) and (3.72) respectively.

$$w_c^2 = \frac{\pi^2 \Gamma}{4E'E(m)} \begin{pmatrix} L_f / G_s(m) \\ h_f / (2G_l(m)) \end{pmatrix} \tag{3.71}$$

$$w_f^4 = \frac{3\pi^4 \mu Q_0 L_f}{8E'E(m)} \begin{pmatrix} L_f / h_f \\ 1/2 \end{pmatrix} \tag{3.72}$$

$G_s(m)$ and $G_l(m)$ in Eq. (3.71) are the geometrical functions for short and fractures respectively, shown below in Eq. (3.73).

$$\begin{pmatrix} G_s(m) \\ G_l(m) \end{pmatrix} = \begin{pmatrix} 1.0 - (2L_f / h_f)^2 \left[K(m) - E(m)\right] / \left[2mE(m)\right] \\ 0.5 - (h_f / 2L_f)^2 \left[K(m) - E(m)\right] / \left[2mE(m)\right] \end{pmatrix} \tag{3.73}$$

Where $K(m)$ is the complete elliptical integral of the first kind, defined in Appendix A.

Γ_s and Γ_l in Eq. (3.71) above are the apparent fracture toughness for short and long fractures respectively, shown below in Eq. (3.74).

$$\begin{pmatrix} \Gamma_s \\ \Gamma_l \end{pmatrix} = \begin{pmatrix} \dfrac{2\overline{\Delta P}_o^2 L_f}{\pi E'} \\ \dfrac{\pi^2 \overline{\Delta P}_o^2 h_f G_l(m)}{32E'E(m)} \end{pmatrix} \tag{3.74}$$

The two average widths in Eqs. (3.70) and (3.61) are equated, and fracture length is calculated iteratively.

3.4.4 Equivalent Fracture Dimensions

It is important to emphasize that the fracture dimensions obtained from the derivations of Mondal (2010) and Shylapobersky et al. (1988) are based on the assumptions that planar, bi-wing fractures are created. Present day hydraulic fracture treatments consist of multiple perforation clusters per stage, with the goal of creating multiple fractures in each stage. This created fracture network is in communication with the wellbore right after the pump shutdown, and influences the water hammer signal. Thus, the calculated fracture dimensions should be considered to be equivalent fracture dimensions, where the effect of multiple fractures is summarized as a single, bi-wing fracture.

Furthermore, the calculated equivalent fracture length and width are a combination of all the created fractures in communication with the wellbore. Consider a stimulation treatment stage that consists of three perforation clusters that create three transverse fractures, shown in Fig. 3.8 below. This can be modeled by a *RCI* circuit, where the capacitance of each fracture is connected in parallel (Feynman et al., 1964), shown in Fig. 3.9 below. Since capacitances in parallel are combined as follows,

$$C_T = C_1 + C_2 + C_3 \tag{3.75}$$

where C_T = total capacitance, Eq. (3.67) for fracture half-length can be re-written as,

$$L_{f_E} = \sqrt{\frac{C_T I_T \overline{\Delta P_o}}{\rho}} = \sqrt{\frac{C_1 I_T \overline{\Delta P_{o1}}}{\rho} + \frac{C_2 I_T \overline{\Delta P_{o_2}}}{\rho} + \frac{C_3 I_T \overline{\Delta P_{o_3}}}{\rho}} \tag{3.76}$$

Where L_{f_E} = equivalent half-length, and summarized for *n* number of fractures as,

$$L_{f_E} = \sqrt{\frac{I_T}{\rho} \sum_{i=1}^{n} C_i \overline{\Delta P_{o_i}}} \tag{3.77}$$

Equivalent fracture half-length can be re-written as the summation of the individual fracture half-lengths as follows,

$$\begin{aligned} L_{f_E} &= \sqrt{L_{f_1}^2 + L_{f_2}^2 + L_{f_3}^2} \\ L_{f_E} &= \sqrt{\sum_{i=1}^{n} L_{f_i}^2} \end{aligned} \tag{3.78}$$

The substitution of Eq. (3.76) into Eq. (3.69) and subsequent rearrangement yields an expression for equivalent average fracture width, shown below in Eq. (3.79),

$$\overline{w_E} = \frac{\sqrt{\rho}}{h_f \sqrt{I_T}} \sqrt{C_1 \overline{\Delta P_{o_1}} + C_2 \overline{\Delta P_{o_2}} + C_3 \overline{\Delta P_{o_3}}} \tag{3.79}$$

and summarized for *n* number of fractures as,

$$\overline{w_E} = \frac{\sqrt{\rho}}{h_f \sqrt{I_T}} \sqrt{\sum_{i=1}^{n} C_i \overline{\Delta P_{o_i}}} \tag{3.80}$$

Equivalent average fracture width can be written in terms of the average fracture widths as follows,

$$\begin{aligned} \overline{w_E} &= \sqrt{\overline{w_1^2} + \overline{w_2^2} + \overline{w_3^2}} \\ \overline{w_E} &= \sqrt{\sum_{i=1}^{n} \overline{w_i^2}} \end{aligned} \tag{3.81}$$

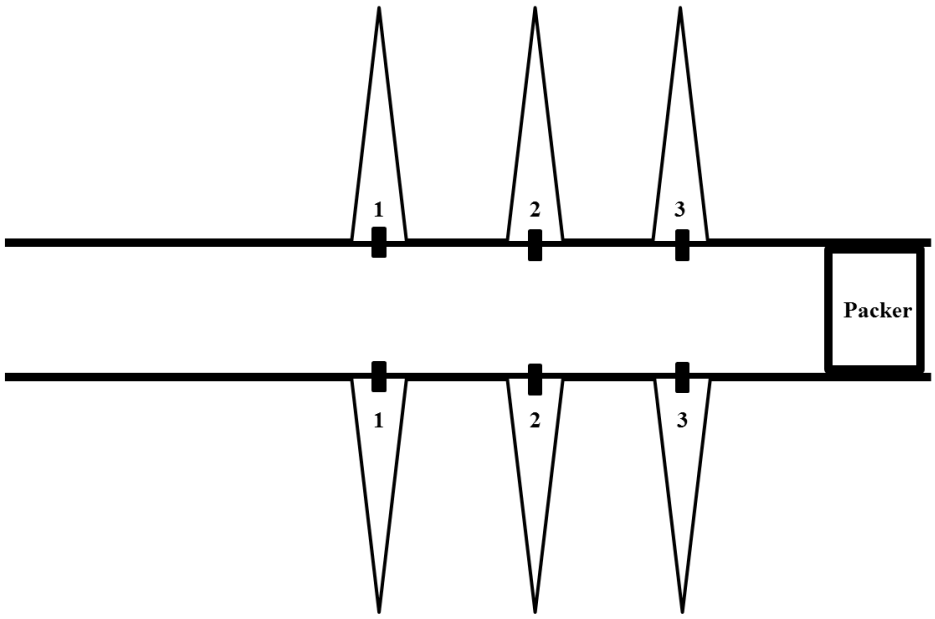

Figure 3.8: Map view schematic of a stimulation stage in a horizontal well with three perforation clusters and three created hydraulic fractures.

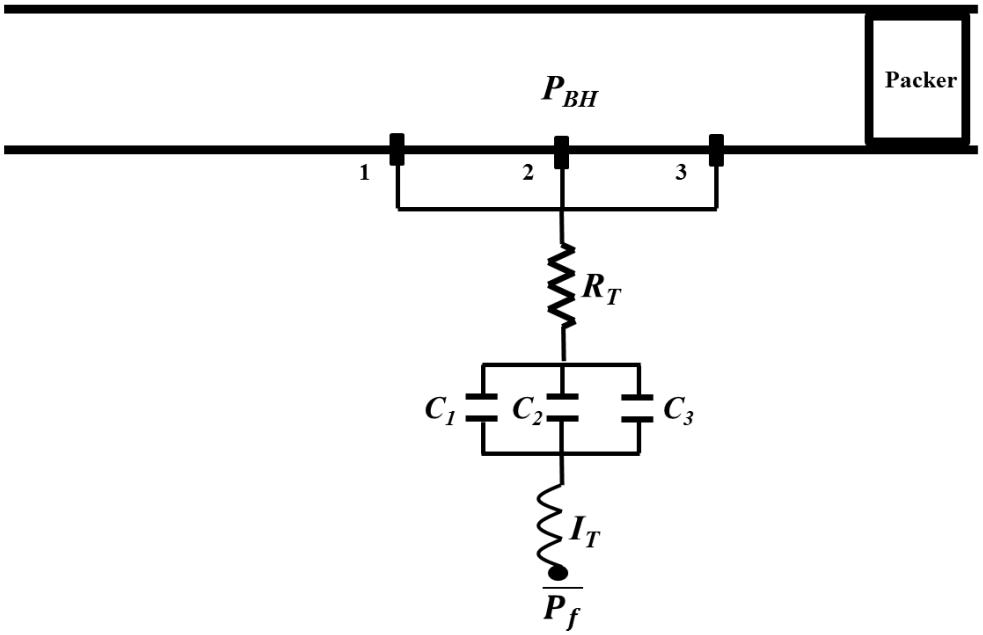

Figure 3.9: Map view of Fig. 3.8 modeled as a *RCI* circuit with the three fracture capacitances connected in parallel.

3.5 MODEL VALIDATION

The numerical model was validated with field data from Mondal (2010) and Ferrick et al. (1982).

3.5.1 Mondal (2010) Field Data

The Mondal (2010) field data of a post-minifrac water hammer was history matched by iteratively altering the *R*, *C*, and *I* values until an appropriate match was obtained, shown below in Fig. 3.10, with the final *R*, *C*, and *I* values of 52.9 bpd/psi, 4.33×10^{-2} bbl/psi, and 2.45×10^{-10} psi/bbl/d^2 respectively.

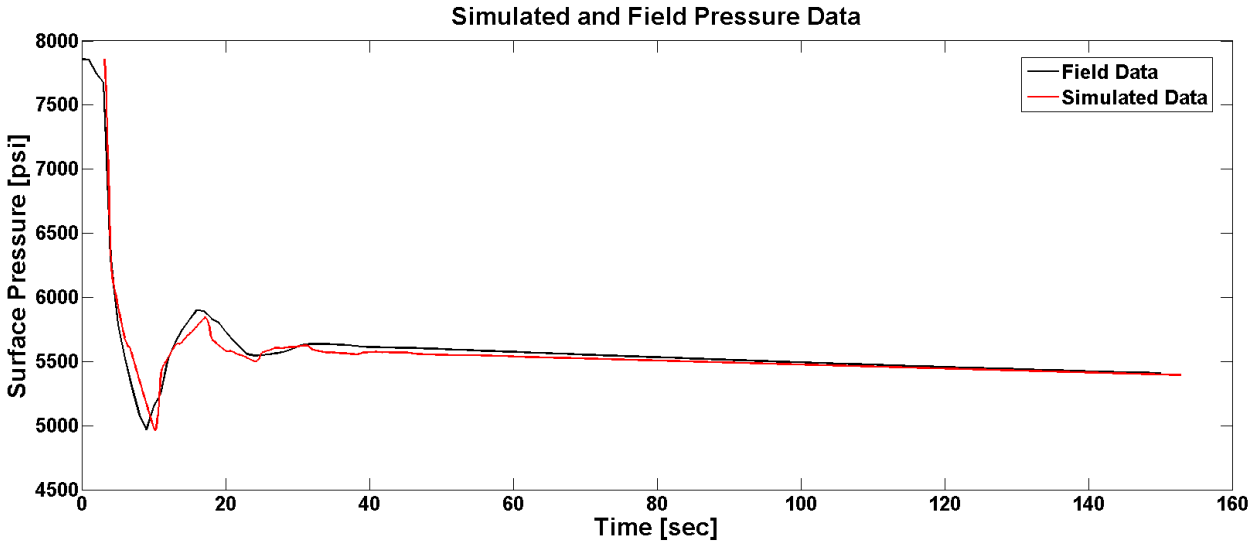

Figure 3.10: History match of Mondal (2010) field data with numerical model data where R = 52.9 bpd/psi, C = 4.33×10^{-2} bbl/psi, and I = 2.45×10^{-10} psi/bbl/d^2.

The numerical model matched the field data (surface pressure in the well), and the calculated fracture dimensions, along with those determined by Mondal (2010) are shown below in Table 3.2. The fracture dimensions obtained from the numerical model are in reasonable agreement with both Mondal's model and the fracture simulator "E-Stimplan".

Fracture Dimensions	Calculated by Mondal (2010)	Calculated by E-Stimplan (Mondal 2010)	Numerical Model
Height [ft]	81.7	75	71.6
Half-Length [ft]	69.3	35	31.2
Width [in]	0.13	0.22	0.28

Table 3.2: Fracture dimensions comparison between Mondal (2010) values and current numerical model

3.5.2 How *RCI* Variations Affect Pressure Profile

R, *C*, and *I* were individually varied over large ranges with each other variable held constant to quantify the effect on the water hammer oscillations for the Mondal (2010) data.

3.5.2.1 Variations in Resistance

As resistance increased the initial water hammer amplitude decreased due to more energy expended at the perforations and the near-wellbore region, shown below in Fig. 3.11. Increased resistance also corresponded to an increased decay of the pressure oscillations, shown in Fig. B.1 in Appendix B for several resistances.

3.5.2.2 Variations of Capacitance

Variations in capacitance altered the period of water hammer oscillations and the average pressure sustained by the water hammer, shown for several various capacitance values in Fig. B.2 in Appendix B. The water hammer period was 4L/a for high capacitance values, and reduced to 2L/a as the capacitance was decreased, as shown in Fig. 3.12 below.

Variations in capacitance also affected the average pressure amplitude during the water hammer event, such that as capacitance was decreased the average pressure decreased, shown below in Fig. 3.13.

3.5.2.3 Variations of Inertance

As inertance was increased, the water hammer period increased as shown below in Fig. 3.14. The water hammer period increased very quickly once the inertance passed a threshold of $3x10^{-8}$ psi/bbl/d^2.

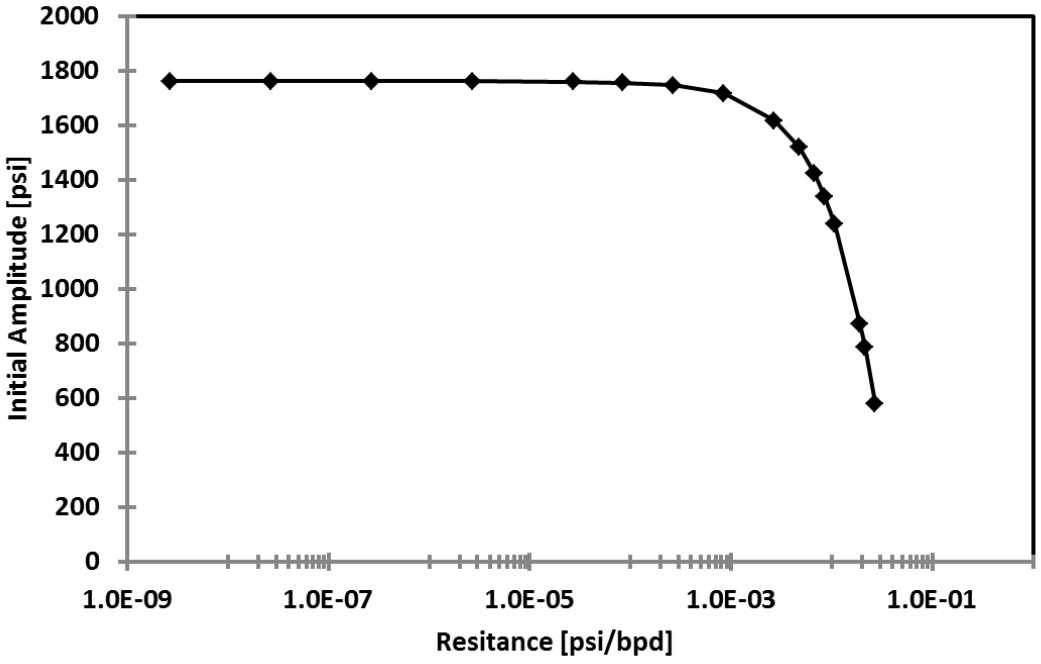

Figure 3.11: Summary of the effect of resistance on the initial water hammer amplitude

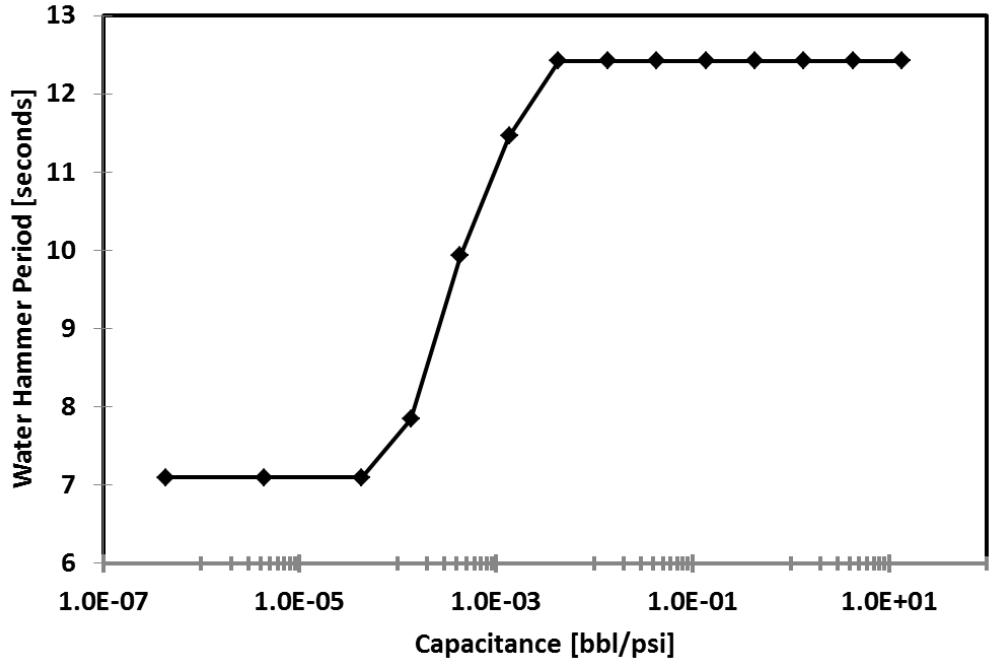

Figure 3.12: Summary of the effect of capacitance on the water hammer period

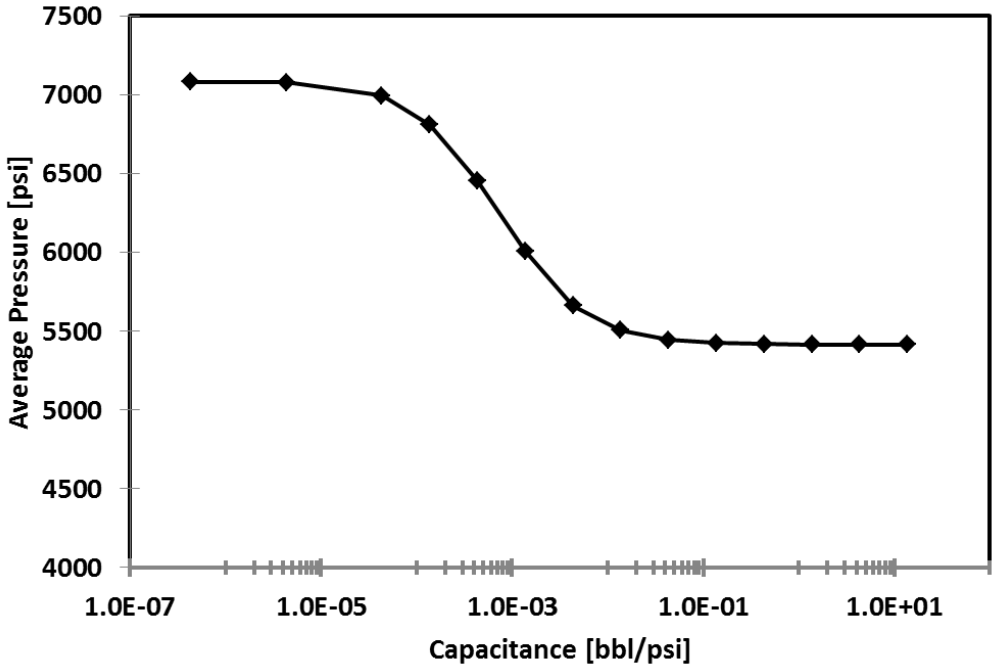

Figure 3.13: Summary of the effect of capacitance on the pressure sustained during a water hammer event.

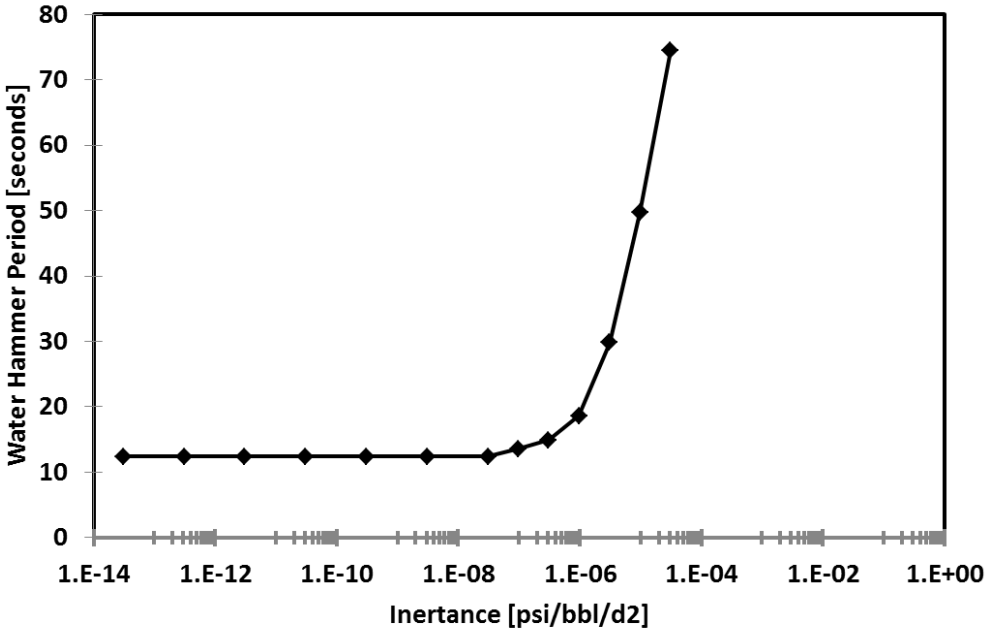

Figure 3.14: Summary of the effect of inertance on the water hammer period.

3.5.2.4 RCI Iteration Method

A systematic method was used to iteratively history match field data consistently since the *R*, *C*, and *I* affect similar water hammer attributes. First, the resistance was iteratively changed until the numerical model matched the amplitudes and decay of the field data. Capacitance was then altered until the numerical model matched the period and average pressure of the field data. Lastly, the inertance was iteratively changed until the calculated hydraulic fracture height was equal to the perforation interval for a vertical well, or the formation thickness for a horizontal well.

3.5.3 Ferrick et al. (1982) Field Data

Ferrick et al. (1982) recorded surface pressure for a water hammer event created by rapidly opening and closing a wellhead valve for both before and after a hydraulic

fracture treatment, shown previously in Fig. 2.18. The post-frac surface pressure data was history matched until an appropriate match was obtained, shown below in Fig. 3.15.

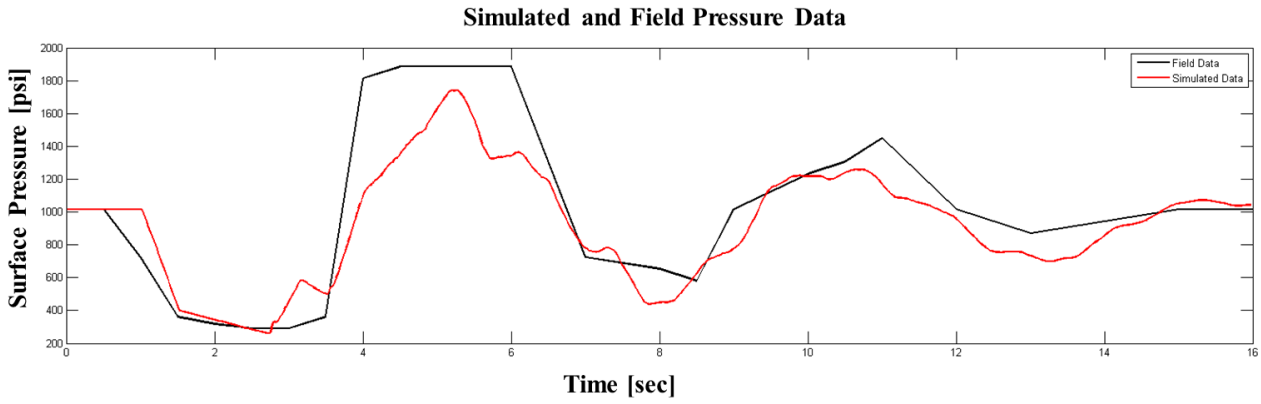

Figure 3.15: History match of Ferrick et al. (1982) post-frac data with numerical model.

The modeled surface pressure was in good agreement with the field data in terms of both the period and amplitude. The small bumps in the modeled data were caused by wave reflections within the casing due to diameter changes, and are not exhibited in the field data because the sampling rate was too low. The wellbore diagram in Fig. 3.16 below shows the diameter change from 6.2 cm inner diameter tubing to 16 cm casing at 1296 m depth (Ferrick et al., 1982). The large variance in conduit diameters results in a significant impedance difference which induces reflections (Wylie and Streeter, 1978; Paige et at., 1992).

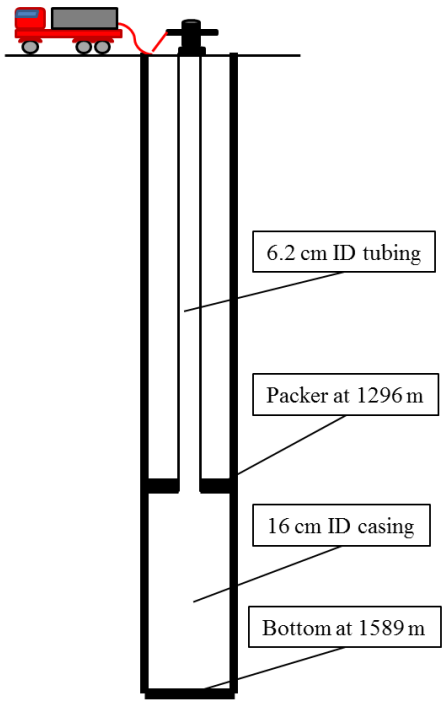

Figure 3.16: Diagram of Ferrick et al. (1982) well with large difference in tubing and casing inner diameters (not to scale).

To further validate the numerical model in terms of how changes in *R*, *C*, and *I* alter the modeled pressure response, capacitance was increased for the Ferrick et al. (1982) well from a small to large value over the course of multiple simulations. The resulting normalized frequency of oscillations (inverse of period) was plotted versus the capacitance in m^2 to match the work done by Holzhausen et al. (1985) on the Ferrick et al. (1982) data, shown below in Fig. 3.17.

As Fig. 3.17 shows, the *RCI* numerical model is in good agreement with the Holzhausen et al. (1985) work. In both (a) and (b) of Fig. 3.17 the normalized frequency ranges from 1 to 2 Hz, which corresponds to the periods of 4L/a and 2L/a respectively. Thus, hydraulic fractures with any significant capacitance will alter the pressure oscillations of a water hammer event.

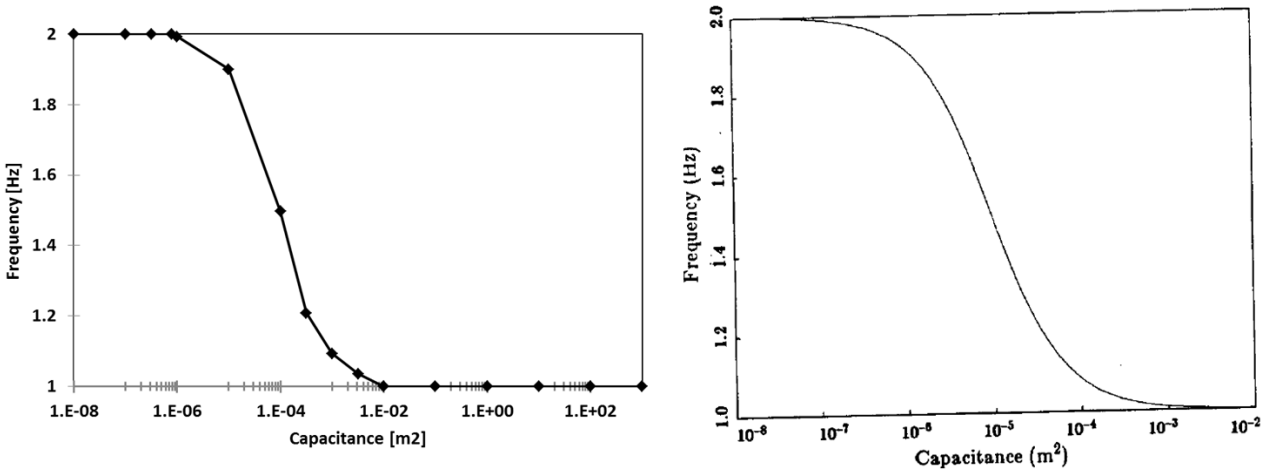

(a) *RCI* numerical model

(b) Holzhausen et al. (1985) *RC* model

Figure 3.17: Capacitance versus normalized frequency from Ferrick et al. (1982) data for (a) *RCI* numerical model and (b) Holzhausen et al. (1985) *RC* impedance model.

3.6 MODEL FORMULATION SUMMARY

The RCI numerical model sufficiently simulates a water hammer event for any specific conditions by solving the continuity and momentum equations within a wellbore linked to a series circuit with the Method of Characteristics. Hydraulic fractures can be characterized by a specific *R*, *C*, and *I* by iteratively history matching stimulation water hammer field data. Fracture dimensions can be calculated for known *R*, *C*, and *I* values based on the derivation of Mondal (2010) and Shylapobersky et al. (1988). Finally, simulation results are in good agreement with results presented earlier by Mondal (2010), Holzhausen et al. (1985), and Ferrick et al. (1982).

Chapter 4: Results and Discussion

The *RCI* model was used to history match field-data from three multi-stage, hydraulically fractured horizontal wells. *R*, *C*, and *I* values were determined for each stage, from which the fracture dimensions were calculated, and the results were compared to production log and SRV data. Bottom-hole pressure transients were modeled, which led to accurate instantaneous shut-in pressure estimations. Several water hammer events in the same fracture treatment were analyzed, and fracture growth was observed. Fracture complexity was also quantified and compared to *RCI* values. Finally, a Fast Fourier Transform was performed on water hammer data to identify dominant frequencies.

4.1 History Matching Field Data

The *R*, *C*, and *I* values of 51 stages were obtained by iteratively history matching field data until an appropriate fit was acquired. The surface pressure match for the first water hammer event in stage 1 of Well A is shown below in Fig. 4.1.

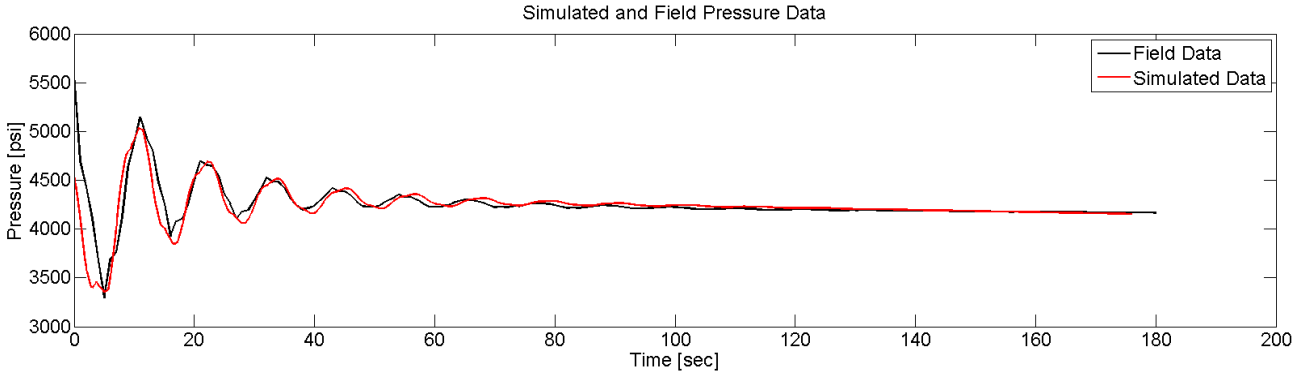

Figure 4.1: History match of field data with simulation results for shutdown event 1 in stage 1 of Well A

The simulated data for Well A stage 1 matches the field data sufficiently in terms of period, amplitude, and decay. Fracture height, half-length, and width were calculated

as 100 feet, 602 feet, and 1.78 inches respectively. The history match pressure profiles for the remaining stages of wells A, B, and C, as well as the *R*, *C*, and *I* values obtained from the fit with data are shown in tabular form in Appendix C and D respectively.

4.2 *RCI* RELATIONSHIPS WITH PRODUCTION AND SRV

To test our hypothesis that the pressure transients in the water hammer response have information about the fracture geometry, we plotted the inferred resistance, capacitance, and inertance derived from the signal against other indirect measures of fracture geometry. Capacitance had a direct relationship with the stimulated reservoir volume (SRV) derived from micro-seismic measurements, as shown below in Fig. 4.2. The resistance had an inverse relationship with SRV, as shown below in Fig. 4.3. The inertance showed a general trend with SRV, but the relationship was not very good as shown below in Fig. 4.4.

Production log data was compared to *R*, *C*, and *I* values in Fig. 4.5, 4.6, and 4.7 respectively. No significant correlations were observed. It is also important to note that there was no significant correlation between micro-seismic derived SRV and gas production data either, as shown in Fig 4.8. This is not surprising since the production rate is a function of many different parameters other than the fracture geometry.

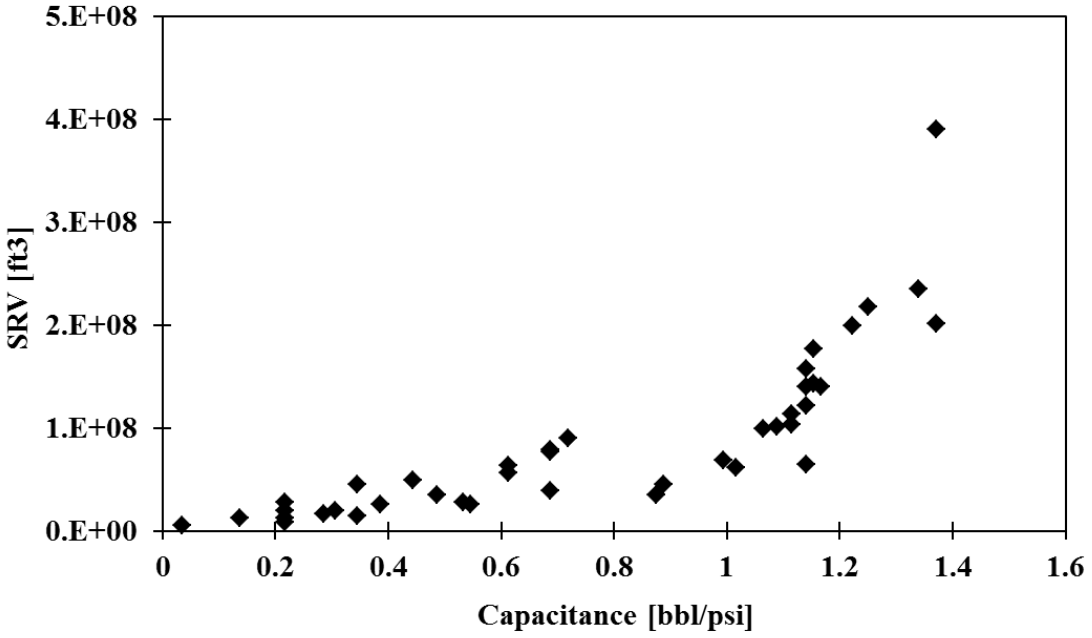

Figure 4.2: Capacitance obtained from our model's interpretation of water hammer data plotted versus stimulated reservoir volume (SRV).

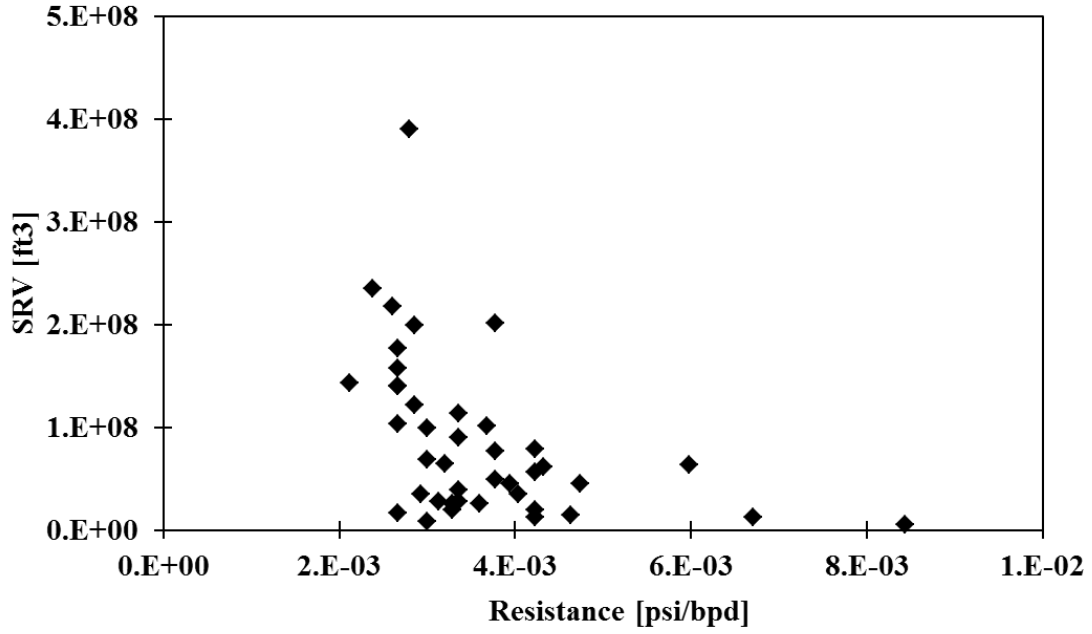

Figure 4.3: Resistance obtained from our model's interpretation of water hammer data plotted versus stimulated reservoir volume (SRV).

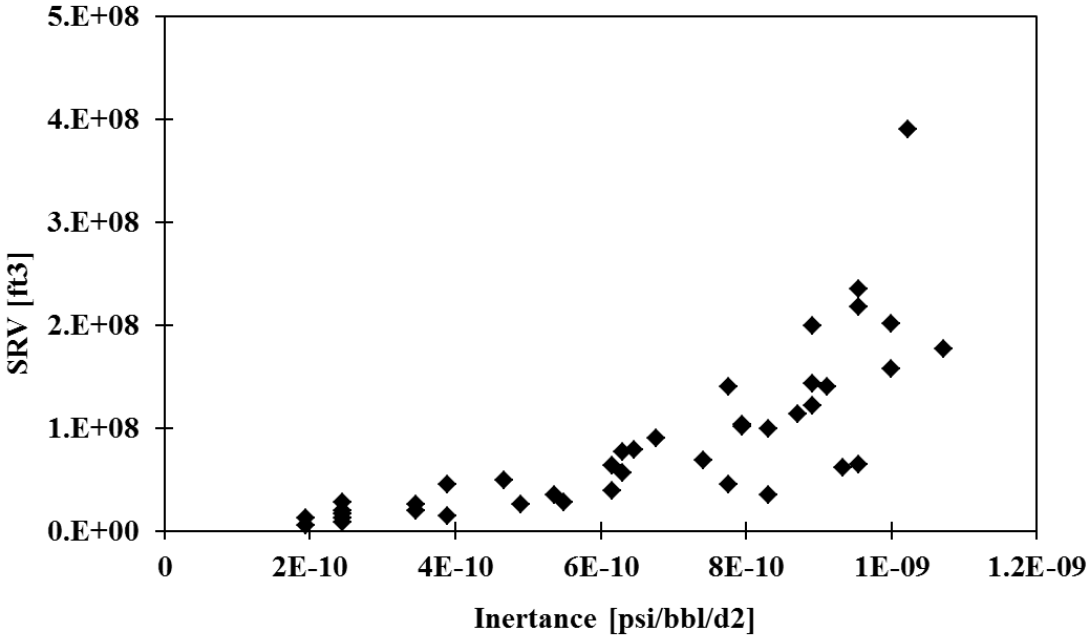

Figure 4.4: Inertance obtained from our model's interpretation of water hammer data plotted versus stimulated reservoir volume (SRV).

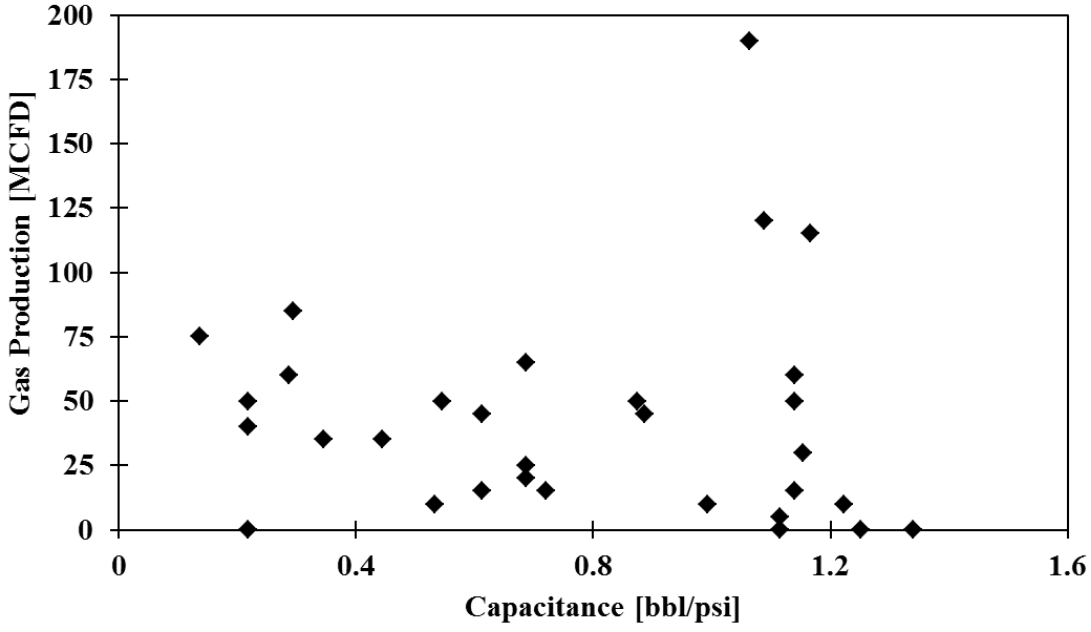

Figure 4.5: Capacitance obtained from our model's interpretation of water hammer data plotted versus gas production obtained from production logs.

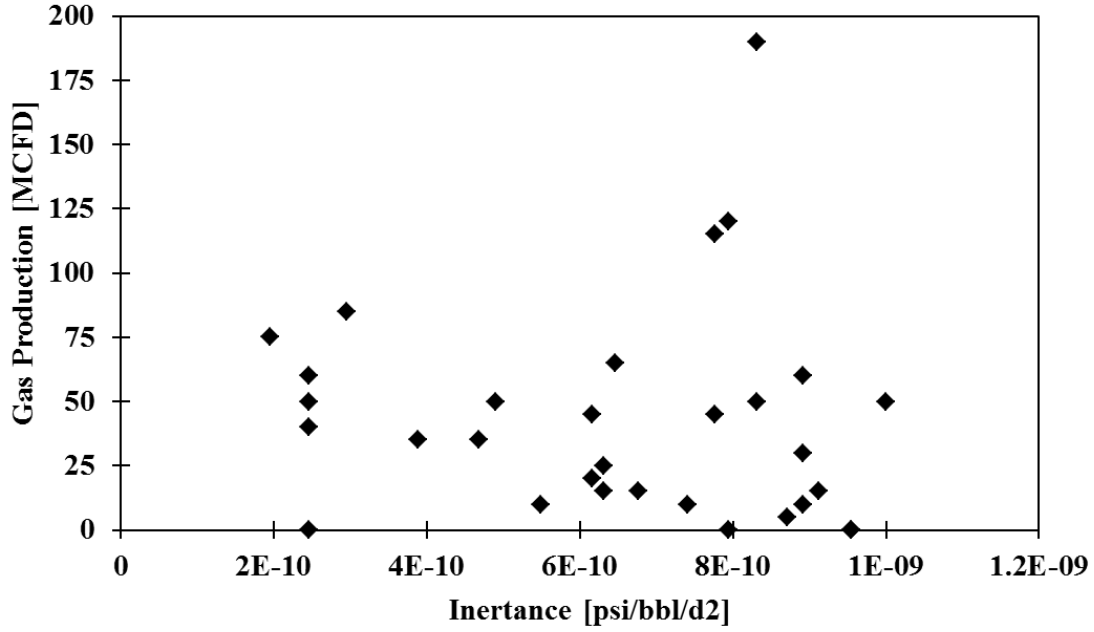

.

Figure 4.6: Inertance obtained from our model's interpretation of water hammer data plotted versus gas production obtained from production logs.

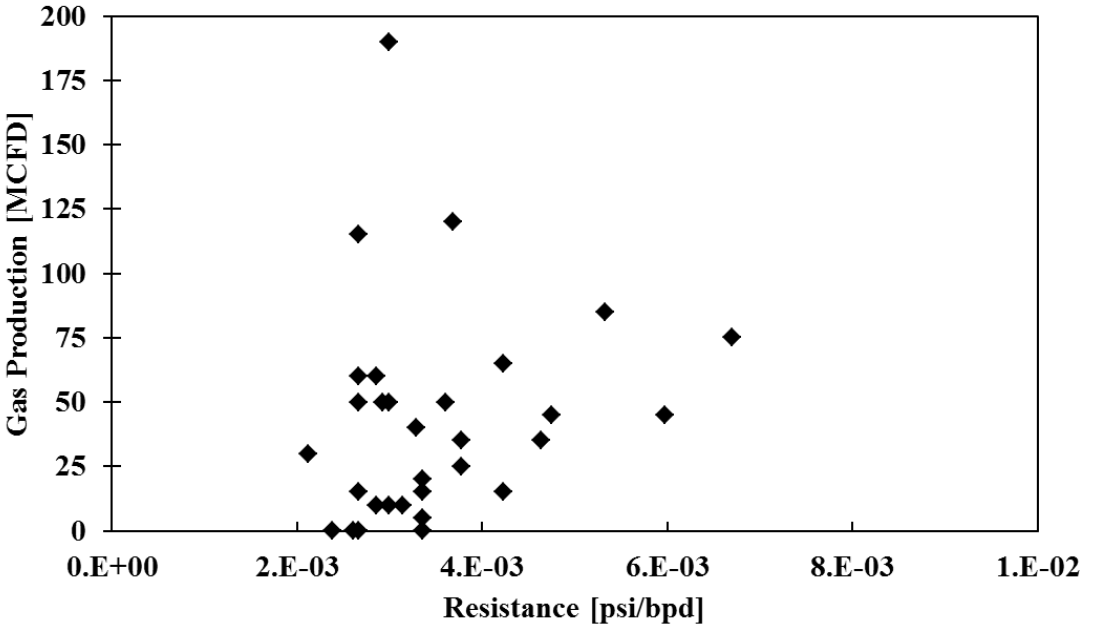

Figure 4.7: Resistance obtained from our model's interpretation of water hammer data plotted versus gas production obtained from production logs.

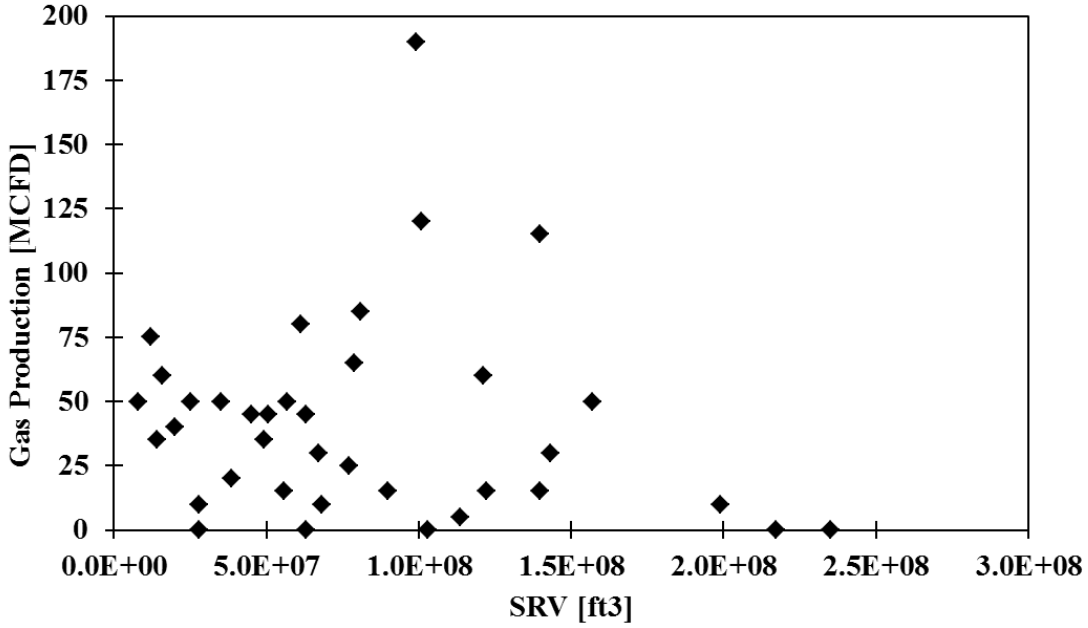

Figure 4.8: Stimulated reservoir volume (SRV) plotted versus gas production obtained from production logs.

4.3 SIMULATED BOTTOM-HOLE PRESSURES

The *RCI* numerical model was capable of simulating bottomhole pressures (P_{BH}) during water hammer events, as shown below in Fig. 4.9 for stage 1 of well A. Accurate predictions of P_{BH} for any specific shutdown procedure could aid in selecting a shutdown procedure that reduces formation damage due to pressure surges.

Accurate estimation of P_{BH} also yielded a more exact assessment of the instantaneous shut-in pressure (P_{ISIP}). Eq. (4.1) below shows how P_{ISIP} was calculated from P_{BH} and P_{nwf} obtained from the numerical model.

$$P_{BH} - P_{nwf} = P_{ISIP} \tag{4.1}$$

Since P_{nwf} included perforation and near-wellbore friction, the calculated P_{ISIP}'s were devoid of perforation friction, and more accurate than the current industry practice of estimating P_{ISIP} from surface pressure.

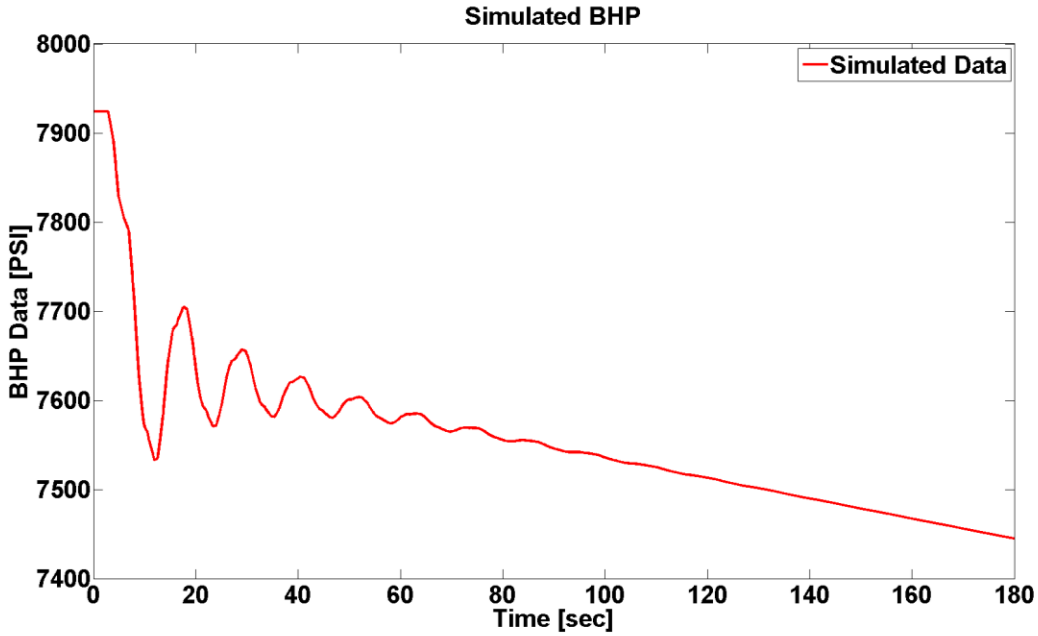

Figure 4.9: Simulated bottomhole pressure for shutdown event 1 of stage 1, well A.

4.4 FRACTURE TREATMENT DIAGNOSTIC TOOL

Several fracture treatments had multiple shutdowns per stage. The treatment plots of Well A, stage 1, and Well C, stage 10 are shown below if Fig. 4.10 and 4.11 respectively, with the shutdown events indicated by black circles. All water hammer signals throughout the treatment were history matched and compared. Table 4.1 below shows the R, C, and I values obtained. In each case fracture growth was observed through an increase in capacitance and equivalent fracture length. There was a large increase in resistance for the second shutdown event of Well A, which corresponds with the increased pressure prior to shutdown which is indicative of a screen-out.

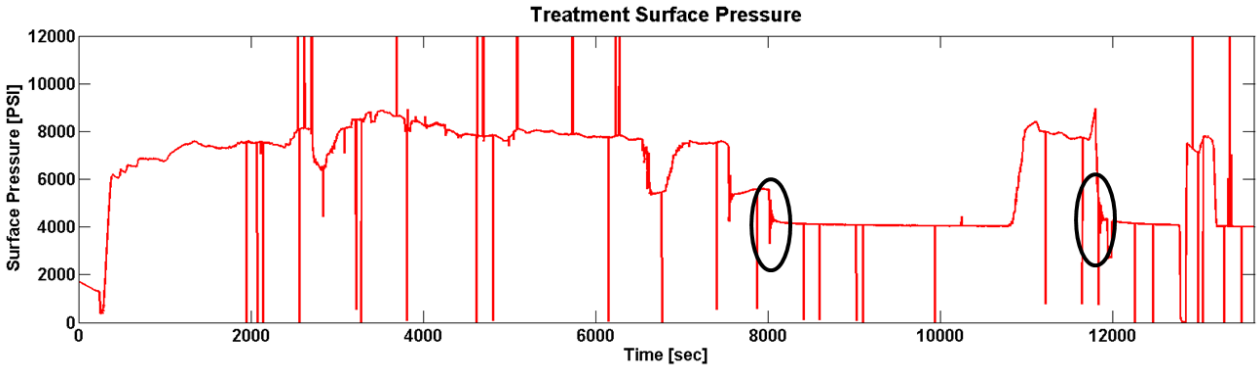

Figure 4.10: Surface pressure profile that depicts the two shutdown events of Well A, stage 1. (Note: large fluctuations due to bad transducer or cable)

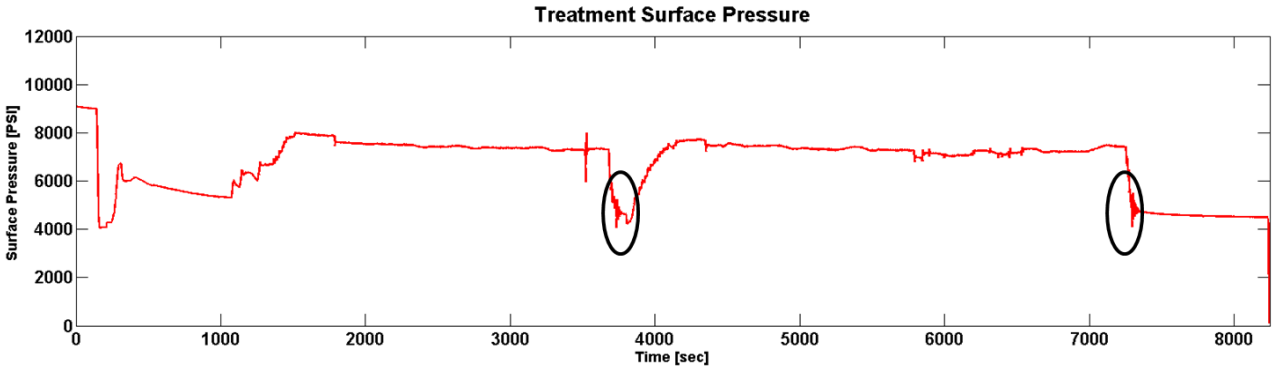

Figure 4.11: Surface pressure profile that depicts the two shutdown events of Well C, stage 10

Well	Stage	Event	R [bpd/psi]	C [bbl/psi]	I [psi/bbl/d2]	Height [ft]	Half-Length [ft]	Width [in]
A	1	1	4.04E-03	0.487	5.37E-10	100	602	1.782
A	1	2	5.20E-03	0.656	7.08E-10	100	811	1.847
C	10	1	5.33E-03	0.293	2.95E-10	100	366	1.836
C	10	2	3.28E-03	0.386	3.47E-10	101	465	1.974

Table 4.1: Summary of *RCI* values and fracture dimensions for the multiple shutdown events from Wells A and C.

4.5 FRACTURE COMPLEXITY INDEX CORRELATIONS

The fracture complexity index (FCI), defined by Cipolla et al. (2008), is the ratio of micro-seismic cloud width to length, shown below in Eq. (4.2), in which higher FCI values indicate increased fracture complexity. An image of micro-seismic SRV data, shown below in Fig.4.12, indicates how width and length were acquired.

$$FCI = \frac{Width_{microseismic}}{Length_{microseismic}} \tag{4.2}$$

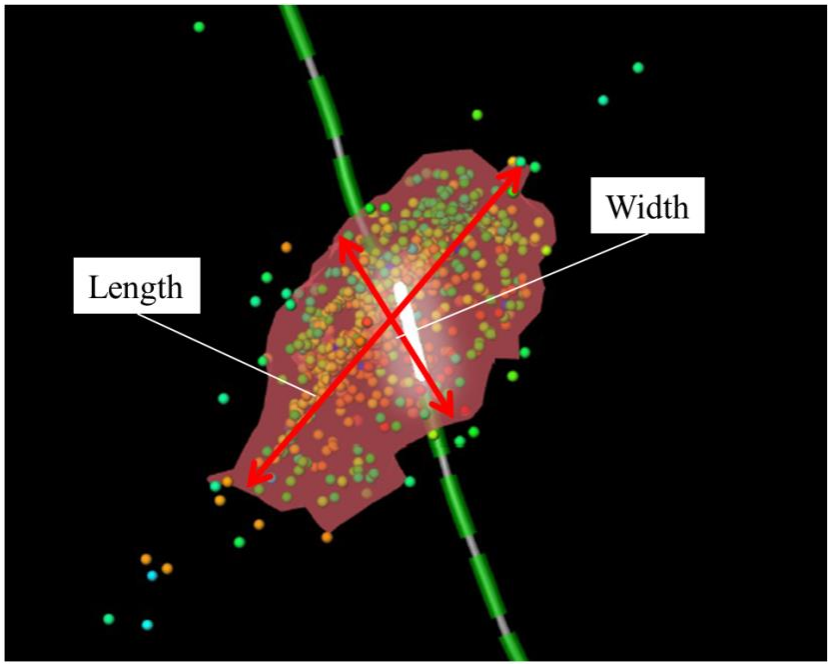

Figure 4.12: Visual description of how micro-seismic width and length were obtained from SRV data.

FCI values were compared to *R*, *C*, and *I* as well as the ratio of calculated width to length. Resistance exhibited a slight positive correlation with FCI, shown below in Fig. 4.13, which may indicate that fractures with a higher degree of complexity have an increased near-wellbore resistance. Both capacitance and inertance were inversely

correlated with FCI, shown below in Figs. 4.14 and 4.15 respectively. This is in agreement with previously obtained results that higher capacitance and inertance values indicate larger created fractures. The ratio of calculated width to length had a positive correlation with FCI, shown below in Fig. 4.16. Since fracture length and width are calculated from *RCI* values, Fig. 4.16 further supports that the obtained *R*, *C*, and *I* values accurately describe created hydraulic fractures.

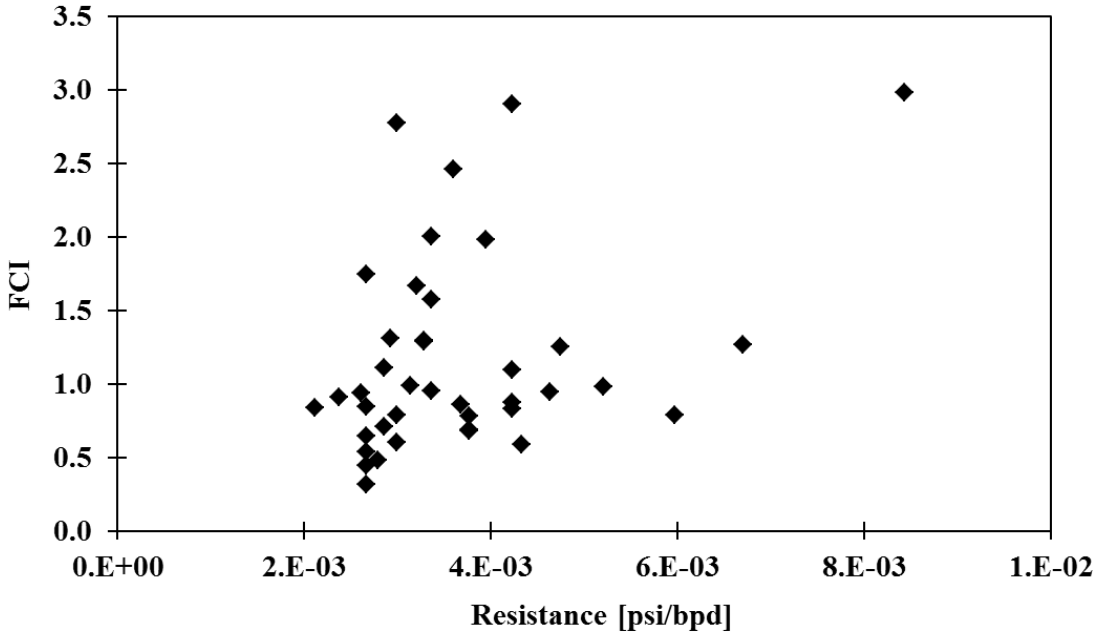

Figure 4.13: Resistance versus fracture complexity index (FCI).

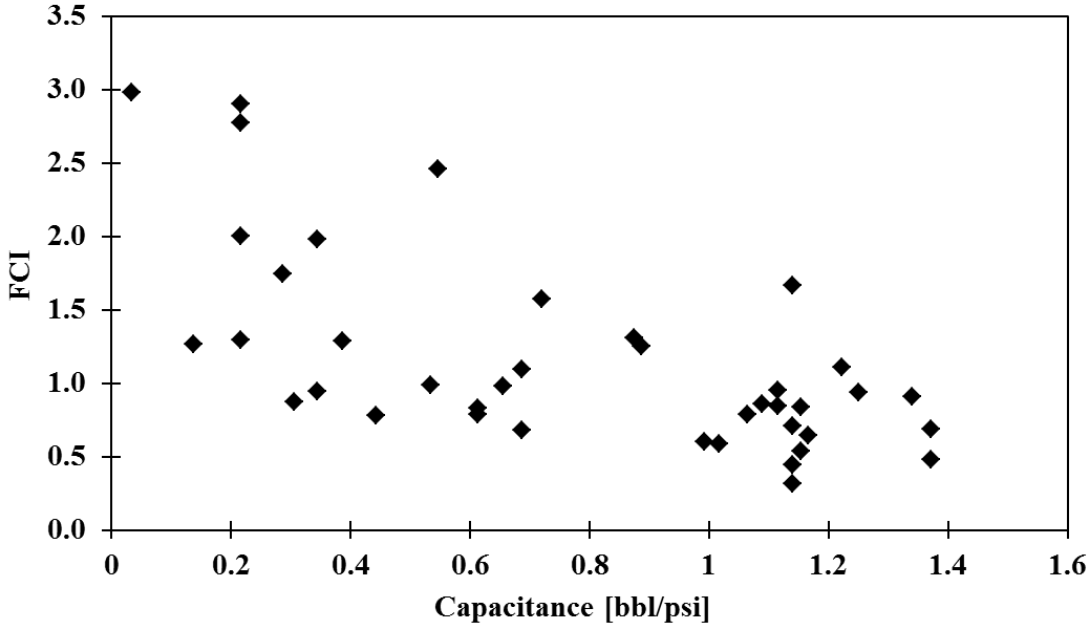

Figure 4.14: Capacitance versus fracture complexity index (FCI).

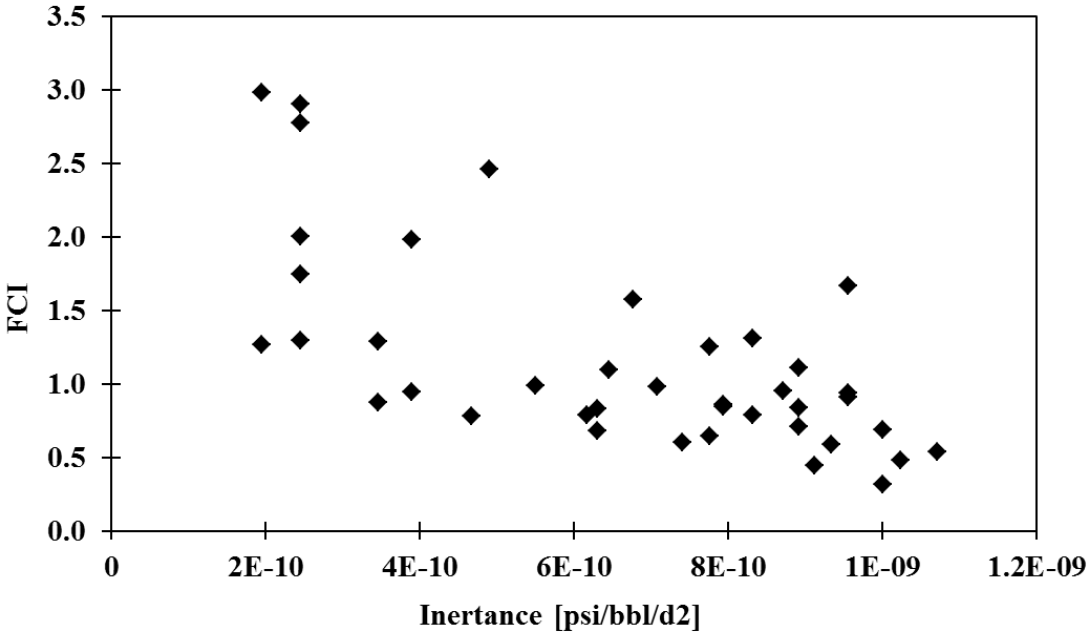

Figure 4.15: Inertance versus fracture complexity index (FCI).

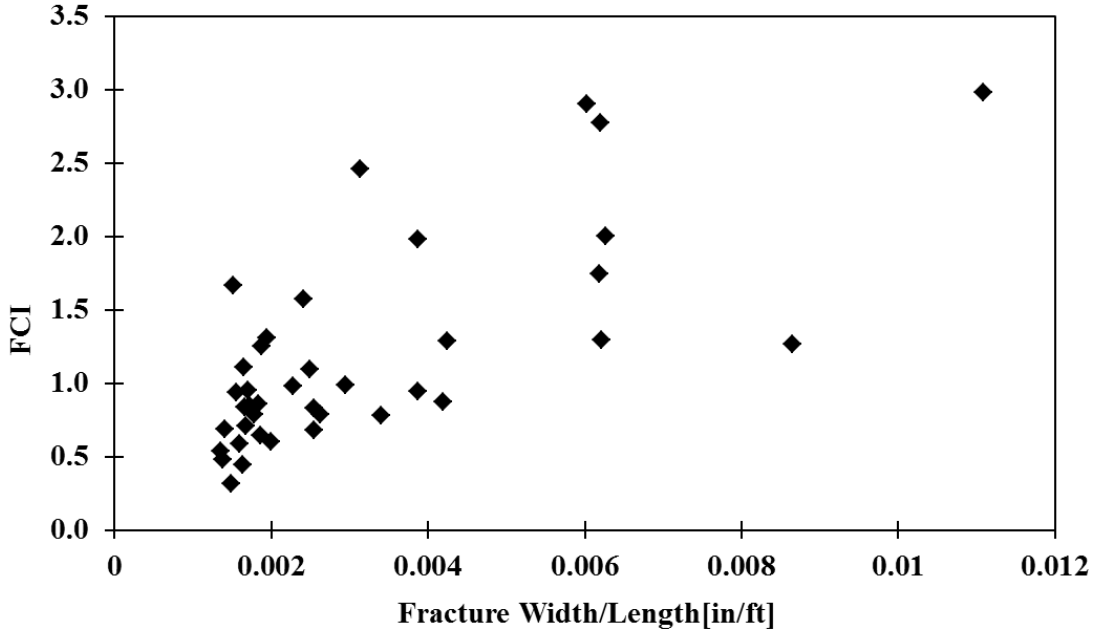

Figure 4.16: Ratio of calculated width to length versus fracture complexity index (FCI).

4.6 WAVELENGTH IDENTIFICATION WITH FOURIER TRANSFORMS

A fast Fourier Transform (FFT) was performed on field data with the hypothesis that water hammer events comprised of several dominant frequencies, either from reflections from the end of the wellbore or communication with nearby zones, such as depicted in Fig. 4.17 below, may be observable.

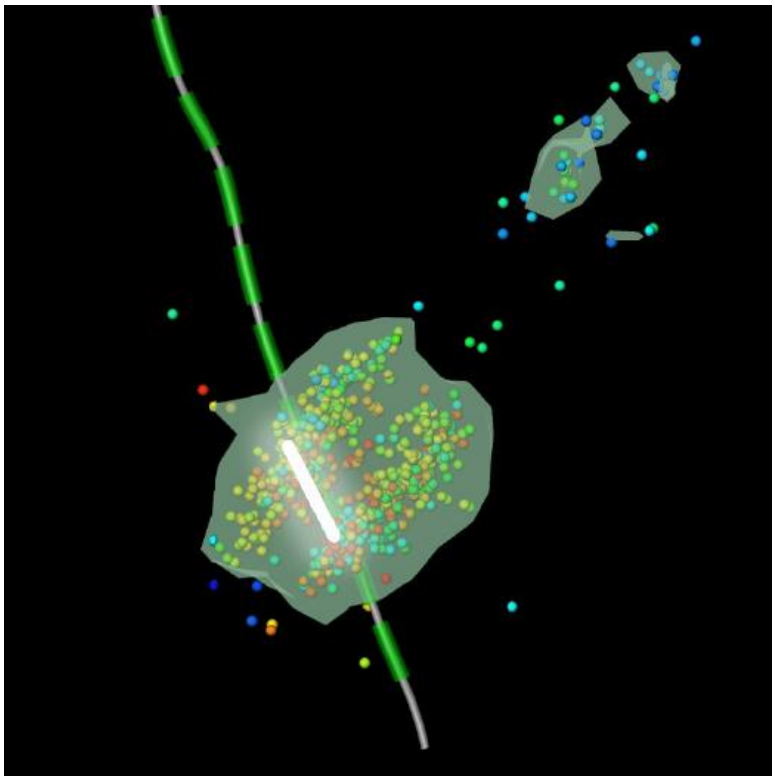

Figure 4.17: Micro-seismic events showing communication with an adjacent zone during stimulation treatment either due to poor cement job or leaky packer for stage 3 of well B.

FFT results were inconclusive, however, since the short distance between zones required a sampling rate of at least 100 samples per second to capture an observable signal in the high frequency domain. An example of an FFT is shown below in Fig. 4.18 for stage 3 of Well B. The dominant frequency of 10.6 seconds is clearly observable, which corresponds to T = 4L/a, but any influences of the adjacent zone cannot be distinguished due to the low pressure sampling rate of 1 sample per second. Higher resolution data, on the order of 100+ samples per second, could capture the reflections from nearby zones, and could indicate inter-zonal communication during hydraulic fracture treatments.

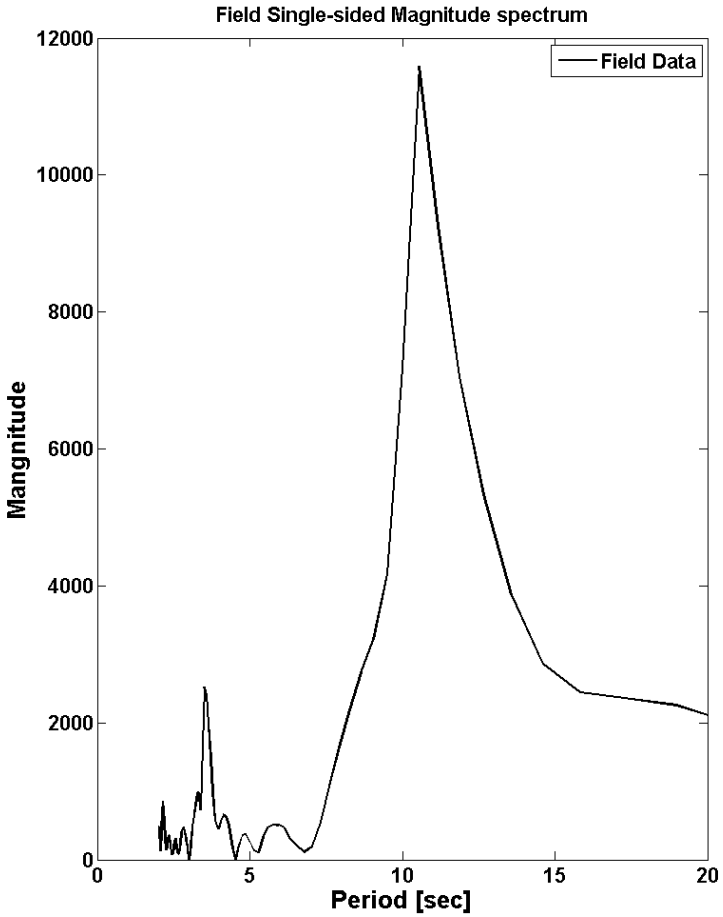

Figure 4.18: Fast Fourier Transform of Well B, Stage 3 which identifies the dominant period as 10.6 seconds, but fails to identify the period of the nearby zone due to low resolution of pressure data.

Chapter 5: Conclusion

A sudden change in flow in a confined system results in a pressure pulse known as a water hammer. The pressure pulse travels through the wellbore and interacts with created hydraulic fractures, altering the period, amplitude, and decay of the pressure transient. A hydrodynamic model was constructed based on the work of Mondal (2010), which linked the continuity and momentum equations of the wellbore with a downhole *RCI* series circuit boundary condition. This model was validated with the results of Mondal (2010), Holzhausen et al. (1985), and Ferrick et al. (1982).

Water hammer field data from 51 stages of 3 horizontal, multi-stage fractured wells were history matched with the numerical model through a systematic procedure that iteratively altered the resistance, capacitance, and inertance (*R*, *C*, and *I*) until an appropriate match was obtained. The resulting R, C, and I values were compared to other indirect measures of fracture geometry such as the SRV derived from micro-seismic data and production log data. Good correlations were found to exist between these two completely different methods of estimating fracture geometry.

Capacitance was directly correlated with SRV, while resistance was inversely correlated with SRV. These relationships allow for SRV approximations from water hammer data alone, supporting the claim that there is valuable information present in water hammer signals of fractured wells.

Fracture dimensions were calculated from *R*, *C*, and *I* values based on the derivations of Mondal (2010) and Shylapobersky et al. (1988). The obtained dimensions were considered equivalent fracture dimensions since most treatment stages create multiple hydraulic fractures instead of one planar fracture.

Bottom-hole pressures were simulated with the *RCI* numerical model which could aide in designing safe shutdown procedures. Simulated bottom-hole pressures also led to a more accurate determination of instantaneous shut-in pressures, free of friction.

The analysis of several shutdown events throughout a single hydraulic fracturing treatment stage indicated that fracture dimensions changed and fracture growth had occurred. This could lead to a diagnostic method that periodically checks on the progress of stimulation treatments.

The fracture complexity index (FCI), defined by Cipolla et al. (2008) as the ratio of SRV cloud width to length, was compared to the *R*, *C*, and *I* obtained here from water hammer data. A weak correlation between resistance and FCI was noted, as well as an inverse correlation between FCI and both capacitance and inertance. A direct correlation between calculated width to length ratios and FCI values demonstrated that the *R*, *C*, and *I* numerical model results were in agreement with acquired micro-seismic data.

Finally, fast Fourier Transforms were performed on the field data to test the hypothesis that adjacent zones in communication with the target zone through either a failed cement job or packer could be identified by the presence of a combination of oscillation periods or frequencies. Combinations of water hammer periods, however, were not able to be observed due to the low time resolution of the field data. Higher resolution pressure data, on the order of 100+ samples per second, are needed to observe the desired effect.

Appendices

Appendix A: Elliptical Integral Equations

Appendix B: Oscillation Profiles for Varying *R*, *C*, and *I*

Appendix C: Field Data and Numerical Model History Matches

Appendix D: Tables of RCI values and Fracture Dimensions

Appendix A: Elliptical Integral Equations

Part 1: The complete elliptical integral of the first kind is given by *K* as:

$$K(m) = \int_0^{\frac{\pi}{2}} \frac{d\theta}{\sqrt{1-m^2\sin^2\theta}} = \int_0^1 \frac{dt}{\sqrt{(1-t^2)(1-m^2t^2)}}$$

K can be numerically approximated as follows:

$$K(1-x) = (c_0 + c_1x + c_2x^2) + (d_0 + d_1x + d_2x^2)\log(\frac{1}{x})$$

Where c_0 = 1.3862944, c_1 = 0.1119723, c_2 = 0.0725296, d_1 = 0.1213478, and d_2 = 0.0288729.

Part 2: The complete elliptical integral of the second kind is given by *E* as:

$$E(m) = \int_0^{\frac{\pi}{2}} \sqrt{1-m^2\sin^2\theta}\,d\theta = \int_0^1 \frac{\sqrt{1-m^2t^2}}{1-t^2}dt$$

E can be numerically approximated as follows:

$$E(1-x) = (1 + a_1x + a_2x^2) + (b_1x + b_2x^2)\log(\frac{1}{x})$$

Where a_1 = 0.4630151, a_2 = 0.2452727, b_1 = 0.1077812, and b_2 = 0.0412496

Appendix B: Oscillation Profiles for Varying *R*, *C*, and *I*

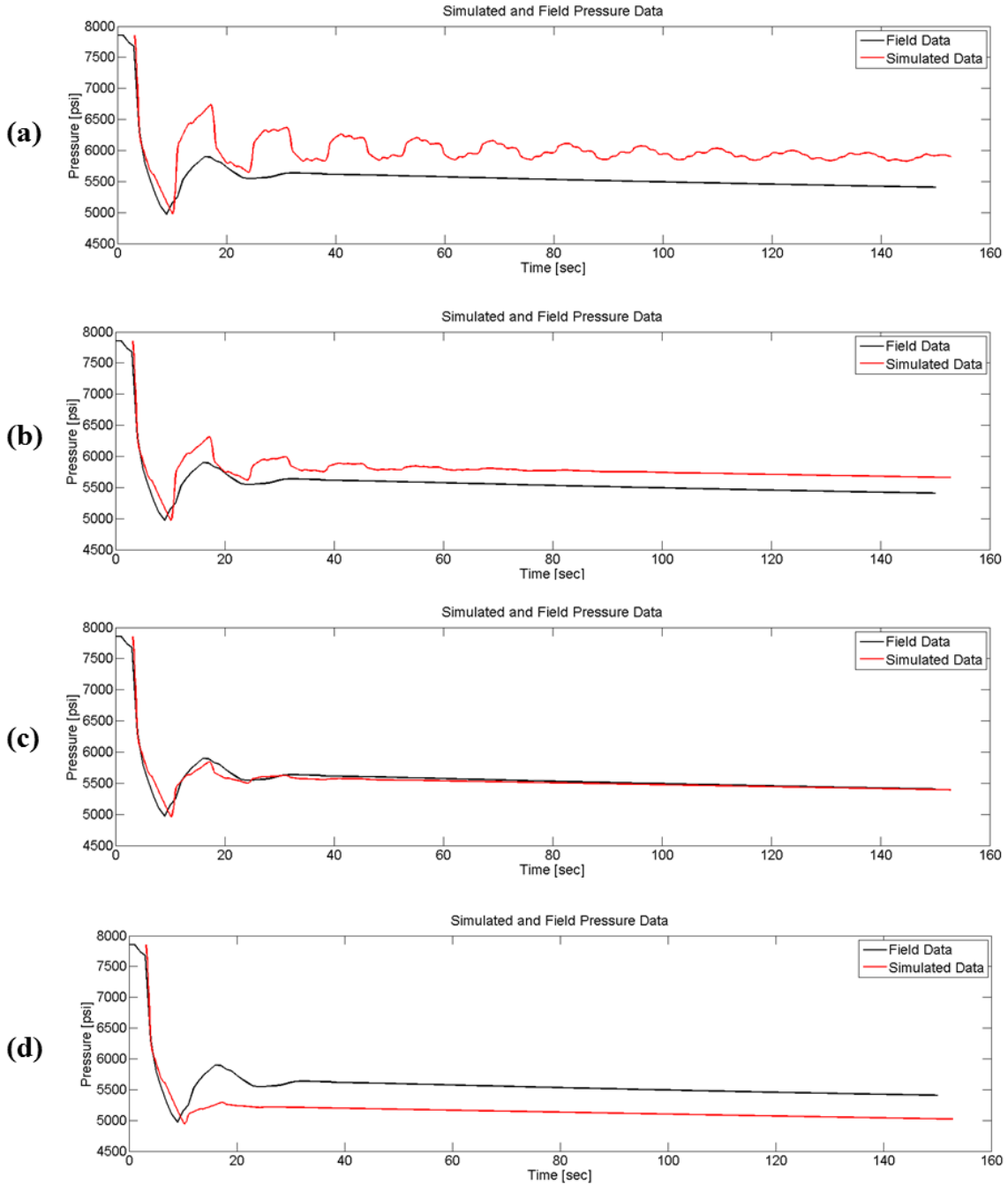

Figure B.1: Oscillation profiles for resistances of (a) 2.67×10^{-6} psi/bpd, (b) 8.44×10^{-3} psi/bpd, (c) 1.89×10^{-2} psi/bpd, and (d) 3.36×10^{-2} psi/bpd at a fixed C and I of 1.37×10^{-3} ^{3} bbl/psi, and 2.45×10^{-10} psi/bbl/d^{2} respectively.

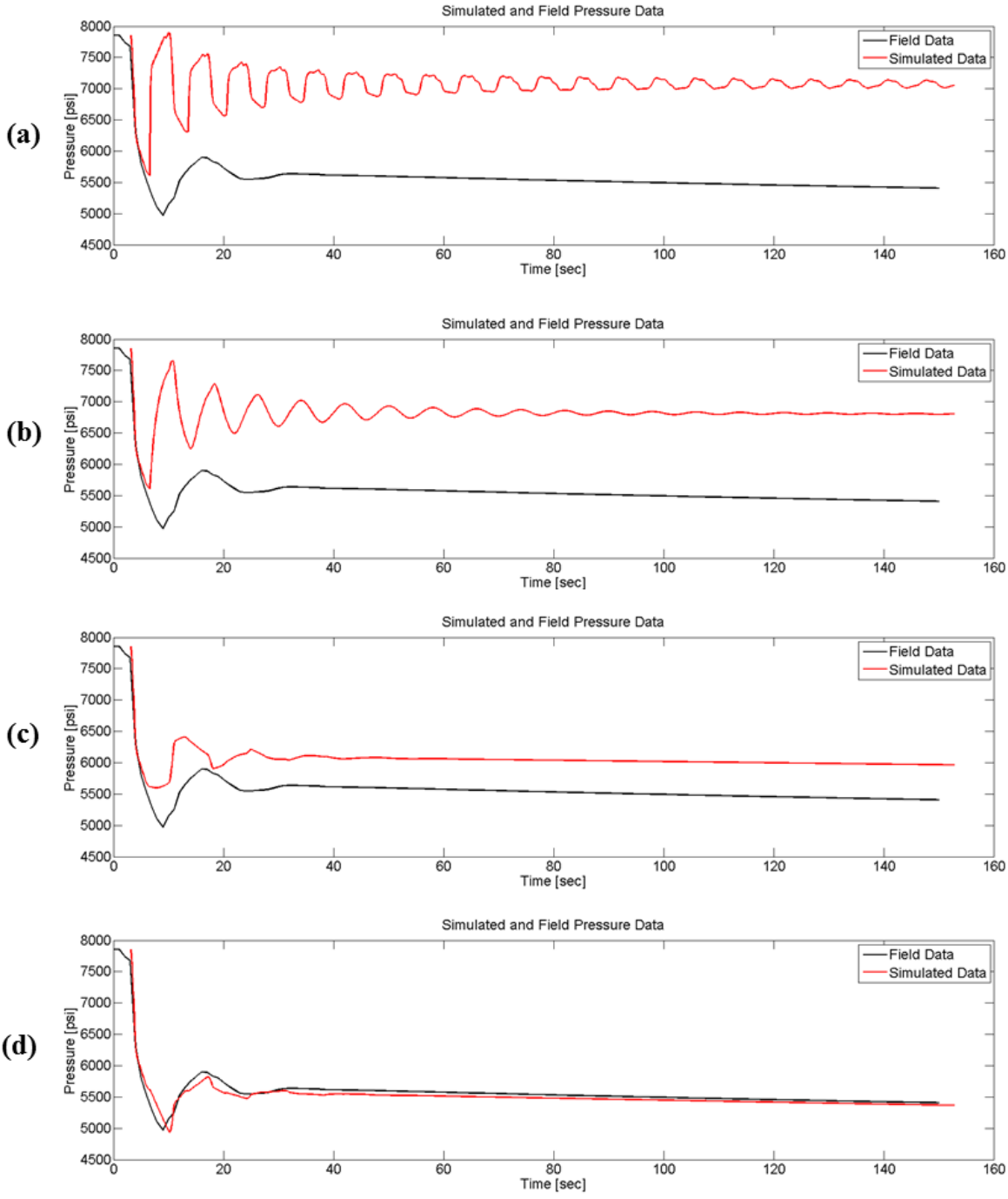

Figure B.2: Oscillation profiles for capacitances of (a) 4.34×10^{-6} bbl/psi, (b) 1.37×10^{-4} bbl/psi, (c) 1.37×10^{-3} bbl/psi, and (d) 1.37 bbl/psi at a fixed R and I of 1.89×10^{-2} psi/bpd and 2.45×10^{-10} psi/bbl/d^2 respectively.

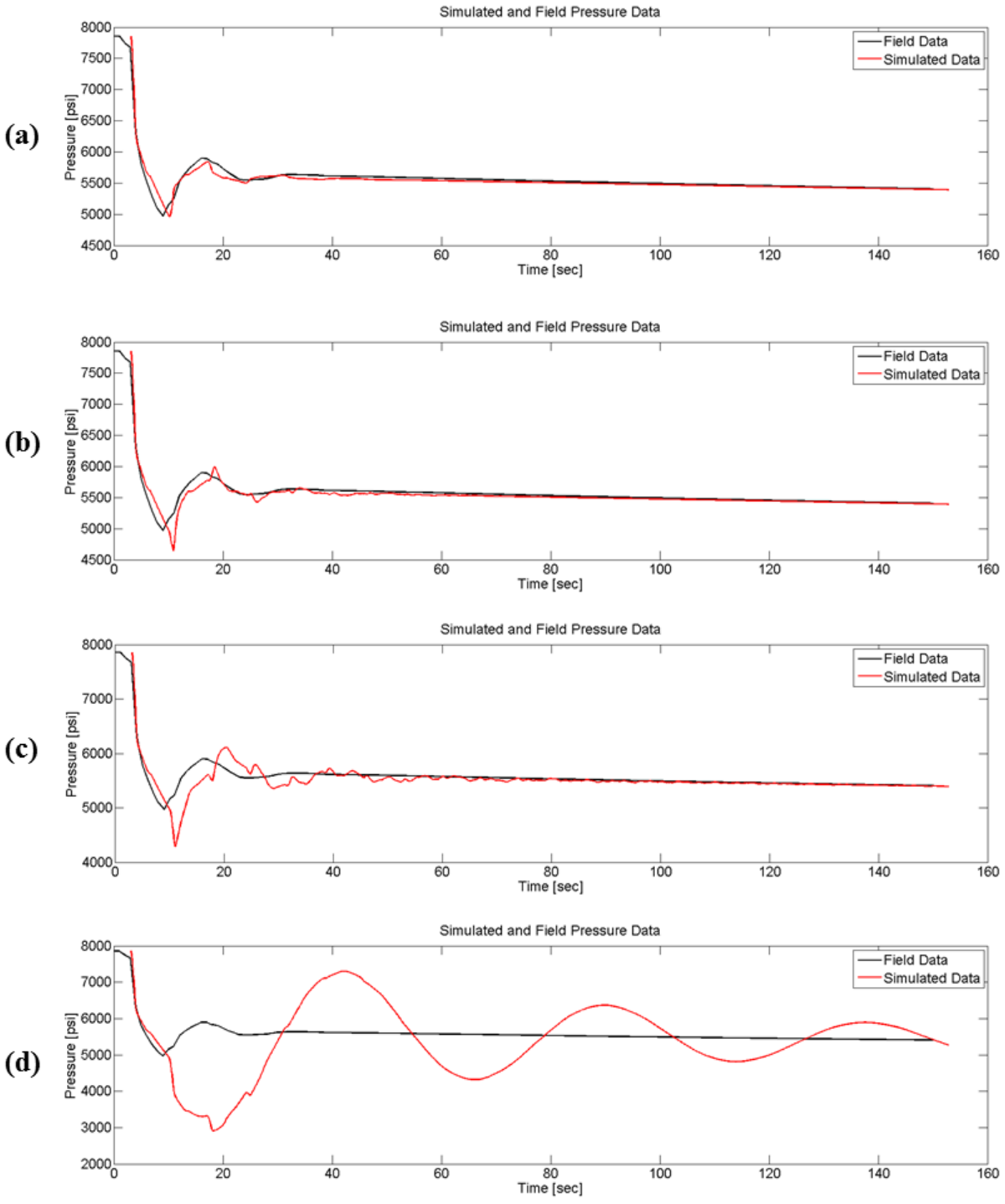

Figure B.3: Oscillation profiles for inertances of (a) 3.09×10^{-10} psi/bbl/d^2, (b) 3.09×10^{-7} psi/bbl/d^2, (c) 9.77×10^{-7} psi/bbl/d^2, and (d) 9.77×10^{-6} psi/bbl/d^2 at a fixed R and C of 1.89×10^{-2} psi/bpd 1.37×10^{-3} bbl/psi respectively.

Appendix C: Field Data and Numerical Model History Matches

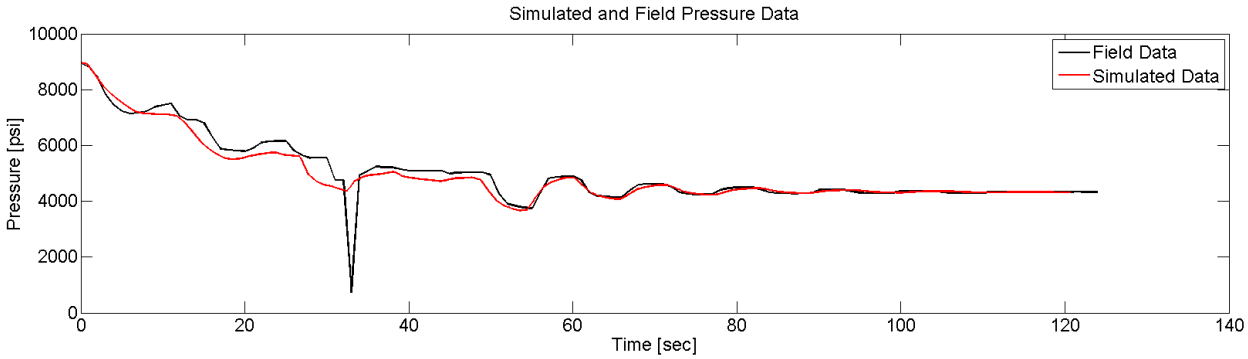

Figure C.1: History match of well A, stage 1, shutdown 2 field data with numerical model results

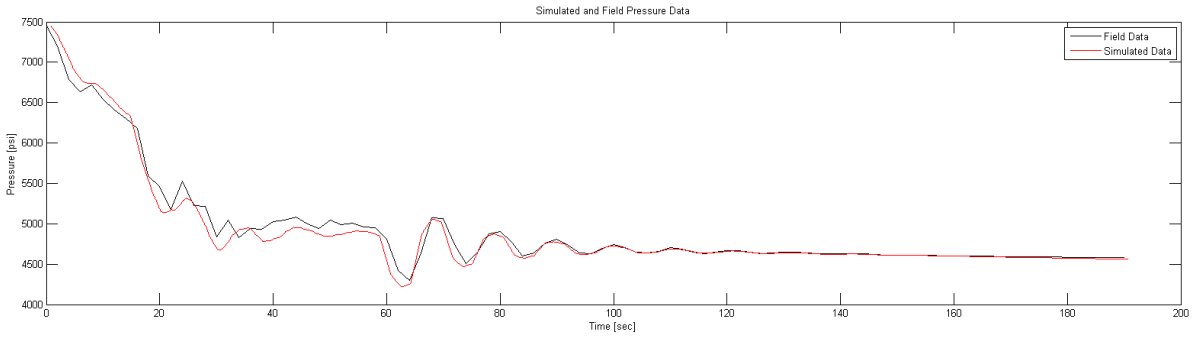

Figure C.2: History match of well A, stage 3 field data with numerical model results

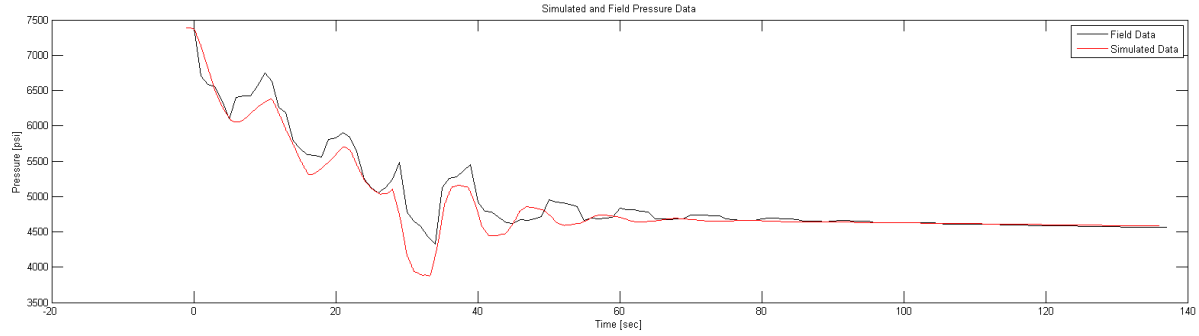

Figure C.3: History match of well A, stage 4 field data with numerical model results

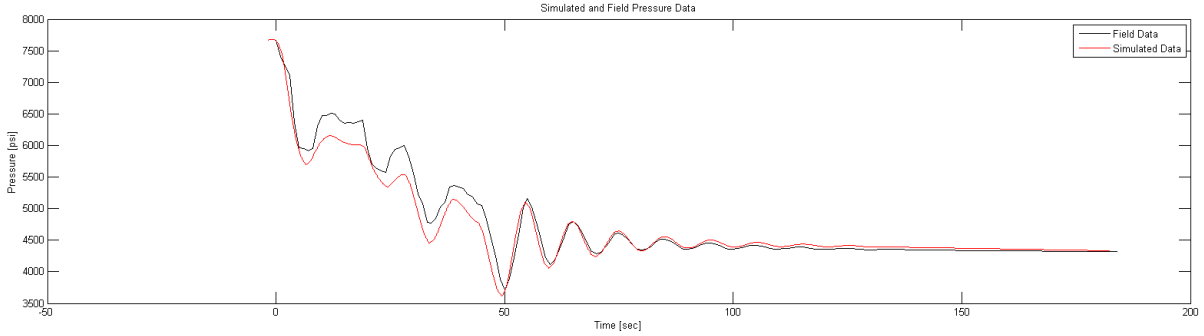

Figure C.4: History match of well A, stage 5 field data with numerical model results

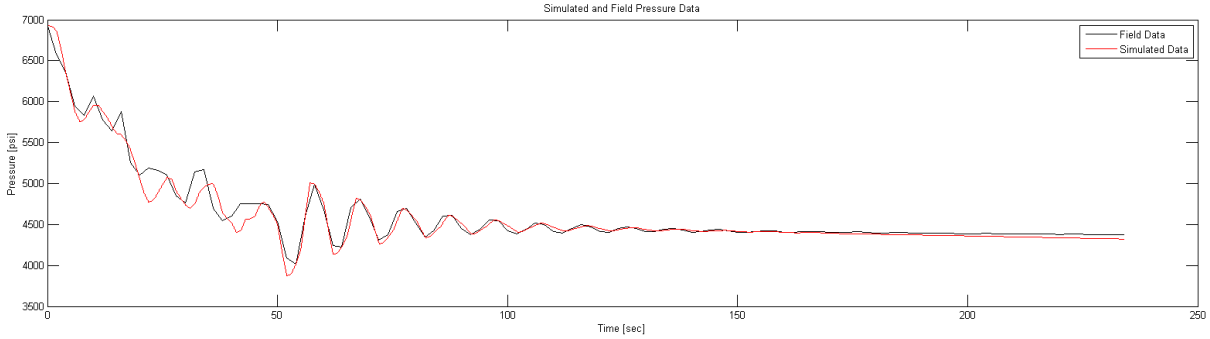

Figure C.5: History match of well A, stage 6 field data with numerical model results

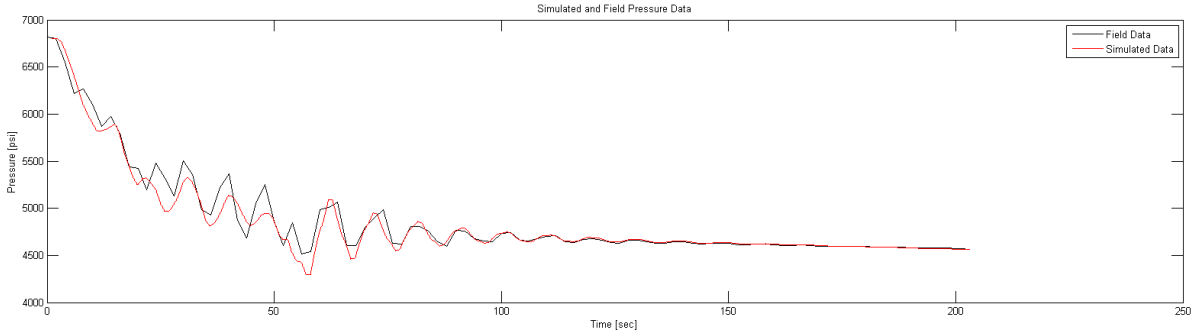

Figure C.6: History match of well A, stage 7 field data with numerical model results

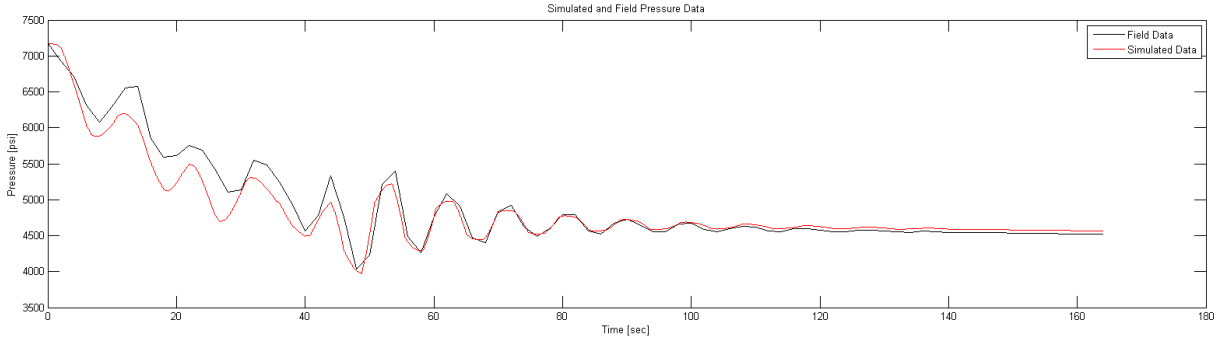

Figure C.7: History match of well A, stage 8 field data with numerical model results

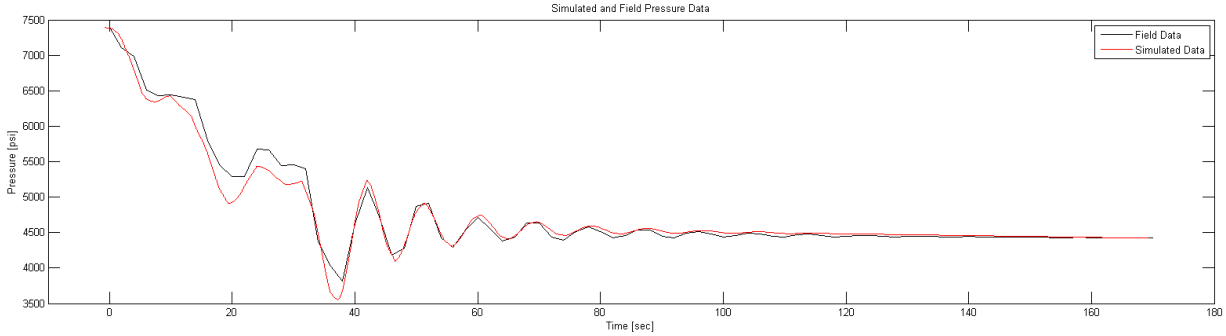

Figure C.8: History match of well A, stage 9 field data with numerical model results

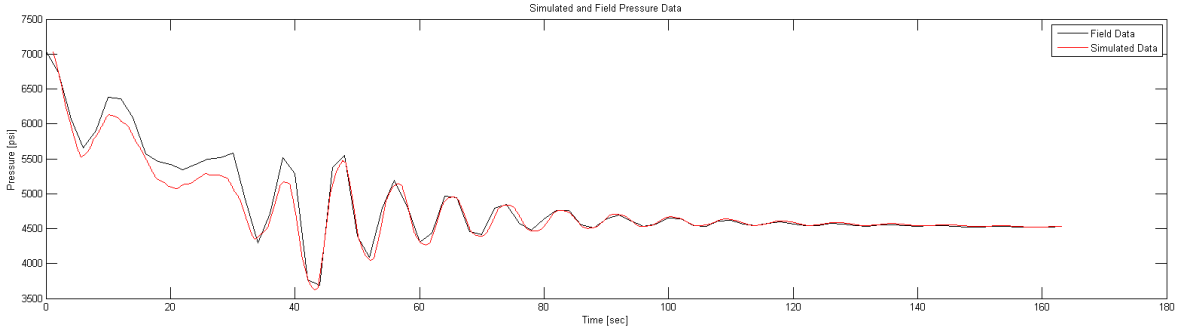

Figure C.9: History match of well A, stage 10 field data with numerical model results

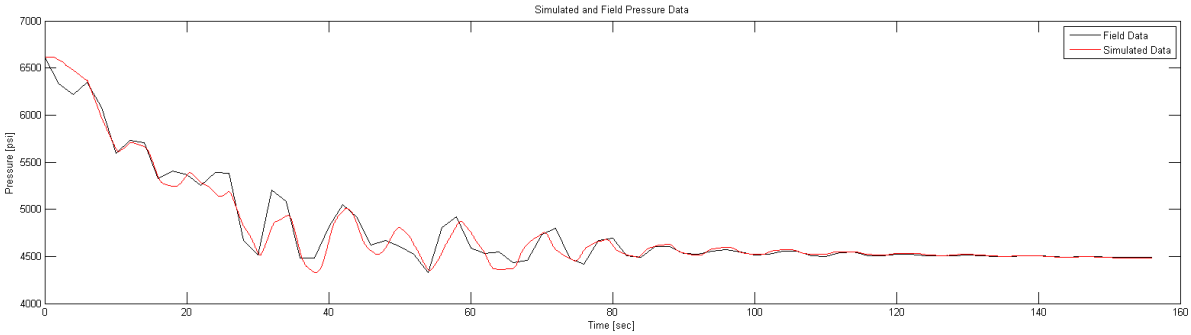

Figure C.10: History match of well A, stage 11 field data with numerical model results

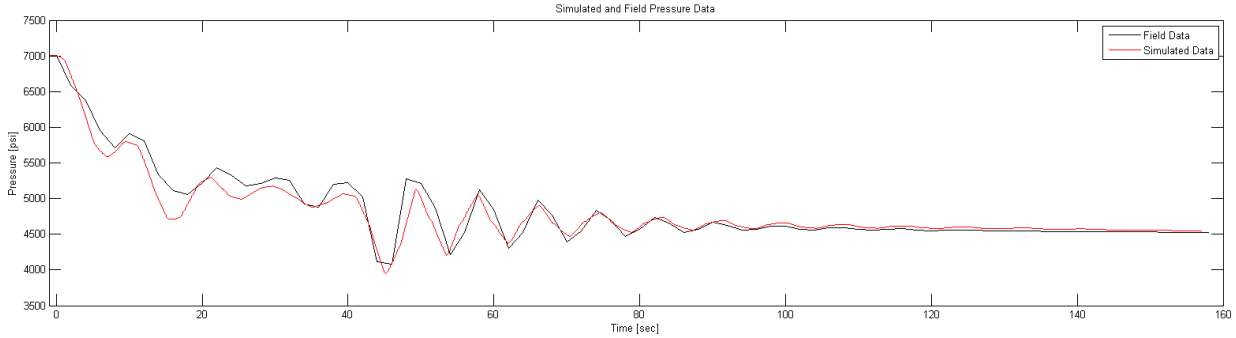

Figure C.11: History match of well A, stage 12 field data with numerical model results

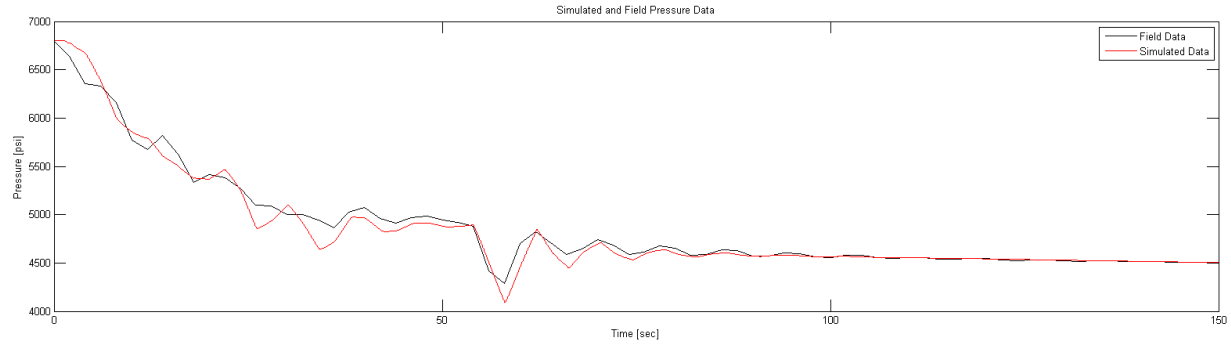

Figure C.12: History match of well A, stage 13 field data with numerical model results

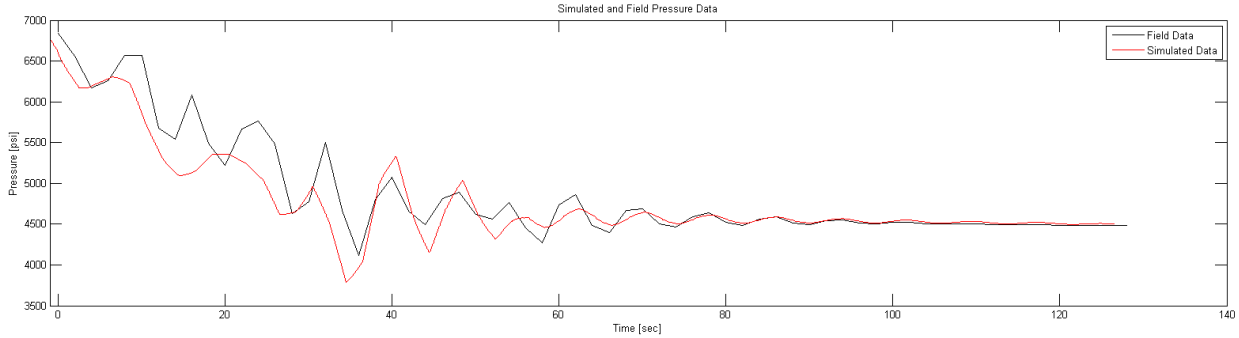

Figure C.13: History match of well A, stage 14 field data with numerical model results

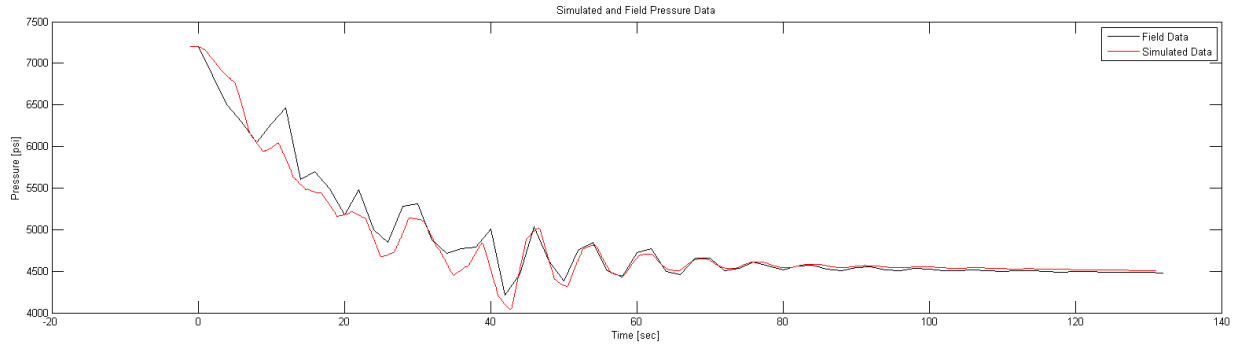

Figure C.14: History match of well A, stage 15 field data with numerical model results

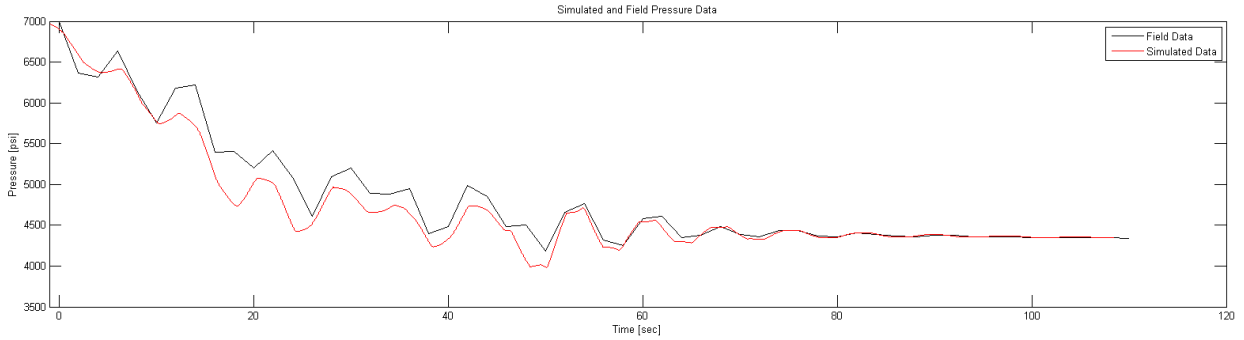

Figure C.15: History match of well A, stage 16 field data with numerical model results

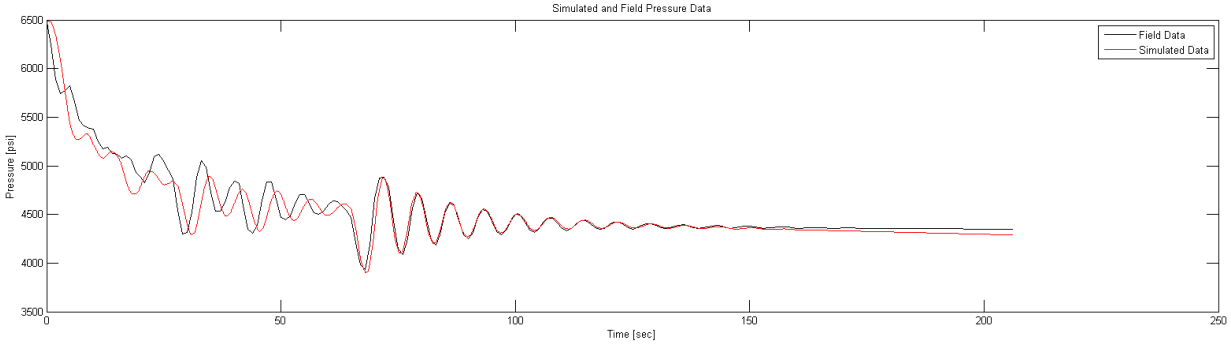

Figure C.16: History match of well A, stage 17field data with numerical model results

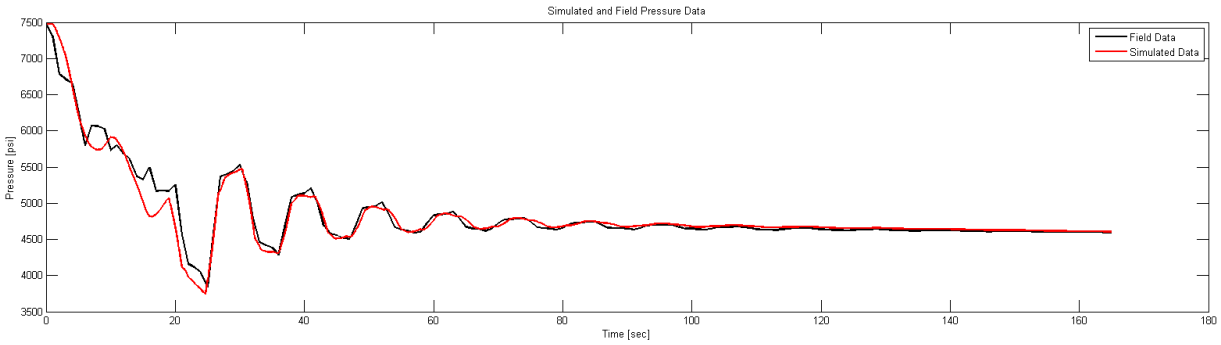

Figure C.17: History match of well B, stage 1 field data with numerical model results

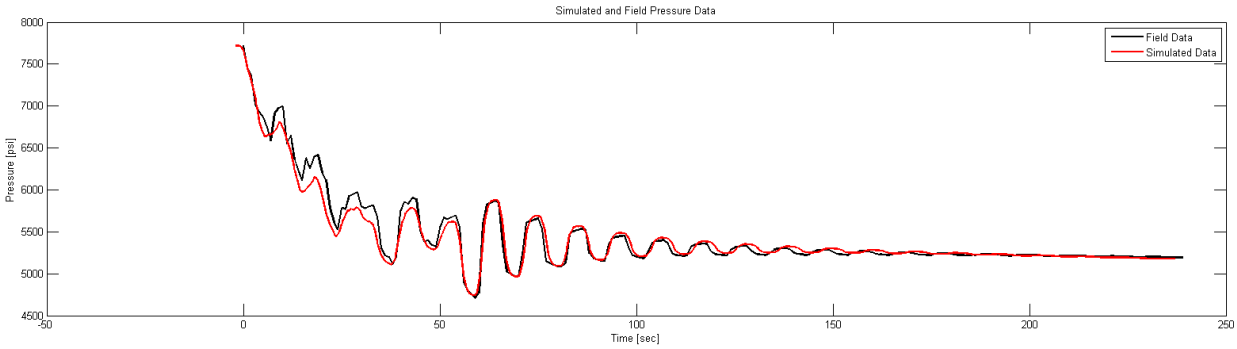

Figure C.18: History match of well B, stage 3 field data with numerical model results

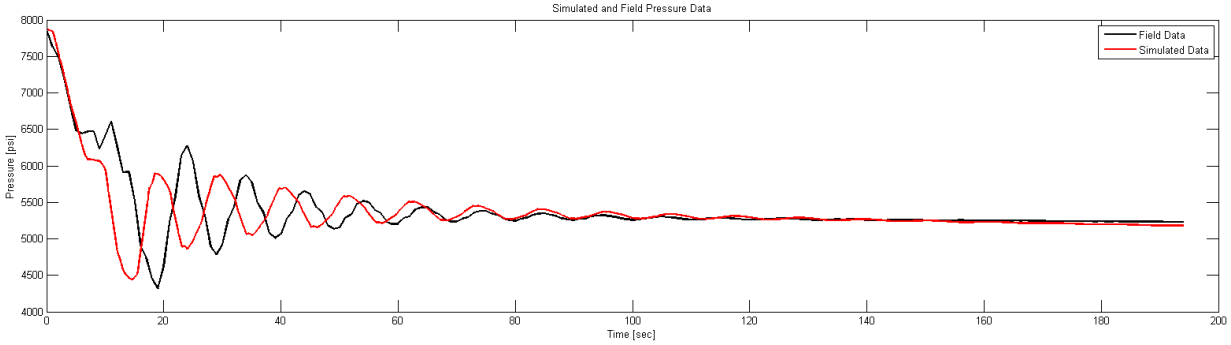

Figure C.19: History match of well B, stage 4 field data with numerical model results

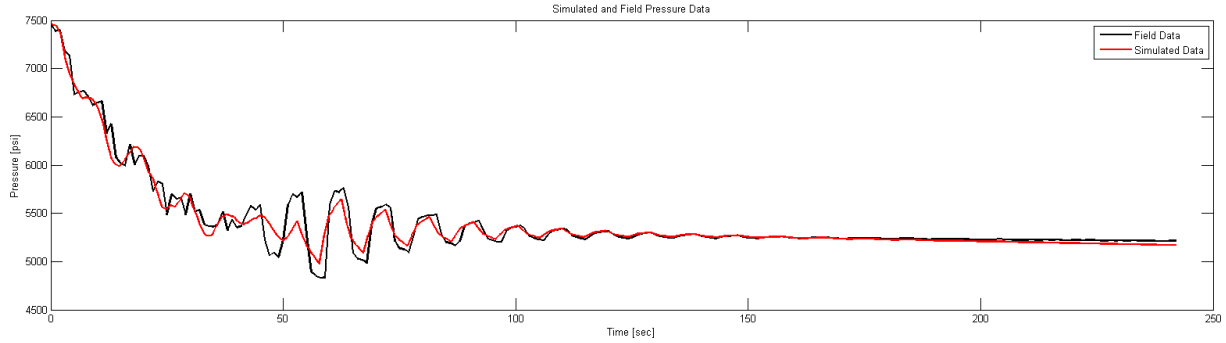

Figure C.20: History match of well B, stage 8 field data with numerical model results

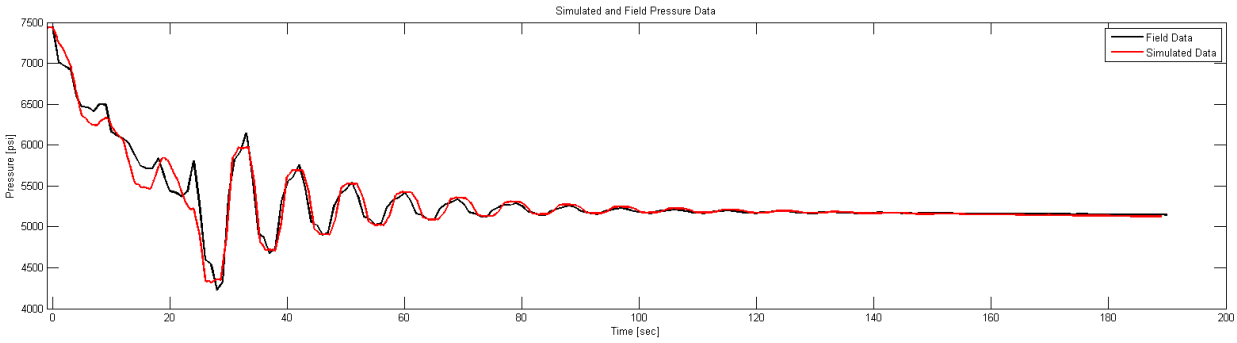

Figure C.21: History match of well B, stage 9 field data with numerical model results

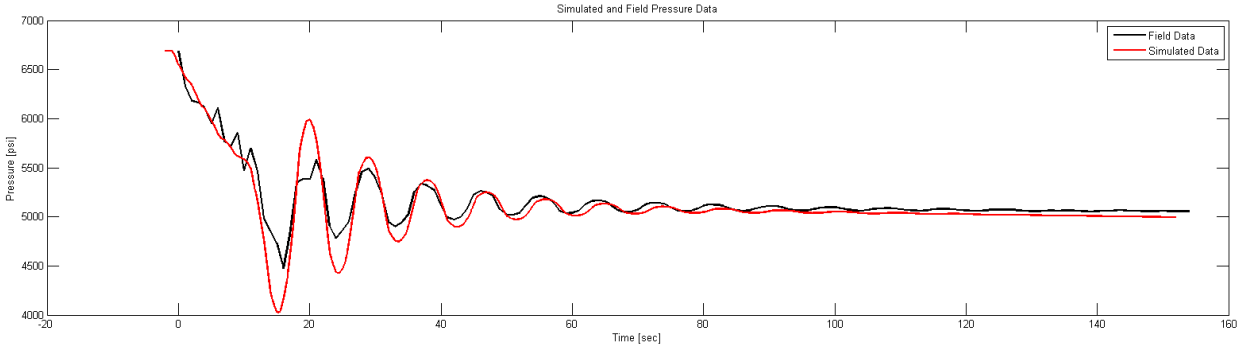

Figure C.22: History match of well B, stage 10 field data with numerical model results

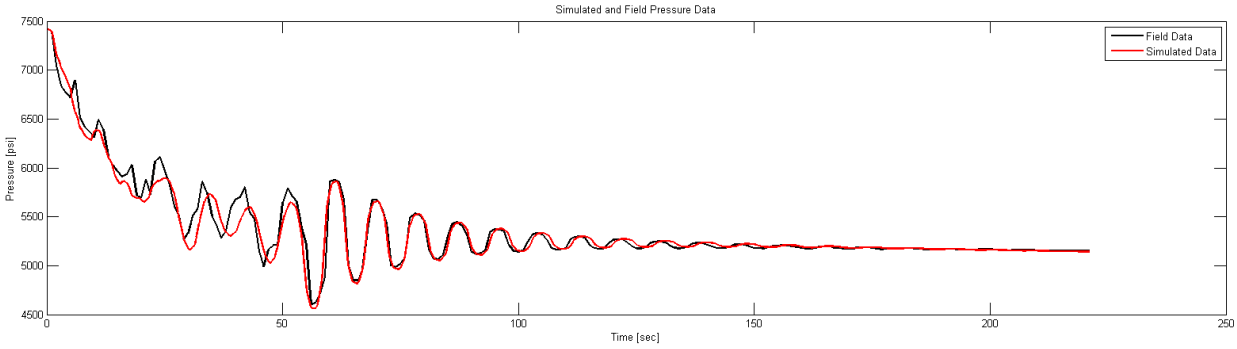

Figure C.23: History match of well B, stage 11 field data with numerical model results

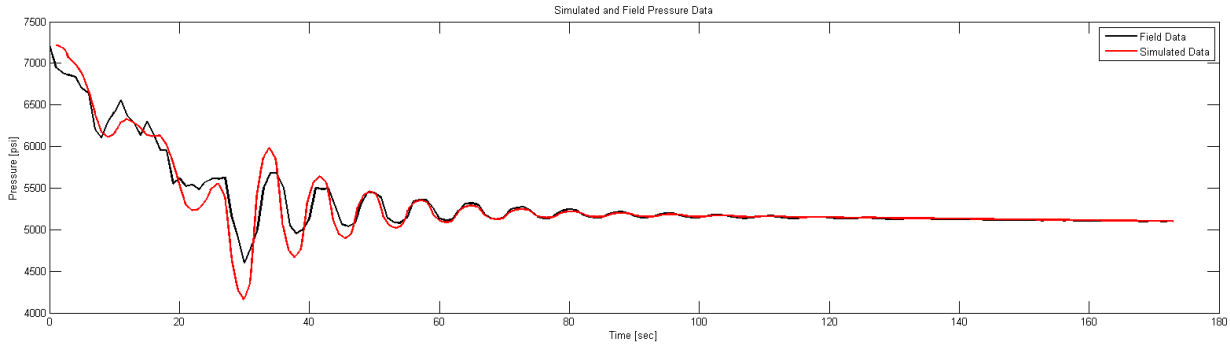

Figure C.24: History match of well B, stage 15 field data with numerical model results

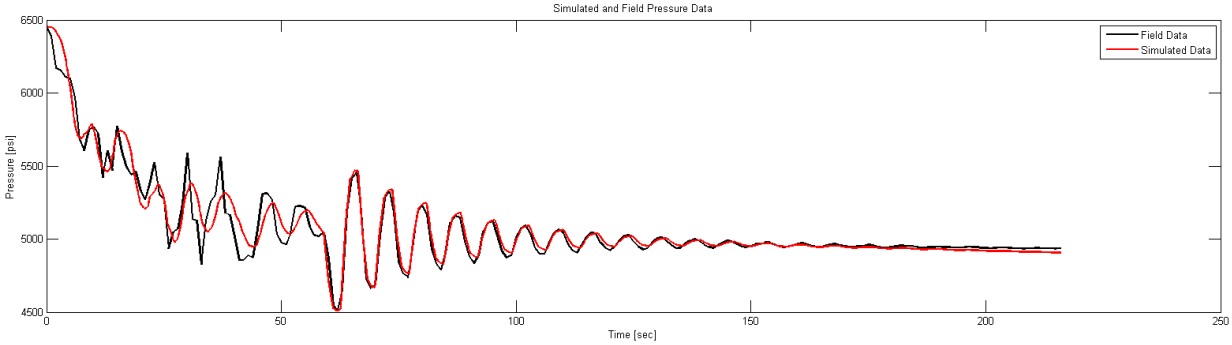

Figure C.25: History match of well B, stage 17 field data with numerical model results

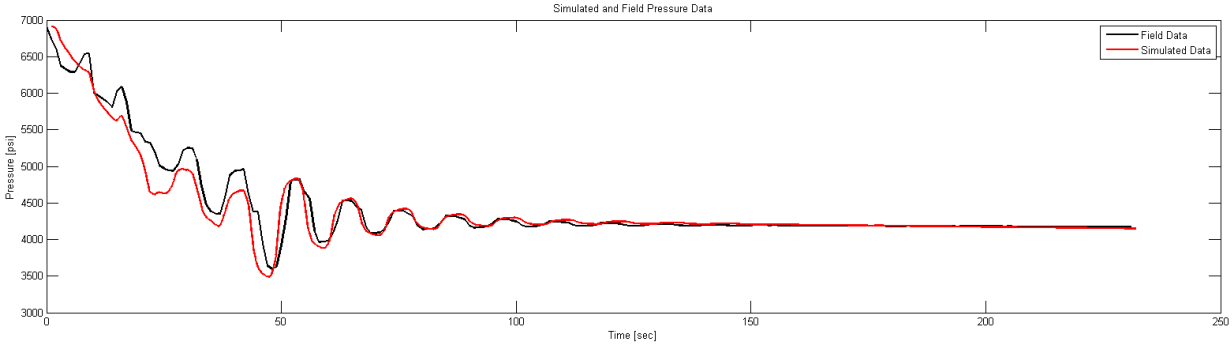

Figure C.26: History match of well C, stage 1 field data with numerical model results

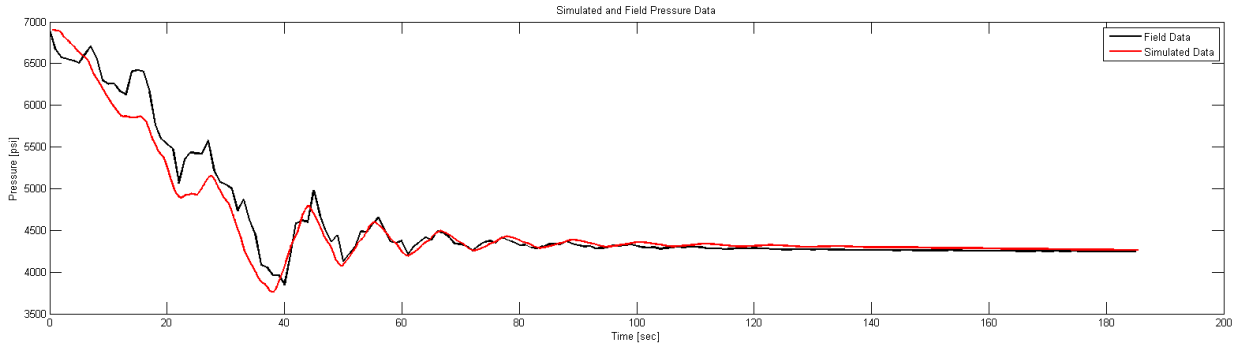

Figure C.27: History match of well C, stage 2 field data with numerical model results

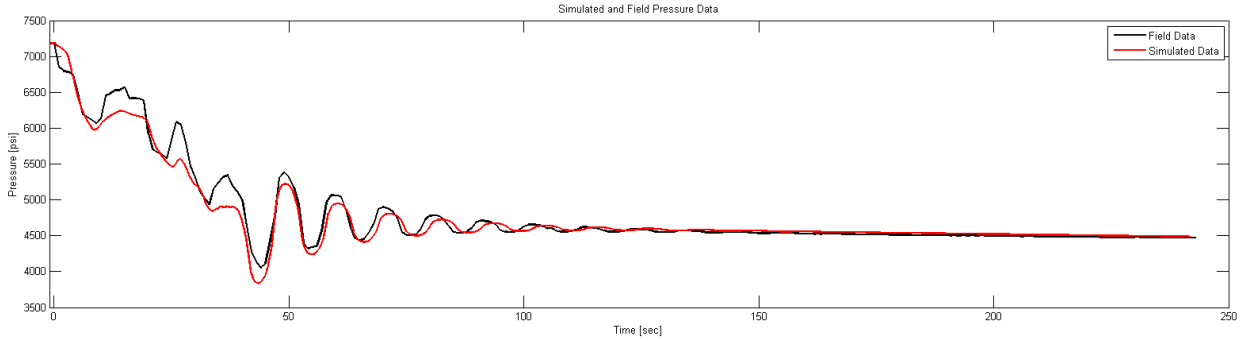

Figure C.28: History match of well C, stage 3 field data with numerical model results

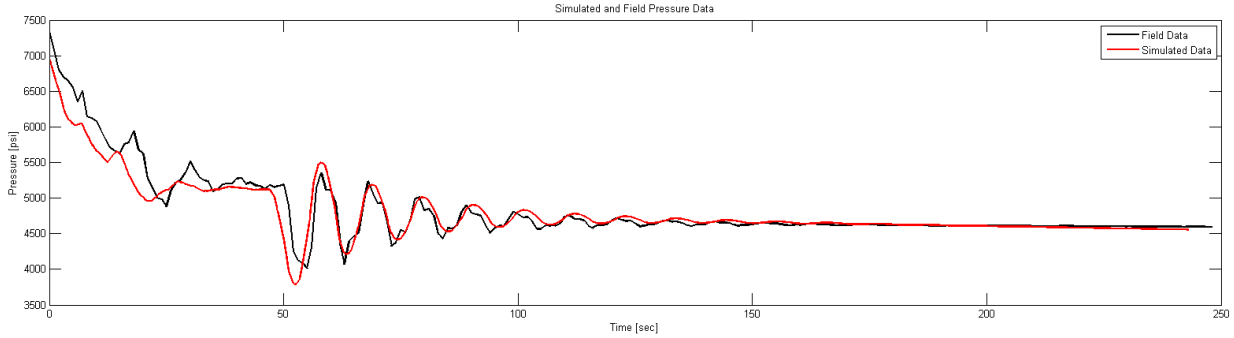

Figure C.29: History match of well C, stage 4 field data with numerical model results

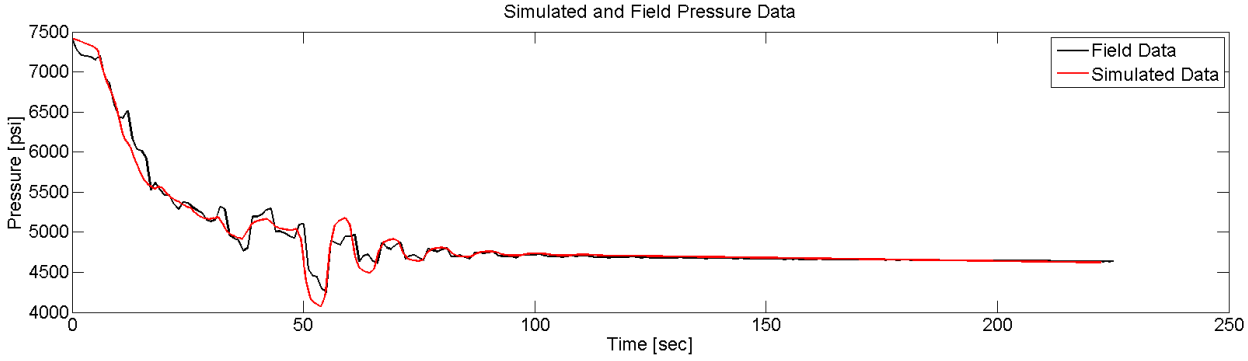

Figure C.30: History match of well C, stage 5 field data with numerical model results

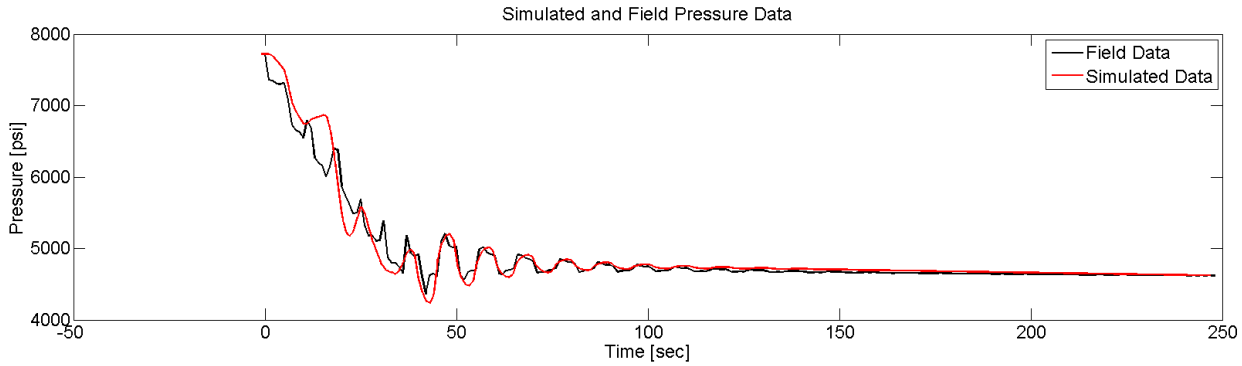

Figure C.31: History match of well C, stage 6 field data with numerical model results.

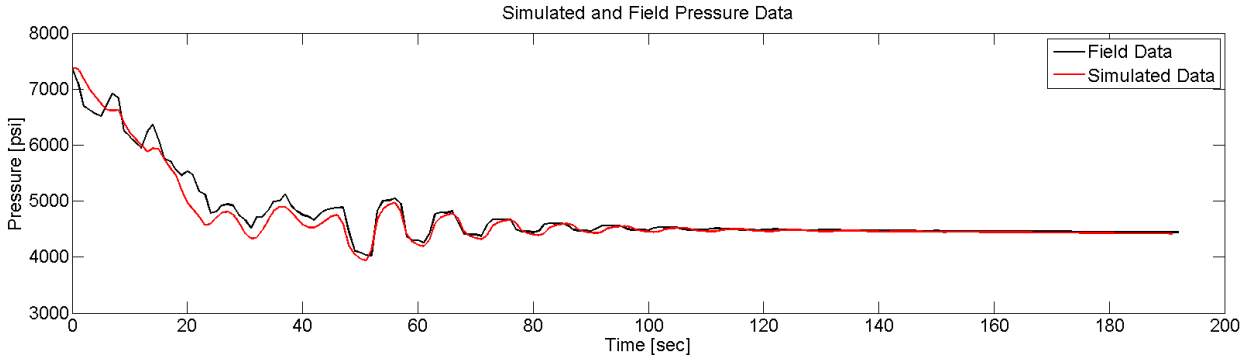

Figure C.32: History match of well C, stage 7 field data with numerical model results.

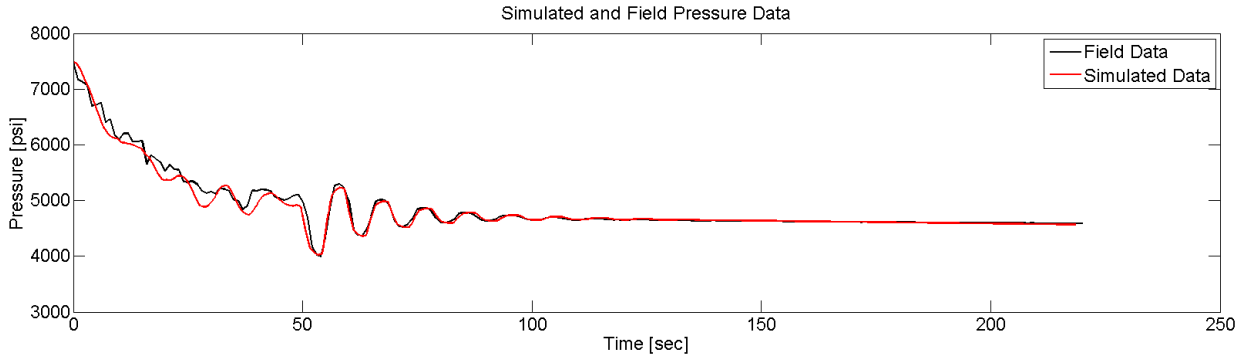

Figure C.33: History match of well C, stage 9 field data with numerical model results.

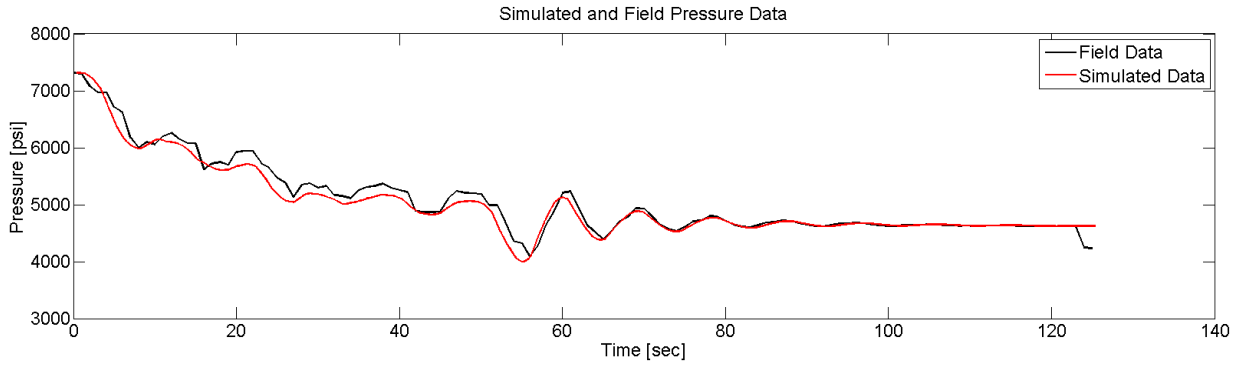

Figure C.34: History match of well C, stage 10 shutdown 1 field data with numerical model results.

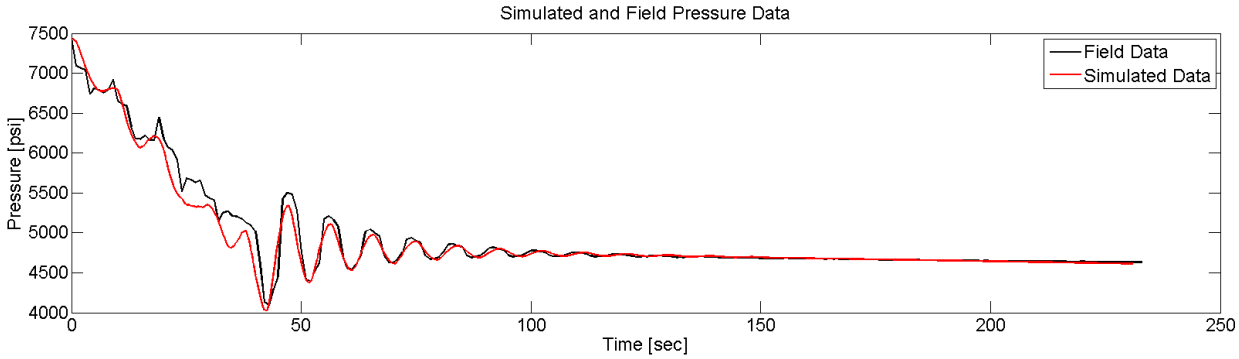

Figure C.35: History match of well C, stage 10 shutdown 2 field data with numerical model results.

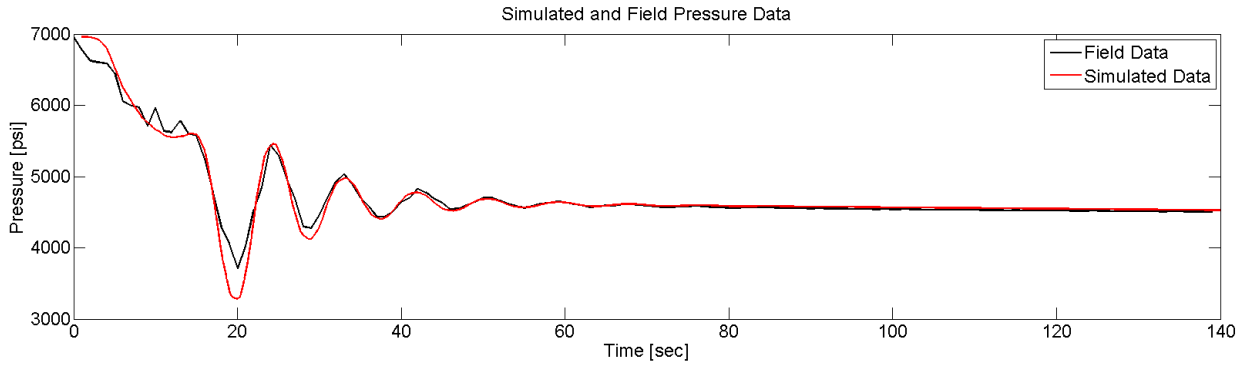

Figure C.36: History match of well C, stage 12 field data with numerical model results.

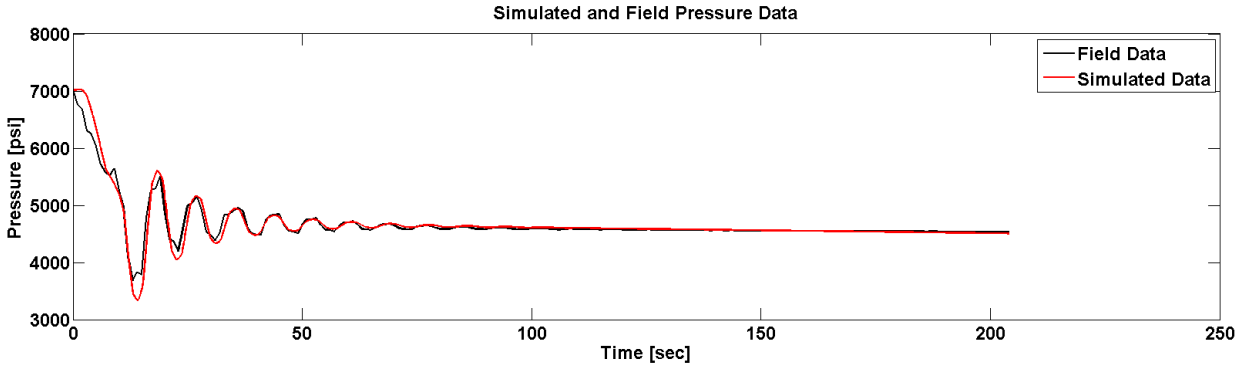

Figure C.37: History match of well C, stage 13 field data with numerical model results.

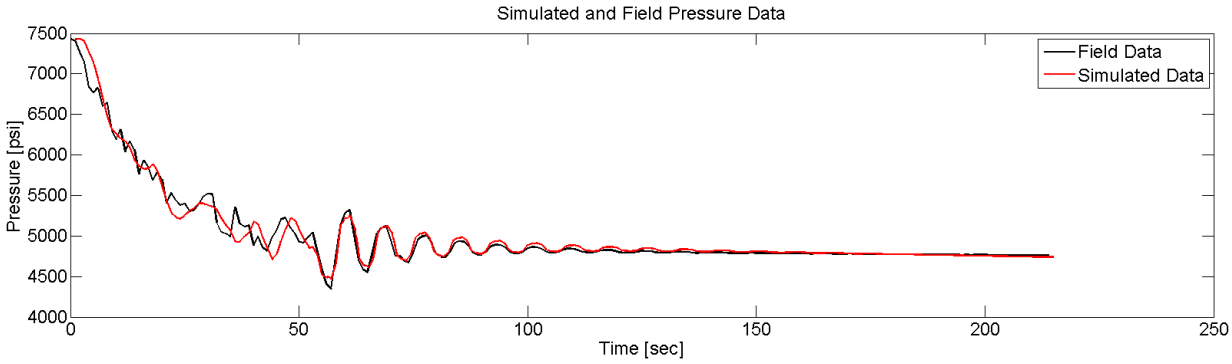

Figure C.38: History match of well C, stage 14 field data with numerical model results.

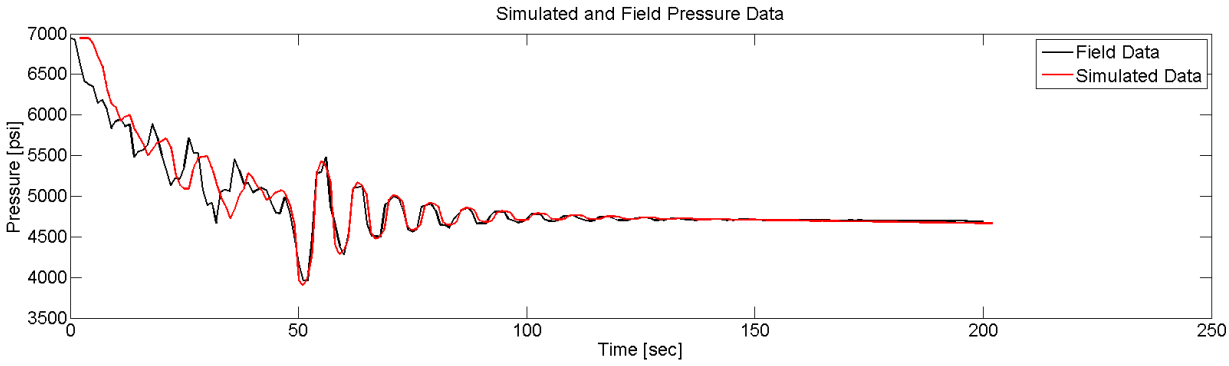

Figure C.39: History match of well C, stage 15 field data with numerical model results.

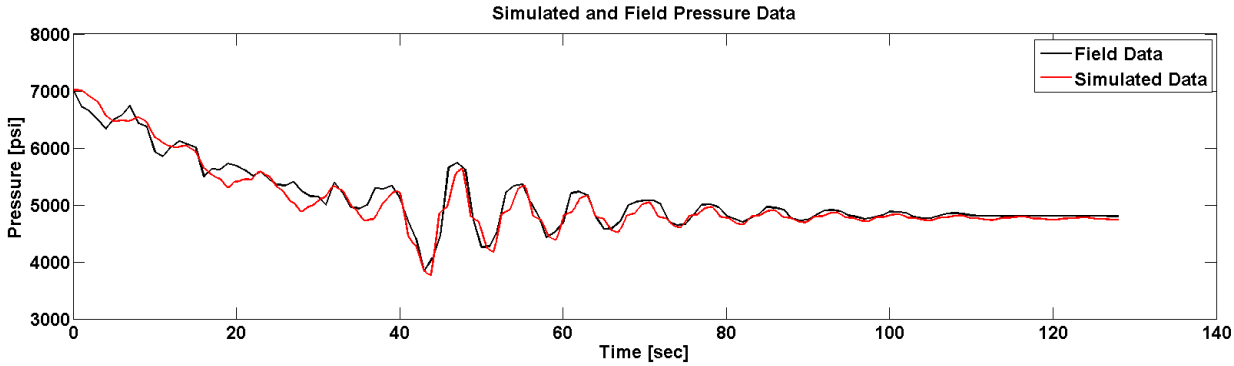

Figure C.40: History match of well C, stage 16 field data with numerical model results.

Appendix D: Tables of *RCI* values and Fracture Dimensions

Stage	R [bpd/psi]	C [bbl/psi]	I [psi/bbl/d2]	Height [ft]	Half Length [ft]	Width [in]	Pnwf [psi]
1	5.20E-03	0.656	7.08E-10	100	811	1.85	336
4	8.44E-03	0.034	1.95E-10	73	80	0.88	1059
5	4.23E-03	0.217	2.45E-10	100	273	1.64	540
6	3.60E-03	0.546	4.90E-10	104	630	1.97	452
7	3.36E-03	0.217	2.45E-10	98	288	1.80	404
8	3.14E-03	0.533	5.49E-10	99	675	1.99	392
9	4.23E-03	0.613	6.31E-10	100	756	1.92	557
10	2.99E-03	0.217	2.45E-10	98	284	1.76	391
11	3.36E-03	0.687	6.16E-10	103	808	2.05	405
12	3.28E-03	0.217	2.45E-10	98	285	1.77	433
13	6.70E-03	0.137	1.95E-10	96	194	1.68	869
14	2.67E-03	0.286	2.45E-10	106	324	2.01	341
15	4.75E-03	0.887	7.76E-10	103	1032	1.94	623
16	4.64E-03	0.344	3.89E-10	100	433	1.68	610
17	2.93E-03	0.875	8.31E-10	102	943	1.83	369

Table D.1: Well A *RCI* and fracture dimension values obtained from history matching

Stage	R [bpd/psi]	C [bbl/psi]	I [psi/bbl/d2]	Height [ft]	Half Length [ft]	Width [in]	Pnwf [psi]
1	4.33E-03	1.017	9.33E-10	101	1246	2.00	506
3	2.67E-03	1.167	7.76E-10	104	1338	2.49	332
4	2.67E-03	1.115	7.94E-10	100	1391	2.41	330
6	3.36E-03	1.115	8.71E-10	101	1342	2.28	342
7	2.61E-03	1.251	9.55E-10	101	1502	2.33	301
8	2.86E-03	1.222	8.91E-10	102	1459	2.41	356
9	2.99E-03	1.064	8.31E-10	101	1295	2.32	388
10	2.12E-03	1.154	8.91E-10	101	1406	2.35	251
11	2.67E-03	1.141	9.12E-10	100	1411	2.32	349
12	2.86E-03	1.141	8.91E-10	100	1401	2.35	341
14	2.99E-03	0.993	7.41E-10	101	1192	2.38	351
15	3.68E-03	1.089	7.94E-10	103	1273	2.34	457
17	2.38E-03	1.340	9.55E-10	105	1509	2.26	296

Table D.2: Well B *RCI* and fracture dimension values obtained from history matching

Stage	R [bpd/psi]	C [bbl/psi]	I [psi/bbl/d2]	Height [ft]	Half Length [ft]	Width [in]	Pnwf [psi]
1	4.23E-03	0.307	3.47E-10	101	375	1.57	474
2	3.95E-03	0.344	3.89E-10	100	431	1.67	426
3	3.21E-03	1.141	9.55E-10	104	1302	1.97	358
4	3.77E-03	1.371	1.00E-09	106	1502	2.12	462
5	2.79E-03	1.371	1.02E-09	106	1515	2.10	349
6	3.77E-03	0.687	6.31E-10	100	843	2.15	465
7	3.77E-03	0.444	4.68E-10	100	555	1.89	477
9	4.23E-03	0.687	6.45E-10	100	847	2.11	529
10	3.28E-03	0.386	3.47E-10	101	465	1.97	400
12	5.98E-03	0.613	6.16E-10	100	768	2.02	672
14	2.67E-03	1.154	1.07E-09	103	1597	2.17	348
15	3.36E-03	0.720	6.76E-10	99	898	2.16	439
16	2.67E-03	1.141	1.00E-09	100	1391	2.07	352

Table D.3: Well C *RCI* and fracture dimension values obtained from history matching.

References

Afshar, M.H., Rohani, M. 2008. Water Hammer Simulation by Implicit Method of Characteristics. *International Journal of Pressure Vessels and Piping* **85**: 851-859.

Allievi, L. 1902. General theory of the variable motion of water in pressure conduits. *Annali della Societa` degli Ingegneri ed Architetti Italiani* **17**(5): 285-325 (in Italian). (French translation by Allievi, in evue de Me canique, Paris, 1904) (Discussed by Bergant et al., 2006).

Allievi, L. 1913. Teoria del colpo d'ariete (Theory of water-hammer.). Atti del Collegio degli Ingegneri ed Architetti Italiani, Milan, (in Italian) (Discussed by Bergant et al., 2006).

Anderson, T.O., Stahl, E.J. 1967. A Study of Induced Fracturing Using an Instrumental Approach. *Journal of Petroleum Technology* **19**(2): 261-267.

Ashour, A.I.S. 1994. A Study of Fracture Impedance Method. *Ph.D Dissertation*. The University of Texas at Austin, Austin.

Barr, D.I.H. 1980. The Transition from Laminar to Turbulent Flow. In: *Proc. Instn. Civ. Engrs.*, Part 2 **69**: 555-562.

Bergant, A., Simpson, A. ., Vı´tkovsky´, J. 2001. Developments in Unsteady Pipe Flow Friction Modeling. *Journal of Hydraulic Research* **39**(3): 249-257.

Bergant. A., Simpson, A.R., Tijsseling, A.S. 2006. Water Hammer with Column Separation: A Historical Review. *Journal of Fluids and Structures* **22**: 135-171.

Bergant. A., Tijsseling, A.S. 2008. Parameters Affecting Water Hammer Wave Attenuation, Shape, and Timing. *Journal of Hydraulic Research* **46**: 382-391.

Bergeron, . 1935. Etude des variations de re gime dans les conduites d'eau-Solution graphique ge ne rale (Study on the Steady-State Variations in Water-Filled Conduits-General Graphical Solution) (in French). *'Hy iq* **1**(1): 12-25. (Discussed in Saikia and Sarma, 2006).

Bergeron, . 1936. Estude des coups de beler dans les conduits, nouvel exose' de la methodegraphique. *La Technique Moderne* **28**: 33. (Discussed in Saikia and Sarma, 2006).

Bird, R.B., Stewart, W.E., Lightfoot, E.N. 1960. Transport Phenomena. John Wiley & Sons, New York.

Bribiesca, E. 1981. Arithmetic Operation Among Shapes Using Shape Numbers. Pattern Recognition **13**(2): 123-137.

Brunone, B., Golia, U.M., Greco, M. 1991. Modeling of fast transients by numerical methods. In: Proceedings of the International Meeting on Hydraulic Transients with Column Separation. 9th Round Table, IAHR, Valencia, Spain. pp. 215-222.

Cipolla, C.L., Warpinski, N.R., Mayerhofer, M.J., Lolon, E.P., Vincent, M.C. 2008. The Relationship Between Fracture Complexity, Reservoir Treatment, and Fracture Treatment Design. Paper SPE 115769 presented at the 2008 SPE Annual Technical Conference and Exhibition, Denver, CO, 21-24 September.

Chaudhry, H.M., Hussaini, M.Y. 1985. Second-order Accurate Explicit Finite-Difference Schemes for Water Hammer Analysis. *Journal of Fluids Engineering* **107**: 523-529.

Chaudhry, H.M. 1987. Applied Hydraulic Transients. 2nd ed. Van Nostrand Reinhold Company, New York.

Chen, N.H. 1979. An Explicit Equation for Friction Factor in Pipe. *Ind. Eng. Chem. Fund.* **18**: 296.

Choi, S.K., Huang, W.S. 1991. Impact of Water Hammer in Deep Sea Injection Wells. Paper SPE 146300 presented at the SPE Annual Technical Conference and Exhibition held in Denver, CO, 2 November.

Ferrick, M.G., Qamar, A., St. Lawrence, W.F. 1982. Source Mechanism of Volcanic Tremor. *Journal of Geophysical Research* **87**: 8675-7683.

Feynman, R.P., Leighton, R.B., Sands, M. 1964. Feynman Lectures on Physics Vol. II. Basic Books, New York.

Ghidaoui, M.S., Mansour, G.S., Zhao, M. 2002. Applicability of Quasi Steady and Axisymmetric Turbulence Models in Water Hammer. *Journal of Hydraulic Engineering* **128**(10): 917-924.

Ghidaoui, M.S., Zhao, M., McInnis, D.A., Ashworthy, D.H. 2005. A Review of Water Hammer Theory and Practice. *Applied Mechanics Reviews* **58**(1): 49-76.

Greyvenstein, G.P. 2006. An Implicit Method for Analysis of Transient Flows in Piping Networks. *International Journal for Numerical Methods in Engineering* **53**: 1127-1148.

Halliwell, A.R. 1963. Velocity of a Water Hammer Wave in an Elastic Pipe. *ASCE Journal of Hydraulic Division* **89**(4): 1-21.

Han, G., Ioannidis, M., Dusseault, M.B. 2002. Semi-Analytical Solutions for the Effect of Well Shut Down on Rock Stability. Paper 2002-050 presented at the Canadian International Petroleum Conference, Calgary, 11-13 June.

Holzhausen, C.R., Gooch, R.P. 1985. Impedance of Hydraulic Fracture: Its Measurement and Use for Estimating Fracture Closure and Dimensions. Paper SPE 13892 presented at SPE/DOE Low Permeability Gas Reservoirs Symposium, Denver, 19-22 May.

Holzhausen, C.R., Egan, H.N. 1986. Fracture Diagnostics in East Texas and Western Colorado using Hydraulic-Impedance Method. Paper SPE 15215 presented at the SPE Unconventional Gas technology Symposium, Louisville, 18-21 May.

Izquierdo, J., Iglesias, P.L. 2002. Mathematical Modelling of Hydraulic Transients in Simple Systems. *Mathematical and Computer Modelling* **35**: 801-812.

Izquierdo, J., Iglesias, P.L. 2004. Mathematical Modelling of Hydraulic Transients in Complex Systems. *Mathematical and Computer Modelling* **39**: 529-540.

Joukowsky, . 1900. n the Hydraulic Hammer in Water Supply Pipes. Me moires de l'Acade mie Impe riale des Sciences de St.-Petersbourg **8**(9): 5 (in German). English translation by, Simin, 1904.

Khalevin, N.I. 1960. Measurement of rock porosity by sonic well logging. *Razvedochnaya i Promyslovaya Geofizika* **30**: 3-9.

Mathieu, F., Toksoz, M.N. 1984. Application of Full Waveform Acoustic Logging Data to the Estimation of Reservoir Permeability. Proceedings, Soc. of Exploration Geophysicists 54th International Meeting, Atlanta. pp. 9-12.

Mondal, S. 2010. Pressure Transients in Wellbores: Water Hammer Effects and Implications for Fracture Diagnostics. *M.S. Thesis*. The University of Texas at Austin, Austin

Morris, R.L., Grine, D.R., Arkfeld, T.E. 1964. Using Compressing and Sheer Acoustic Amplitudes foe Location of Fracture. Journal of Petroleum Technology 16: 623-632.

Paige, R.W., Murray, I.R., Roberts, J.D.M., Mellor, D.W. 1992. Fracture Measurement using Hydraulic Impedance Testing. Paper SPE 24824 presented at the 68th Annual Technical Conference and Exhibition, Washington, DC, 4-7 October.

Paige, R.W., Murray, L.R., Roberts, J.D.M. 1993. Field Application of Hydraulic Impedance Testing for Fracture Measurement. Paper SPE 26525 presented at the SPE Annual Technical Conference and Exhibition, Houston, 3-6 October.

Patzek, T.W., De, A. 2000. Lossy Transmission Line Model of Hydrofractured Well Dynamics. *Journal of Petroleum Science and Engineering* **25**(1-2): 59-77.

Saikia, M.D., Sarma, A.K. 2006. Simulation of Water Hammer Flows with Unsteady Friction Factor. *ARPN Journal of Engineering and Applied Sciences* **1**(4): 35-40.

Santarelli, F.J., Skomedal, E., Markestad, P., Berge, H.I., Nasvig, H. 2000. Sand Production on Water Injectors: Just How Bad Can It Get? *SPE Drill. & Compl* **15**(2): 132.

Schönfeld, J.C. 1951. Analogy of Hydraulic, Mechanical, Acoustic and Electrical Systems. *Appl. Sci. Res.* **3**(B): 417-450.

Shimada, M., Okushima, S. 1984. New Numerical Model and Technique for Water Hammer. *Journal of Hydraulic Engineering* **110**(6): 736-748.

Shylapobersky, J., Wong, G.K., Walhaug, W.W. 1988. Overpressure Calibrated Design of Hydraulic Fracture Stimulations. Paper SPE 18194 presented at the 63rd SPE Annual Technical Conference and Exhibition, Houston, 2-5 October.

Silva-Araya, W. 1993. Energy Dissipation in Transient Flow. *Ph.D Dissertation*. Washington State University, Washington.

Silva-Araya, W., Chaudhry, M.F. 1997. Computation of Energy Dissipation in Transient Flow. *Journal of Hydraulic Engineering* **123**(2): 108-115.

Sneddon, I.N. 1946. The Distribution of Stress in the Neighborhood of a Crack in an Elastic Solid. *Proceedings of the Royal Society A.* **187**(1009): 187-229.

Streeter, V.L., Wylie, E.B. 1967. Hydraulic Transients. McGraw Hill, New York.

Trikha, A.K. 1975. An Efficient Method for Simulating Frequency-dependent Friction in Transient Liquid Flow. *Journal of Fluids Engineering* **97**: 97-105.

Vardy, A.E., Brown, J.M.B. 2004. Transient Turbulent Friction in Fully Rough Pipe Flows. *Journal of Sound and Vibration* **270**(1-2): 233-257.

Vardy, A.E., Hwang, K. 1991. A Characteristic Model of Transient Friction. *Journal of Hydraulics Research* **29**(5): 669-684.

Vaziri, H., Nouri, A., Hovem, K., Wang, X. 2007. Computation of Sand Production in Water Injectors. Paper SPE 107695 presented at the European Formation Damage Conference, Scheveningen, 30 May-1 June.

Walker, T. 1962. Fracture zones vary acoustic signal amplitudes. *W. O*. **154**(6).

Wang, X., Hovem, K. 2008. Water Hammer Effects on Water Injection Well Performance and Longevity. Paper SPE 112282 presented at the SPE International Symposium and Exhibition on Formation Damage Control, Lafayette, 13-15 February.

Wood, D.J. 2005. Water Hammer Analysis – Essential and Easy (and Efficient). *Journal of Environmental Engineering* **131**(8): 341-348.

Wylie, E.B., Streeter, V.L. 1993. Fluid Transients in Systems. Prentice-Hall, New Jersey.

Zhao, M., Ghidaoui, M.S. 2003. Efficient Quasi Two Dimensional Model for Water Hammer Problems. *Journal of Hydraulic Engineering* **1129**(12): 1007-1013.

Zhao, M., Ghidaoui, M.S. 2004. Godunov-type Solutions for Water Hammer Flows. *Journal of Hydraulic Engineering* **130**(4):341-348.

Zielke, W. 1968. Frequency-dependent Friction in Transient Pipe Flow. *Journal of Basic Eng, ASME.* **90**(9): 109-115.